SEISMIC PROCESSING ENHANCEMENT AND ATTRIBUTE ANALYSIS OF THE EARLY JURASSIC NAVAJO SANDSTONE – UINTA BASIN, UTAH

A Thesis Presented to

the Faculty of the Department of Earth and Atmospheric Sciences

University of Houston

In Partial Fulfillment

of the Requirements for the Degree

Master of Science

By Austin Jumper

December 2016

SEISMIC PROCESSING ENHANCEMENT AND ATTRIBUTE ANALYSIS OF THE EARLY JURASSIC NAVAJO SANDSTONE – UINTA BASIN, UTAH

_____

Austin Jumper

APPROVED:

_____

Dr. John P. Castagna, Chairman

_____

Dr. Evgeny Chesnokov

_____

Dr. Donald Van Nieuwenhuise

_____

Dr. William R. Keller, Chief Geophysicist, Enervest, Ltd.

_____

Dean, College of Natural Science and Mathematics

ACKNOWLEDGEMENTS

First and foremost I would like to thank my wife, Shelby, for her love and patience and for always believing in me and encouraging me. I don't see any way I could have done this without her behind me the entire way.

I would like to thank my thesis advisor Dr. John P. Castagna for his instruction and guidance in my M.S. research. It was a privilege getting to learn from him both in the classroom and throughout my research. I would also like to thank my internal committee members Dr. Evgeny Chesnokov and Dr. Donald S. Van Nieuwenhuise for their sound advice and suggestions. Special thanks to Dr. Van Niuwenhuise who encouraged me to come to The University of Houston. I would like to thank my external committee member Dr. William R. Keller and Enervest, Ltd. for providing the dataset for my research. Without their contribution and resources my research wouldn't have been possible. Personally, I want to thank Dr. Keller for giving me the opportunity to gain industry experience while pursuing my degree and for the tremendous amount of help he has provided in the process.

Last, I would like to thank my parents and family for their support and encouragement during this process. Thank you to my mom and to my dad for molding me into the person I am today and helping me in my pursuit of my M.S.

SEISMIC PROCESSING ENHANCEMENT AND ATTRIBUTE ANALYSIS OF THE EARLY JURRASIC NAVAJO SANDSTONE – UINTA BASIN, UTAH

An Abstract of a Thesis

Presented to

the Faculty of the Department of Earth and Atmospheric Sciences

University of Houston

In Partial Fulfillment

of the Requirements for the Degree

Master of Science

By Austin Jumper

December 2016

ABSTRACT

Adding innovative techniques including five-dimensional interpolation, wavelet packet denoising, and bandwidth extension to a traditional seismic processing flow applied to a 3D seismic survey in the Uinta Basin improved signal-to-noise ratio, seismic resolution and attribute calculation of the thin bedded Jurassic Navajo sandstone (30-100 ft.). With five-dimensional interpolation, traces were filled in at places where acquisition restraints led to undersampling. Applying a moderate wavelet packet denoising removed a large portion of the random noise. This aided in velocity analysis for migration. A second round of denoising was run post migration to remove most remaining residual noise. Traditional spectral enhancement techniques resolved the base of the sandstone over a large portion of the survey. Bandwidth extension provided enhanced vertical resolution and lateral continuity better than traditional spectral enhancement techniques. Seismic attributes were integrated with log control to map the structural and stratigraphic nature to a degree not previously achievable on conventional data. Seismic coherence provided an in depth fault map for the Navajo sandstone and indicated the Navajo is laterally continuous (i.e., not truncated). A combination of spectral decomposition with peak attributes and well log control highlighted stratigraphic thinning and enabled mapping of changes in interval thickness. Due to resolution constraints, thin intervals are mapped with high iso-frequencies where the base falls below resolution and the response is from the resolved Navajo base. It was observed that wells producing from thin intervals experienced a decrease in well performance while wells that produce from the seismically thicker Navajo experienced an increase in overall performance.

TABLE OF CONTENTS

Page

Chapter 1: Introduction

1.1 Research Objective

The objective of the research is to combine geophysical and geologic data in the Uinta Basin with leading-edge technology to effectively map the Navajo eolian sandstone to clarify past Navajo production and aid in locating future hydrocarbon potential via frequency mapping. With well log data from eight wells; formation tops are picked to provide control to the model, calculate lithology percentages and porosity, generate synthetic seismograms and analyze well performance in the Navajo interval (Chapter 3). Our particular seismic survey (Stone Cabin 3D) was first reprocessed with a new approach that improves event continuity, signal to noise ratio and seismic resolution. Using 5D (inline, crossline, azimuth, offset and frequency/time) interpolation we can effectively fill in portions of the data where sampling is irregular or traces are missing. Further, residual noise was removed pre-stack by applying an adaptive noise attenuation (denoising) method developed by GeoEnergy, Inc. in Houston, Texas. In addition, Stone Cabin will be taken into hi-resolution bandwidth extension was applied with the goal of resolving the Navajo sandstone (30-100 feet thick) covered in Chapter 4. Seismic attributes such as coherence and spectral decomposition were calculated to properly map fault networks and detect lithologic boundaries (Chapter 5). Due to an Enervest data licensing agreement, the precise locations of local maps are obscured. Including removal of well names, landgrid, or other geographic information, to the extent reasonably possible, in order to protect this commercially sensitive information.

1.2 Stone Cabin 3D

The focus of our study is in the southern portion of the Uinta Basin in Carbon County, Utah. In 2004, a 3D seismic data set was shot by Polaris Explorer for Bill Barrett Corporation over

the Prickly Pear and Peter's Point natural gas fields. Originally, the survey was processed by Sterling Seismic Services. Very little information exists describing what processing techniques were used in their processing flow. The data set is now owned by Enervest Limited, an oil and natural gas operating company based in Houston, TX. A live trace outline showing the surveys position in the basin can be found in Figure 1.2.1. The data set, known as Stone Cabin 3D was shot over an area covering roughly 82 square miles of rough terrain and topography.

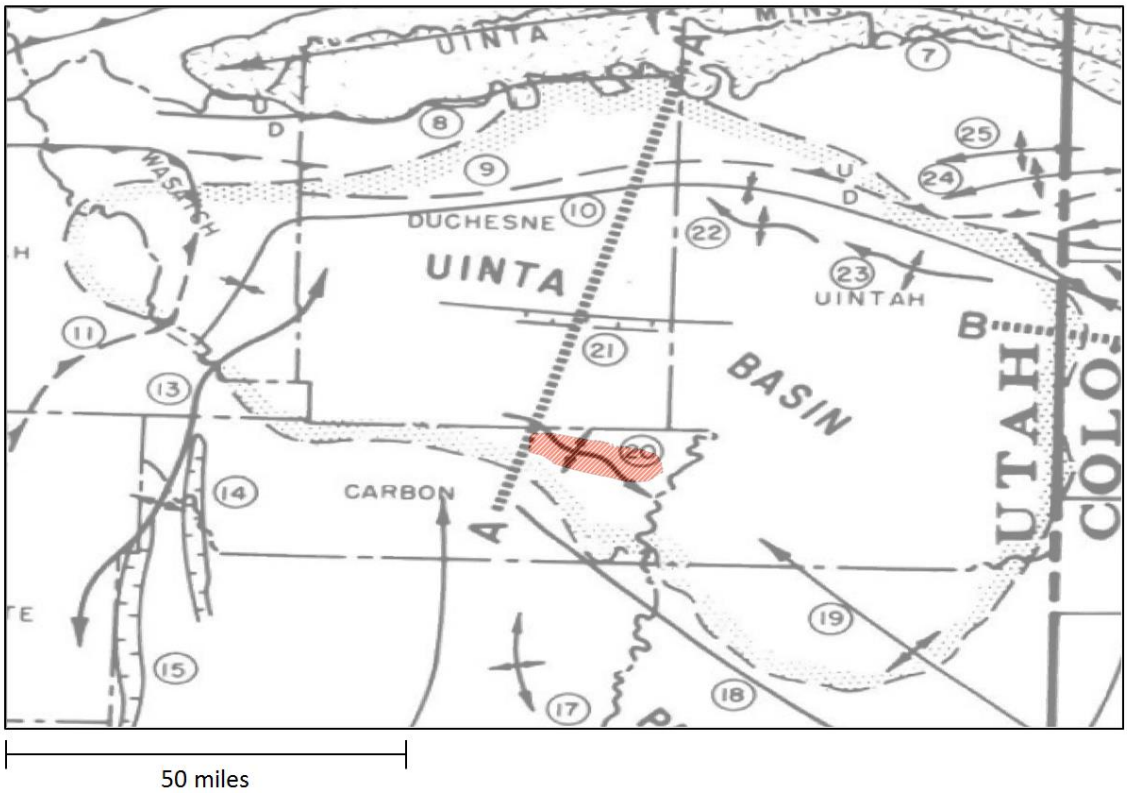

Figure 1.2.1 Stone Cabin 3D (red outline) position in the Uinta Basin along with a tectonic map from Sanborn, 1981. Most notable of these tectonic features are (19) the Uncompaghre Uplift which led to (20) the Uncompaghre Fault that acts as a hydrocarbon trap in our study area.

The in-depth analysis of the study will be over a 10 square-mile cutout over the Peter's Point gas field. The Stone Cabin survey was conducted with 8152 receiver locations and 5285 source locations. Of the source locations, eighty-eight percent were dynamite charges drilled to depths of 50-60 feet and charges ranging from 10-20 pounds. The remaining 12 percent of the sources

were vibroseis (vibe) sweeps from 8 to 100 Hertz with a temporal length of 12 seconds. The survey was recorded on one-component (vertical) p-wave geophones with a sampling rate of two milliseconds. Figure1.2.2 is a display of shot and receiver locations. Receivers (inlines) are oriented north-south and colored red and sources (crosslines) are NE-SW and colored green. Spacing between both receivers and sources were 220 feet, leading to 110 by 110 foot CDP bins.

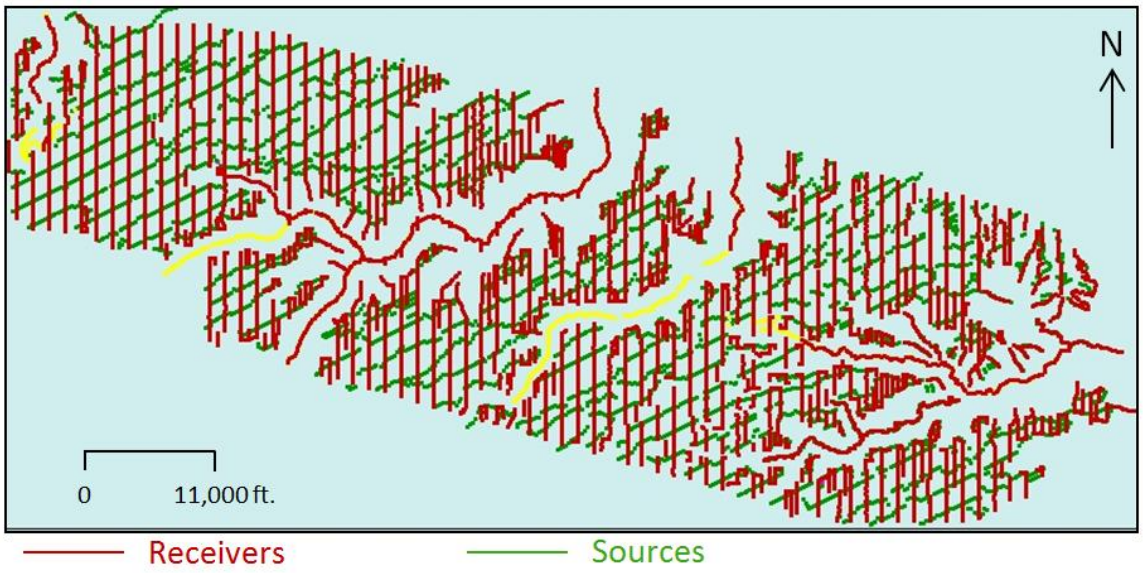

Figure 1.2.2 Source/shot (green) and receiver (red) map for Stone Cabin 3d. Receivers run North-South and shots runs NE-SW.

The receiver elevation map (Figure 1.2.3) shows the vast range in topography of the region. These elevations range from 4897 located in a canyon in the east to 8294 feet in the west. Large gaps between shot and receiver points are a product of the variable topography of the region. These gaps represent canyons that cut through Stone Cabin where the elevation could go from roughly 6500 feet to 4900 feet instantly. Along these canyons, it is not possible to get source or receiver locations. Additionally, the survey relied heavily on heli-portable drilling for source locations and transportation of equipment. The topography creates large gaps in near offset

ranges. A plot of near offsets in Figure 1.2.4 shows that along the canyons the nearest offset is approximately 2000 feet away.

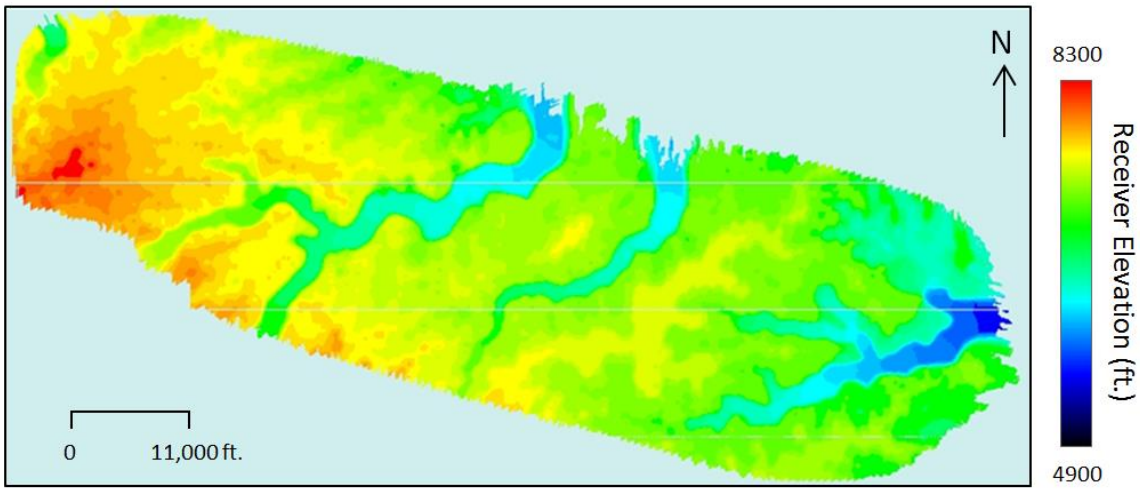

Figure 1.2.3 Receiver Elevation map showing vast range in topography. Warm colors represent higher locations and cool colors represent lows. Elevations range from 4900 to 8300 feet.

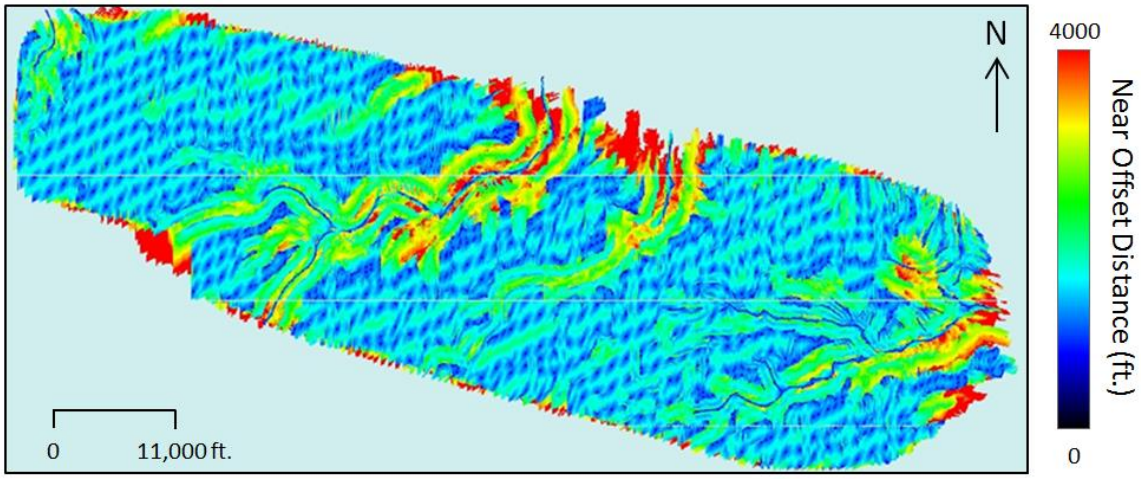

Figure 1.2.4 Plot of nearest offsets for the entire 3D. Notice some near offsets are as far as 4000 feet away. This issue is caused by acquisition geometry and topography.

This far of an offset gap can bring multiple issues in processing techniques for seismic data. For instance, we know that amplitudes tend to diminish as offset increases due to multiple factors (geometric spreading, attenuation, etc.), but when one limits the near offset to 2000 feet, the

total amplitude from stacking can be severely diminished. In addition, a near offset of 2000 feet compared to having what would be considered normal near offset results in lower CMP fold when the data is stacked. A CMP (common midpoint) is known as the location on a reflector that is halfway between a source and receiver. One CMP location, or bin, can represent multiple source and receiver combinations. The total number of source-receiver combinations a CMP bin houses is equivalent to the total number of traces in that CMP bin (Liner, 2004). Displaying all of the traces in a CMP bin at once is termed a CMP gather. When a CMP gather is corrected for normal move out (NMO) and stacked together, the number of total traces stacked is equal to the CMP fold or just fold (Liner, 2004). The more traces in a CMP bin, the higher the fold will be. Therefore, when a near offset is 2000 feet away there are less recorded traces resulting in a diminished fold. The goal in designing a seismic survey is to maximize the number of traces in a CMP bin to increase the fold and decrease the signal to noise ratio (SNR). In Stone Cabin, the large-offset gaps are not entirely related to poor design, but rather topography restraints. Stone Cabin 3D has relatively good fold coverage, averaging a fold of 65 for the entire survey. In the west over the Peter's Point anticline the fold reaches 165 where the receiver coverage is more densely populated. In Figure 1.2.5 a fold coverage map is shown where cool colors correlate to lower fold and warm colors to higher fold. Typically, the edges of a seismic survey will have lower fold than the center because they have far less receiver coverage. This trend can be seen in Figure 1.2.5.

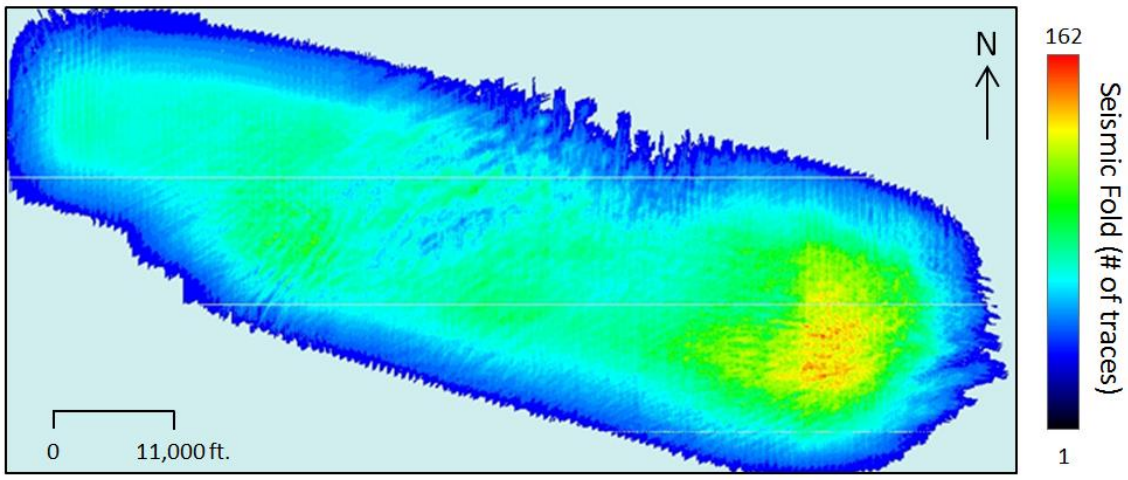

Figure 1.2.5 Seismic fold map. Higher folds are represented in warmer colors and lower folds in cooler colors. The average fold for the survey is roughly 65.

1.3 Well Control and Performance

One of the limiting factors in the research is the inadequate amount of well control within the Stone Cabin survey at the Navajo sandstone interval. The four primary producing intervals are in the Wasatch, North Horn, Dark Canyon and Price River Formations. These producing formations are late Cretaceous to early Paleogene in age. They range in depth from about 3000 feet to 8000 feet depending on well location and target interval. This has resulted in the majority of the well depths ending before reaching the Navajo target by a considerable amount. This trend can also be related to the lack of knowledge of not only the Navajo (14,000 plus feet) interval, but deeper intervals in general. However, there exist some deep well control within the seismic section. A total of eight wells have been drilled within the survey that reach the Navajo, two of which reach the seismic basement. They are primarily deviated wells that approached near vertical in the target interval. Of these eight wells, seven are current Navajo producers, one did not perforate in the Navajo and one does not have

Table 1.1 Initial gas production, cumulative gas production and perforation information for the well control.

Well Name & Number	Initial Gas Production (MCFD)	Cumulative Gas Production (MCF)	Perforation Interval
Well 1	11700	1,955,985	NVJ,ENT,DAK
Well 2	4000	1,528,244	NVJ
Well 3	9900	6,853,137	NVJ
Well 4	950	331,923	NVJ, WIN
Well 5	6100	2,762,152	NVJ, DAK
Well 6	11500	6,344,839	NVJ, ENT
Well 7	679	577,186	NVJ, KAY?
Well 8	N/A	N/A	NVJ

perforation data.

Table 1.1 provides the well name, perforation zones, initial gas production and cumulative gas production for all eight wells that reach the Navajo sandstone. Taking the cumulative gas production data and well name, Figure 1.3.1 illustrates the spatial distribution of well locations. Spatially, there is a high concentration of these wells over the Peter's Point anticline structural high where all eight wells fall within a 3.3 square mile area. The remaining well not used in our study is located over the Prickly Pear anticline 7.5 miles away from the closest well. Considering the survey is 82 square miles, the regional distribution is sparse. The lone well to the west is unique as it was drilled in the mid 1960's and is the only well over Prickly Pear that reaches the Navajo, but it was not perforated in the interval. Existing well logs were obtained in 1967, but it lacks a neutron log. Without a neutron log, it becomes difficult to draw conclusions about the reservoir quality. Altogether, this leads to the Navajo classification as undeveloped in the Prickly

Pear gas field making it an exciting prospect for the future. The eight wells used in the study have a variety of open hole and cased hole logs.

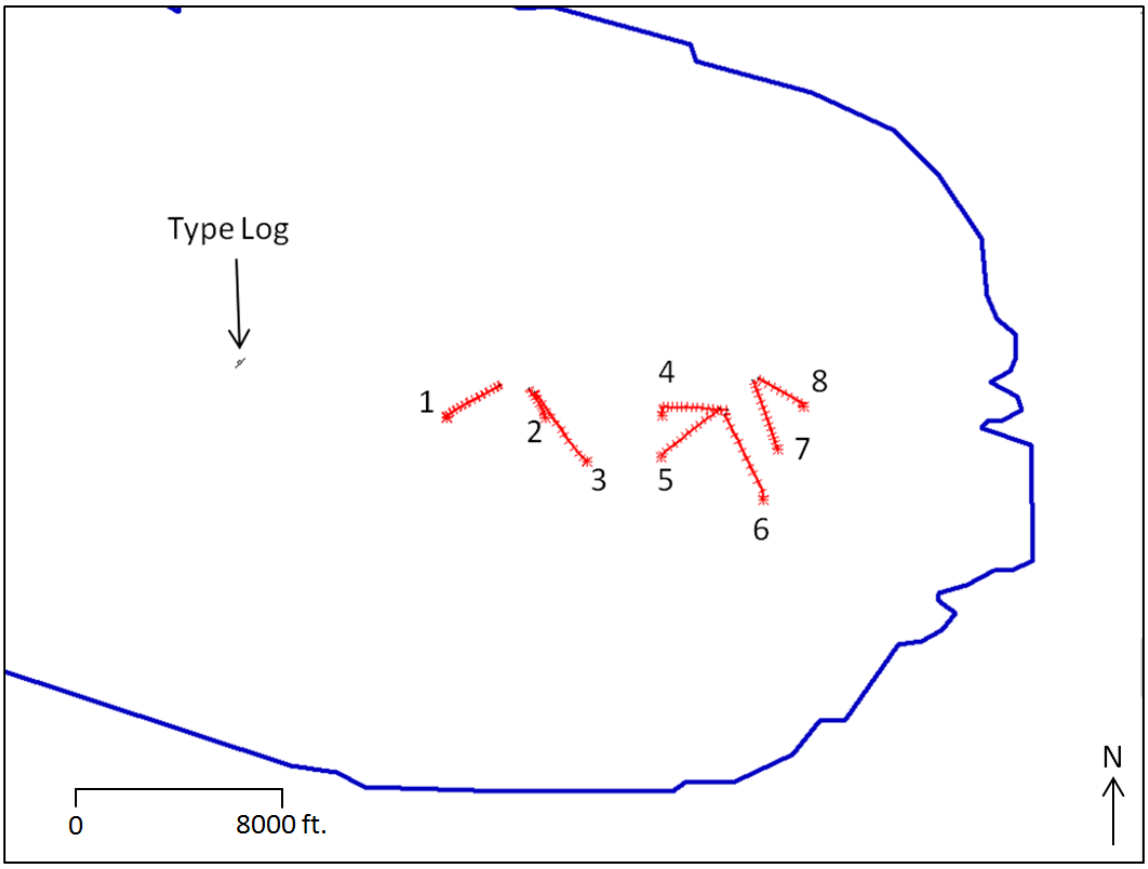

Figure 1.3.1 Well control distribution over Peter's Point. Wells 1-8 and position of the 'Type Log' used for formation top interpretation.

Chapter 2: Data Setting and Basin Geology

2.1 Basin Setting & Tectonics

The Uinta basin is located in northern Utah along the northern edge of the Colorado Plateau with a small portion stretching into western Colorado (McPherson and Bredehoet, 2001). The basin formed from the late Cretaceous into early Paleogene periods during the Laramide orogeny mountain-building episode (McPherson and Bredehoet, 2001). It is described by Osmond (2003) as an asymmetrical foreland basin positioned to the south of the Uinta Mountains. The basin is bounded in all directions by topographic highs. These topographic highs are the result of two mountain-building episodes. First, the Ancestral Rocky Mountain Orogeny was initiated during the late Mississippian to early Pennsylvanian and concluded sometime in the Permian (Budnik, 1986). During the Ancestral Rocky Mountain Orogeny, the Uncompaghre Uplift to the southwest arose. The late Paleozoic Uncompahgre uplift was a topographic high during Uinta basin formation and bounds the basin today to the southwest. Its tectonic movement created the immense Uncompahgre thrust fault (Bump and Davis, 2003). The Uncompahgre uplift can typically be identified in both regional Bouguer and Isostatic anomaly maps. The second episode, known as the Laramide Orogeny (late Cretaceous to Paleogene), is responsible for the present day-Rocky Mountains and basin closure. To the southwest is the San Rafael Swell (or Uplift), “an elongate oval area, surrounded by a rim of inward-facing, almost vertical cliffs” (Gilluly and Reeside, 1928).” According to Bump and Davis (2003), the San Rafael Swell is a doubly plunging anticline that occurred during the Laramide orogeny. The swell was active much later than the Uncompahgre Uplift and continued through the formation of the Uinta Basin. Together, the Uncompahgre Uplift and the San Rafael Swell are joined by the Book Hill Cliffs which mark the entire southern border of the basin. To the east, the basin is enclosed

by the Douglas Creek Arch, a north-south-oriented faulted anticline that also formed during the Laramide Orogeny (Bader, 2009). This structural high is significant because it separates the Uinta Basin from the Piceance Basin in western Colorado. The Wasatch Mountains to the west and the Uinta Mountains in the north finish the closure of the basin. Johnston and Yin (2001) states the Uinta Mountains were formed from the Uinta (Mountains) Uplift. This particular structure is unique as it is an east-trending Laramide structure opposed to north-south (Johnston and Yin, 2001). All of these features create structural highs around the basin, giving it a bowl-like shape. The Ancestral Rocky Mountains Orogeny and Laramide Orogeny had differing stress fields causing fracture orientation in the study area to shift from NW-SE trending to NE-SW. Stone (1977) suggested that tectonic movement from the Laramide Orogeny may have reactivated some of the Paleozoic age faults, while other Laramide structures are oblique to ancient structures. Faulting in and around the basin tend to be reverse or thrust faults that are associated with the two mountain building tectonic episodes discussed. Many of these thrust faults are responsible for hydrocarbon trapping and accumulation, much like the trapping mechanism in Prickly Pear and Peters Point gas fields discussed later. Figure 2.1.1, modified from Sanborn (1981), provides an in depth look at the complex structural setting of the Uinta basin. Outlined in red is the focus area of our study.

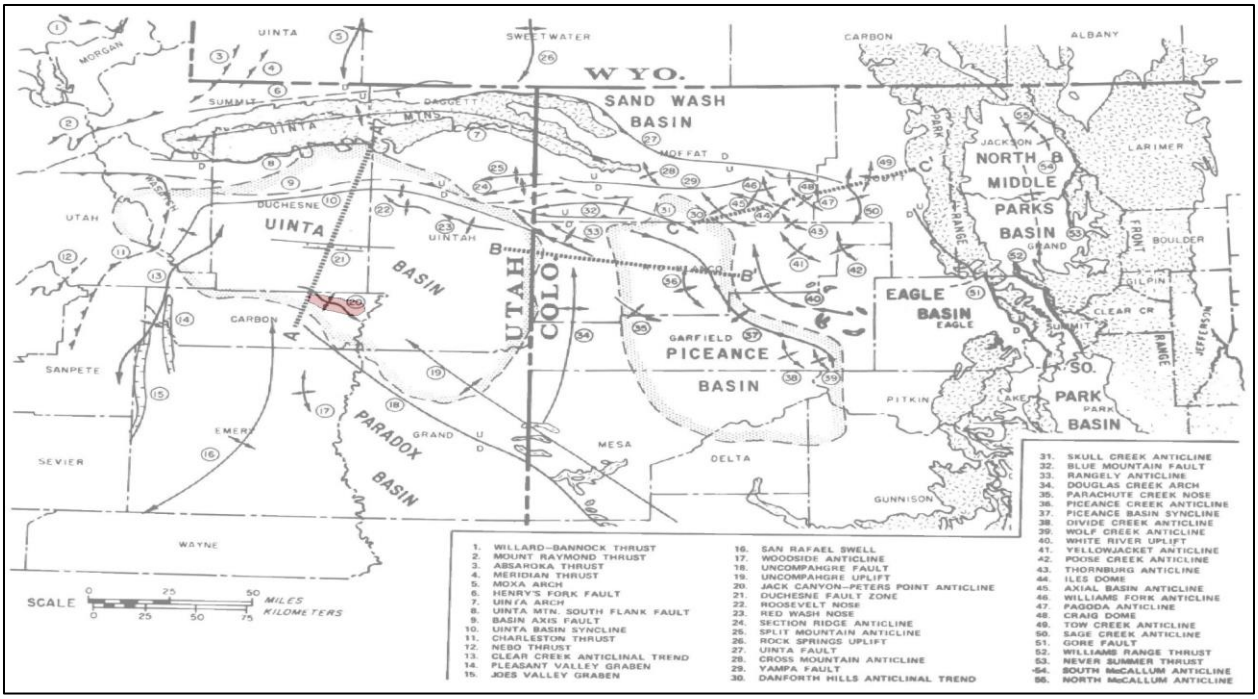

Figure 2.1.1 Modified from Sandborn, 1981. An in-depth look at the basin tectonics that contributed to the Uinta Basin formation.

2.2 Basin Geology

Much of the sediment fill in the Uinta Basin was controlled by the topographic highs surrounding the basin. As the tectonic movement forced the exterior to rise above the basin, sediments were eroded and transported into the basin via rivers, streams and braided channel systems. Erosional internal drainage from these topographic highs led to massive amounts of deposits in either alluvial or lacustrine environment from the late Cretaceous into the late Paleogene (Keighley et al, 2003). The basin is generally deeper to the northwest where sediments are the thickest. Moving to the east, the overall geologic package tends to thin. Figure2.2.1 from Sanborn (1981) provides a cross section of the basin from the San Rafael Swell in the south to the Uinta Mountains in the north. This cross section (A-A') is located in Figure 2.2.1 for reference in map view in the basin.

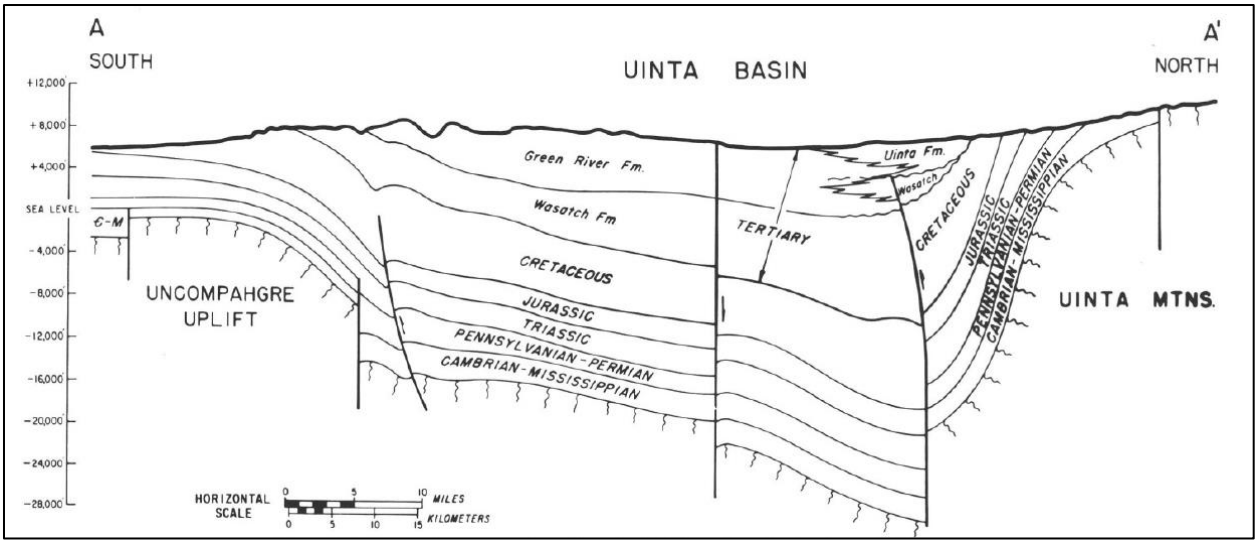

Figure 2.2.1 Regional cross section take from Sanborn, 1981. A-A' correlates with Figure 2.1.1 previously.

Conveniently, this cross section covers the study area in Carbon County. As much as 4 kilometers (roughly 13,000 feet) of sediment filled the basin (Keighley et al., 2003). To better understand the differing depositional phases, it is useful to classify the depositional environments by periods. A stratigraphic column for the basin can be found in Figure 2.2.2.

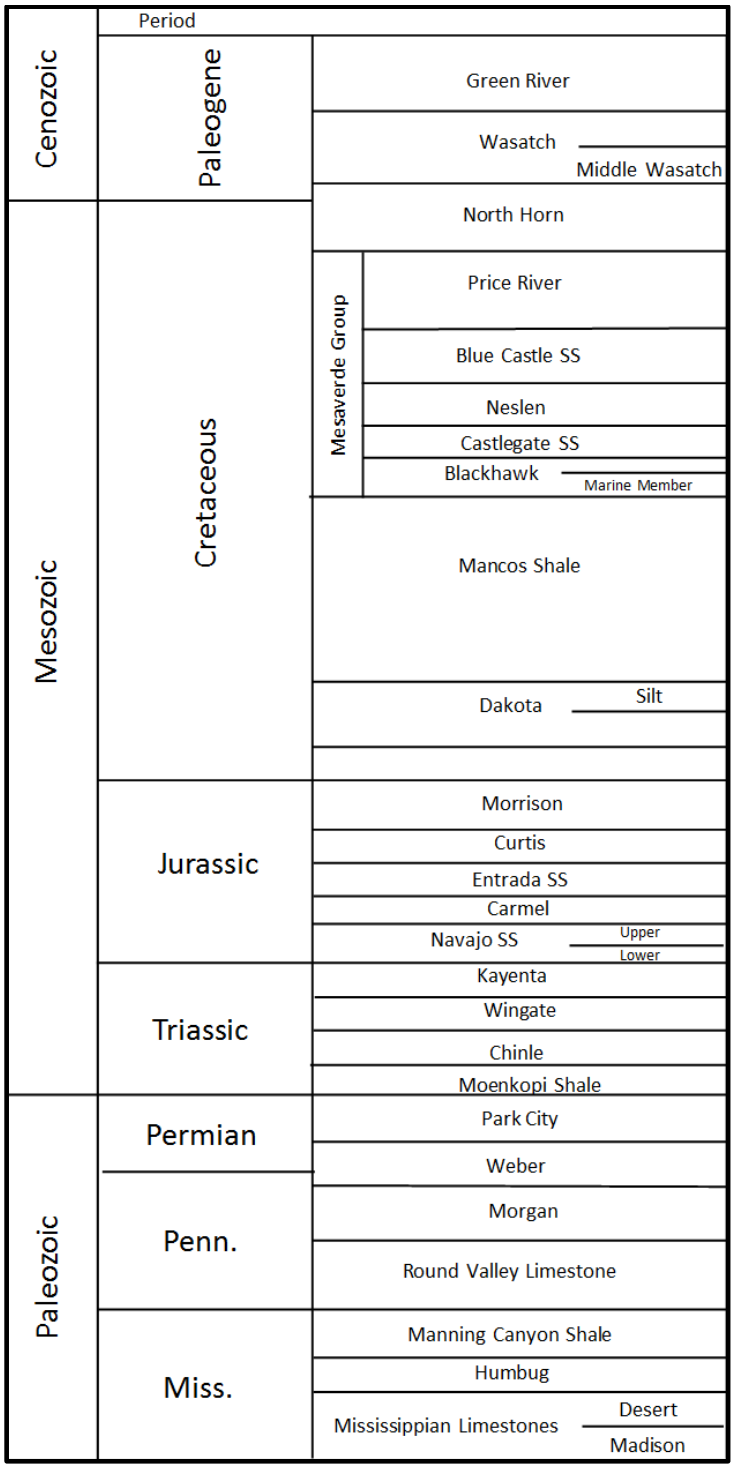

Figure 2.2.2 Stratigraphic column of formations for the Uinta Basin (created using regional geology knowledge). The focus of the study will be on the Early Jurassic Navajo sandstone.

Mississippian

Mississippian deposition was controlled by a period of marine transgression (Sanborn, 1977). The Mississippian packages are predominately carbonate strata capped by weathering sandstones and black shales. The lower Mississippian Madison limestone and the upper Mississippian Deseret formation consist of dark gray cherty limestone and dolomite (Baker et al, 1949). Above the Deseret, the upper Mississippian Humbug Formation is separated by an unconformity and characterized as a brown-weathering sandstone interbedded with the same cherty limestone found in the Madison and Deseret formations (Baker et al, 1949). The Humbug formation was capped in the upper Mississippian by the Manning Canyon black shale. Mississippian strata are present in two well logs not used in our study area, and can be easily correlated based on their gamma ray response. The overall package is thicker in the Prickly Pear anticline in the west and thins to the east towards the Peter's Point anticline. It is faulted by the NW-SE trending thrust fault from the Ancestral Rocky Mountain Orogeny (visible in our vertical seismic profile) that continues into the Permian age strata.

Pennsylvanian and Permian

Deposition during the Pennsylvanian and Permian occurred during a time of continuous tectonic activity (Sanborn, 1977). The lower Pennsylvanian Round Valley Limestone is separated from the two Morgan Formation members by an unconformity. The Morgan strata were deposited during a period of marine regression in the lower Pennsylvanian and can be broken into a lower and upper member. The lower Morgan consists mainly of limestone while the upper member contains sandstone with interbedded limestone (Baker et al, 1949). The Weber "Sand Sea" eolian sandstone (upper Pennsylvanian and lower Permian in age) blanketed these sands and limestones. The Weber is similar in nature to the Navajo Sandstone which we're

concerned with. In the Upper Permian, the marine cyclic Park City is a pinkish gray limestone interbedded with sandy limestones and calcareous sandstones (Baker et al, 1949). The Park City Formation has been considered by some as a potential source rock for the Weber Sandstone in nearby basins (Sandborn, 1977).

Triassic and Jurassic

In the early Triassic, the sea regressed west (Osmond, 2003). The Moenkopi silty shale and siltstone lies under a channel-filling sandstone that was deposited once the area was exposed (Osmond et al., 1968). Another period of marine cyclic deposition occurred that brought the Chinle and Kayenta formations to this area. These formations are dominated by shales and interbedded sandstones. Deposited on top of this sequence is the massive Navajo eolian sandstone during the Triassic to Jurassic transition. The Navajo is a fine to medium-grained cross-stratified sandstone (Osmond et al., 1968). It is a known productive interval, but generally requires closed structures for accumulation (Sanborn, 1977). In our study area, the Navajo is thin (30-90 feet) and well logs show thinning as it steps off the Peter's Point structure. The Navajo is capped by the Carmel Formation that has a mixture of sandstone, shale, and small limestone beds. The Carmel Formation is dense and provides a good hydrocarbon seal. Another period of eolian deposition followed bringing the Entrada Sandstone. The Entrada is also very similar to the Navajo. In the Late Jurassic, more shales with lenticular sandstones interbedded were deposited known as the Curtis and Morrison Formations.

Cretaceous & Paleogene

In the Cretaceous, the Uinta Mountains began to rise (Sanborn, 1977). The Uinta Mountains to the north and the Uncompahgre Uplift to the south controlled much of the deposition during this period. The upper Jurassic Morrison is separated from the Dakota

sandstone at the Jurassic-Cretaceous boundary by a transgressive overlap from the present seaway advanced westward (Walton, 1944). The Upper portion of the Dakota brings a silty sequence or Dakota Silt. This silt boundary can be tracked across all wells and is a relatively good marker for starting the geologic interpretation in deeper sections of the well logs. This becomes particularly easy, because lying above the Dakota sandstone and silt is the massive Mancos shale. This shale is obvious and dominated by quartz-silt and clay minerals (Taylor and Macquaker, 2014). The Mancos shale is rich in hydrocarbons and is currently a candidate in both the Piceance and Uinta Basin for hydrocarbon exploration, but has limited porosity. With current-day fracking technology and horizontal drilling, it could become a serious contender in shale plays of the Rockies. The following Blackhawk and Neslen formation were deposited along the Western Margin of the marine foreland (Pitman et al, 1987). These rocks are thick in the west and thin to the east, eventually pinching out near the Utah-Colorado border. Pitman et al. (1987) claims both formations contain large amounts of thermogenic gas in low-permeable reservoirs. The Blackhawk formation was deposited into wave dominated deltas in the Upper Cretaceous Seaway and coarsened upward from marine silty-shale to fine-grained sandstone (Pitman et al, 1987). Afterwards, the seaway rested at a high stand where the marginal marine Castlegate sandstone was deposited over the Blackhawk via rivers and streams in large amounts (Pitman et al, 1987). As the depositional energy decreased, fine grained sand and shales were deposited on top of the Castlegate known as the Neslen. Following the Neslen another change in sea level and deposition brought thick amounts of fine- to course-grained quartz sandstone similar to the Castlegate known as the Blue Castle. Approaching the end of Cretaceous deposition, the poorly sorted fine- to medium-grained siltstone and sandstone Price River formation was deposited by northeast flowing fluvial systems. We group this period of

deposition into the Mesaverde Group (Blackhawk, Castlegate, Neslen, Blue Castle and Price River).

In the Upper Cretaceous, a vast majority of the Rocky Mountains were covered by the Upper Cretaceous Interior Seaway (Abbot, 1957). The actual Cretaceous to Paleogene boundary is not well marked. Continual deposition during this period led to the lack of an unconformity marker. For this reason, the lower Paleogene North Horn formation can be considered both upper Cretaceous and lower Paleogene in age. The North Horn formation was dominated by fluviatile and lacustrine deposition resulting in gray carboniferous shales interbedded with hard, dense limestones (Abbot, 1957). With the receding Upper Cretaceous Seaway, the Wasatch formation consisting of fluvial shales with interbedded sandstone was deposited above the North Horn. The Wasatch being fluvial in nature gives it great hydrocarbon potential but introduces difficulties with geophysical and geologic well log mapping due to the discontinuous nature of the potential reservoir rocks. Continuing the period of fluvial deposition, the Colton formation was deposited. The Colton formation differs from the Wasatch bringing larger amounts of sandstone to a previously shale rich system (Taylor et al., 2004). Capping off the geologic column, the hydrocarbon rich Green River formation was dominated by gray mudstone, carbonates and salt; typically the Green River sequence is interpreted as a lacustrine facies (Keighley et al., 2003).

There are four primary producing intervals covered in the Stone Cabin the 3D seismic area; primarily the Upper Cretaceous Price River through the Lower Paleogene Wasatch formations. The shallow formations are relatively difficult to track on the current processed seismic. Part of this is due to the nature of the near surface having a low seismic fold which allows noise to be more pronounced. A possible additional objective of the data enhancement

done herein will be to map these fluvial and lacustrine sands. This will depend on the signal-to-noise improvement of the reprocessed data set.

2.3 Uinta Basin Hydrocarbons

The Uinta Basin houses multiple oil- and natural-gas-producing fields. Generally, the oil producing fields are located in the northern portion of the basin. The two most notable oil fields are the Greater Altamont-Bluebell and Greater Red Wash. The natural gas producing fields are largely positioned in the central to southern portion of the basin. The most prominent is the Natural Buttes field. Figure 2.3.1 from Fouch et al (1992) illustrates the positioning of the multiple oil and natural gas fields in both the Uinta and the nearby Piceance Basins. This thesis is focused on the Prickly Pear and Peter's Point gas fields. The Peter's Point and Prickly Pear fields are located in Carbon County, Utah just west of the Green River and east of Price, Utah. The two gas fields are structurally trapped against a northwest-southeast oriented thrust fault labeled in Figure 2.1.1 as the Jacks Canyon-Peter's Point Anticline.

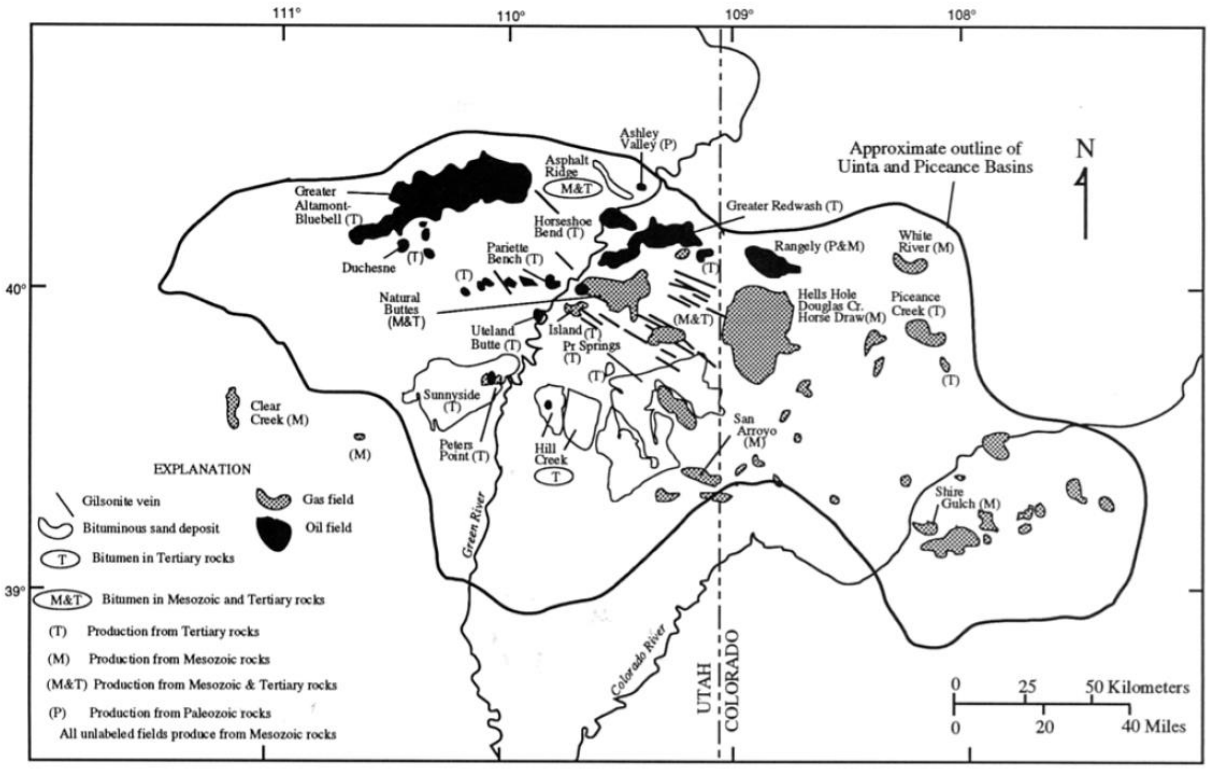

Figure 2.3.1 Regional gas and oil fields of Eastern Utah and Western Colorado from Fouch et. al., 1992.

Figure 2.3.2 is a time structure (two-way) map taken at the Navajo sandstone horizon showing the Prickly Pear (west), Peter's Point (east) gas fields and the trapping thrust fault that is up-thrown to the north. The two fields are separated by a structural low or saddle in the middle. Primary hydrocarbon production in these fields comes from lacustrine and fluvial sandstones lenses in the Upper Cretaceous to Lower Paleogene intervals. Secondary production derives from structurally trapped porous sandstones or gas rich shales in the Cretaceous to Lower Jurassic intervals. In particular, this thesis will be focused around the evolution of the Jurassic Navajo eolian sandstone (secondary producing zone) and its controls on current day hydrocarbon production.

Source rocks for hydrocarbons in the basin were generated commonly by hydrogen-rich Type I and Type II kerogen from lacustrine and marine environments (Rice, Fouch and Johnson

et al, 1992). Rice, Fouch and Johnson (1992) states some hydrocarbon generation is due to Type III kerogen associated with rocks deposited in non-marine settings. Type III is an oxygen-rich kerogen that produces gaseous hydrocarbons as it is being buried over time (Rice, Fouch and Johnson; 1992). Source rocks in the Uinta Basin have contrasting thermal maturity. This might explain why the oil plays tend to be to the north and the gas plays to the south. Anders, Palcas and Johnson (1992) preformed a study that concluded source rocks in the basin were immature to the north and increased in maturity to the south. A separate study by Rice, Fouch and Johnson (1992) showed that thermally mature rocks produce dry and wet gas, while thermally immature rocks tend to generate oil.

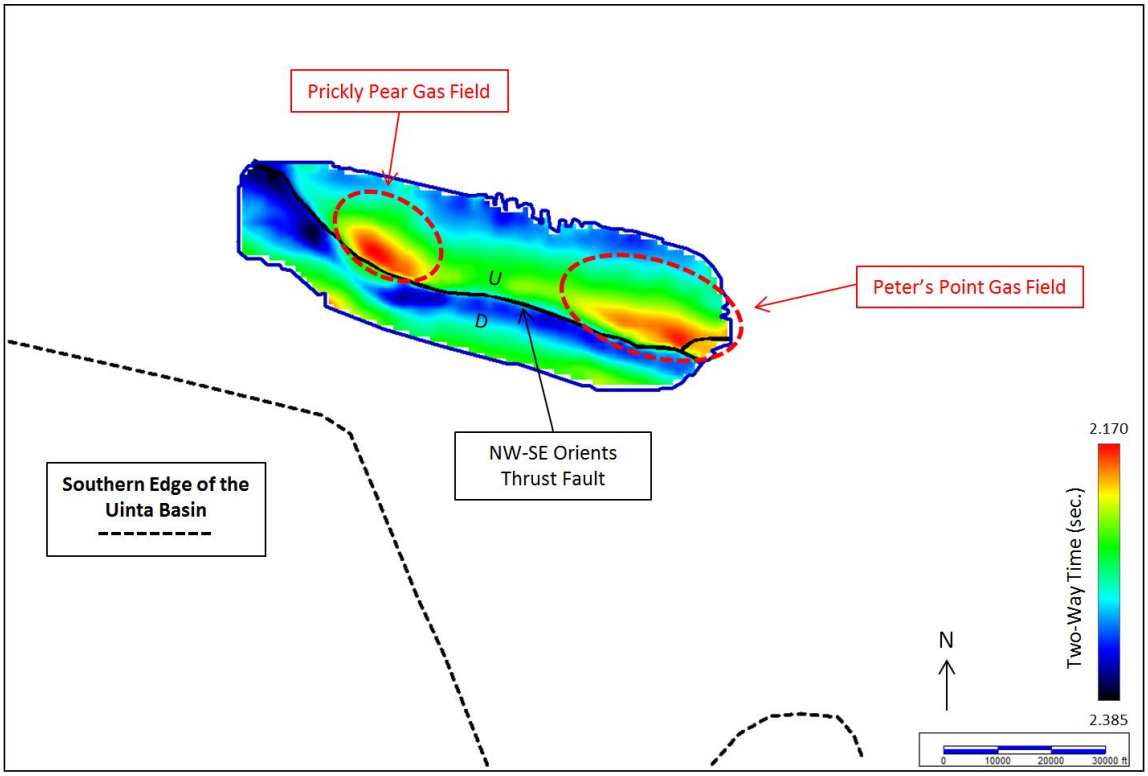

Figure 2.3.2 Two-way time structure map of the Navajo sandstone. circled in red are the Peter's Point and Prickly Pear anticlines/gas fields. To the south is the regional NW-SE thrust fault that acts as a hydrocarbon trap.

Chapter 3: Stone Cabin Processing

3.1 Data Quality Enhancement

The first objective of the research was to reprocess Stone Cabin 3D in a manner that would increase the signal-to-noise ratio (SNR), improve vertical seismic resolution and improve event continuity. Using an updated processing flow with the latest technology well-log correlation and seismic attribute quality can be improved. A processing flow that was as close to AVO (amplitude variation with offset) compliant as possible was followed. Processing with an AVO compliant approach preserves the amplitudes as much as possible. The basic processing flow used combines normal processing procedures used in most processing with new technology like five-dimensional interpolation (5-D) and four-dimensional (4-D) wavelet packet denoising. The preliminary processing flow is outlined in this chapter, but the focus will be on 5-D interpolation and 4-D wavelet packet denoising to improve SNR and resolution. Further post-processing techniques like angle muting, spectral whitening, spectral shaping and principal component filtering are also covered in more detail.

The entire processing flow is listed in Table 3.1. In the flow, methods are broken into primary, secondary and tertiary processing procedures. The most important methods are referred to as *primary* in that most of these procedures can be used in every processing flow. The primary techniques are essential to data quality and fidelity. Using the steps in Table 3.1 many combinations of stacks with different techniques applied are made. The most basic of these stacks combines all the primary procedures and excludes secondary and tertiary procedures. This stack will be used as the reference *raw stack* to quantify parameters for secondary and tertiary processing steps. Additional stacks are made by combining

Table 3.1 Processing flow from Pre-processing, Primary, Secondary and Tertiary processes.

Flow Number	Processing Procedures	Classification
1	Minimum phase conversion	Primary/Pre-Processing
2	Merge navigation with seismic trace headers	Primary/Pre-Processing
3	Geometry assignment and trace edits	Primary/Pre-Processing
4	Amplitude recovery	Primary/Pre-processing
5	Refraction statics	Primary
6	Elevation statics	Primary
7	Surface-consistent scaling	Primary
8	Pre-deconvolution noise attenuation	Primary
9	Surface-consistent deconvolution	Primary
10	Surface-consistent scaling	Primary
11	1st Round velocity analysis	Primary
12	Phase rotation and bulk (static) shift	Primary
13	1st Pass residual statics	Primary
14	2nd Pass velocity analysis	Primary
15	2nd Pass residual statics	Primary
16	Residual phase and static correction	Primary
17	Trim statics	Primary
18	FX deconvolution noise attenuation	Primary
19	4-D wavelet packet denoising - Pre-migration/pre-5-D interpolation	Secondary
20	3rd Round Velocity Analysis (non-denoised gathers)	Secondary
21	3rd Pass residual statics (non-denoised gathers)	Secondary
22	5-D Interpolation	Secondary
23	Pre-stack velocity analysis	Primary
24	Pre-stack Kirchhoff migration	Primary
25	4-D wavelet packet denoising (Post-migration/5-d interpolation)	Secondary
26	Angle mute	Secondary
27	Spectral whitening	Tertiary
28	FX deconvolution noise attenuation	Tertiary
29	Low-frequency spectral shaping	Tertiary
30	FX deconvolution noise attenuation	Tertiary
31	Principal Component Filtering	Tertiary
32	Final Stack	Primary

primary with secondary or tertiary methods. Secondary methods are useful in improving SNR and event continuity. Tertiary methods can be combined solely with primary procedures or with

both primary and secondary procedures. These particular stacks are useful when trying to analyze a particular formation, but can be dangerous when analyzed over the entire volume. Therefore, many of the parameters for tertiary procedures are selected with the goal of resolving or enhancing only a portion of a seismic volume. For this study, the goal is to resolve the Navajo eolian sandstone.

Regardless of the combination of procedures, certain parameters will be unchanged due to the acquisition geometry and recording of the data. These parameters are shot and receiver interval; inline and crossline orientation; sample rate and record length. For the Stone Cabin survey the shot and receiver intervals are both 220 feet, with inlines (receivers) oriented North-South and crosslines (shots) East-West. The time sample interval was 2 milliseconds making the Nyquist frequency 250 Hertz with a total record length of 5 seconds. With this information, the primary processing workflow can be initiated. The raw stack prior to application of the primary processing flow is shown in Figure 3.1.1. From here the goal is to make improvements that provide an enhanced stack with the best SNR, resolution and fidelity that the data will allow.

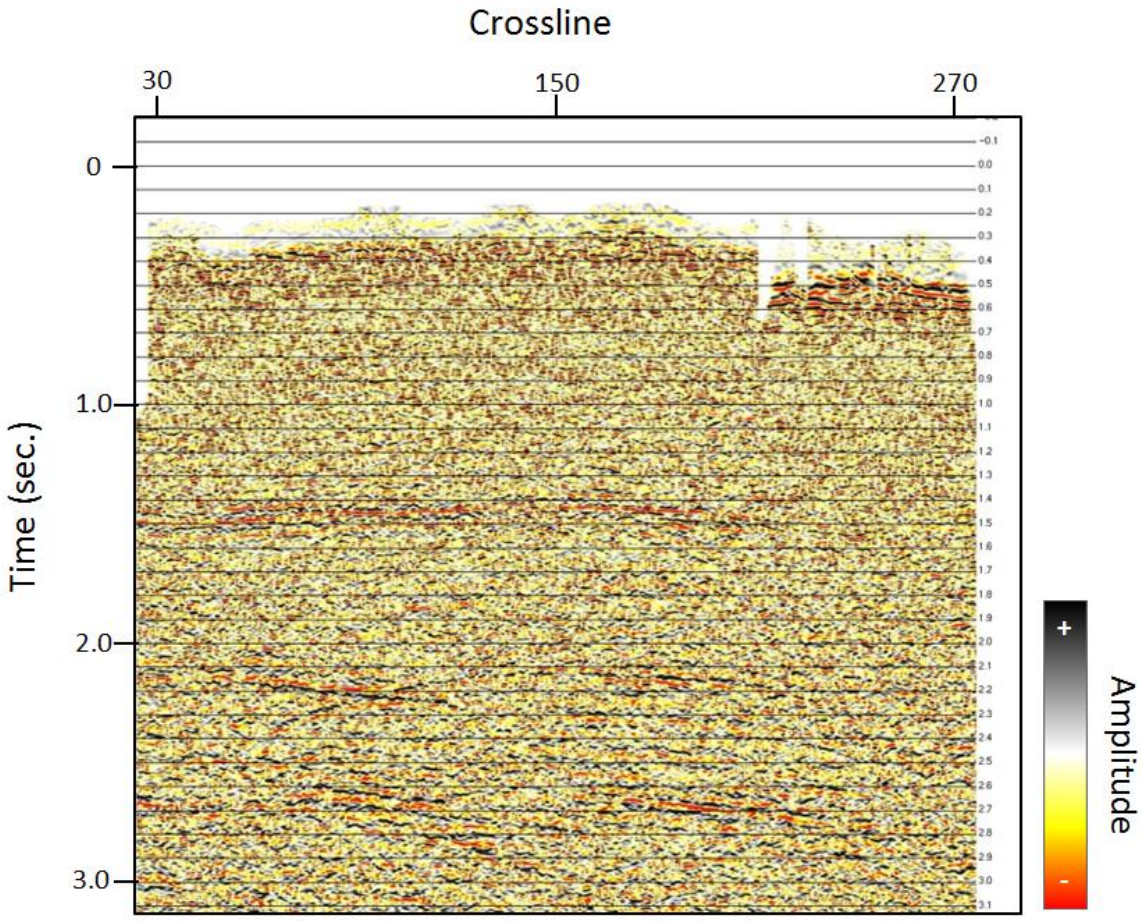

Figure 3.1.1 Raw stack with elevation statics applied on inline 285. All amplitudes are relative and thus unitless. (1 crossline = 110 feet).

3.2 Primary Processing Workflow

Pre-Processing

The first thing done in primary processing is converting each source to minimum-phase. This process is outlined later in the section in Figure 3.2.6. This is particularly important for vibroseis sources since their energy can produce a wavelet that is mixed phase due to “sweeps” at multiple frequencies. A vibroseis (vibe) truck produces a sweep source that starts at low frequencies and gradually increases (linearly or non-linearly) to high frequency, usually 10-120

Hertz. A single vibe shot consist of multiple sweeps and has a temporal length from 12-15 seconds. While a zero-phase wavelet is the most desirable for interpretation, it is not possible to get a zero-phase source wavelet. This would mean energy existed at time zero which isn't possible. The best that can be done is to convert the mixed-phase wavelets into minimum-phase. Dynamite sources are typically closer to minimum-phase but both a vibe sweep and dynamite shot must be converted to minimum phase for subsequent processing. Many processing techniques, like spiking deconvolution, operate using a minimum phase wavelet.

The next step is to set up the survey geometry. The goal of this is to properly place shot and receiver locations and optimize seismic fold. Each shot and receiver has GPS navigation providing its exact spatial location. First, the shot and receiver navigation is merged with the seismic trace header. Using the shot and receiver interval of 220 feet, the survey is broken into bins. Bins are typically half of the shot and receiver interval resulting in 110 feet by 110 feet bin spacing for Stone Cabin, where each bin is a perfect square. Shot and receivers are then oriented to inline and crossline locations, where the spacing interval is both 110 feet respectively. Inlines are numbered 1 (east) to 854 (west) and oriented north-south, crosslines are numbered 1 (south) to 394 (north) and oriented east-west. This produces maximum CDP coverage, increasing the overall fold for the survey. A quick test for accurate geometry is to pick first break arrivals on a CDP gather. If the geometry is correct, a plot of time-offset arrivals will have a linear pattern. If the pattern is scattered, the geometry has failed. The result of our geometry assignment can be found in Figures 1.2.2 (shot and receiver map), 1.2.3 (shot and receiver elevation map), 1.2.4 (near-offset plot) and 1.2.5 (fold map).

Geometry is followed by trace editing. This is a simple procedure to quality check (QC) traces to eliminate dead traces, reverse the polarity of any traces recorded improperly or

eliminate bad traces. After editing a large window automatic gain correction (AGC) for amplitude recovery is applied. This is necessary to correct for amplitude loss due to "source radiation pattern, receiver response, geometric spreading and attenuation effects of the medium (Zhou, 2014)." Applying an AGC is not permissible for AVO analysis and should be used very carefully. Since the overall goal in this study isn't analyzing amplitudes with offset, a long window AGC allows amplitudes to be boosted for visibility and balances amplitudes laterally while retaining amplitude relations between nearby events in a given trace.

After geometry assignment, trace editing and amplitude recovery are completed, elevation and refraction statics are applied. Elevation statics is the process of shifting each shot and receiver to a floating or final datum. A floating datum is a constant distance from surface and a final datum is a flat constant elevation. In this study, each shot and receiver was moved to a final datum of 8300 feet. This elevation correction makes it possible to process on a surface – consistent datum. Refraction statics, deconvolution and other processing operations are most effective when the surface is consistent, so each shot that goes into each receiver doesn't require different static shifts.

Refraction Statics

Refraction statics is a technique that uses critically refracted energy (first-breaks) to predict the depth and velocity structure of the near-surface (Lawton, 1989). Typically, first-breaks are used due to their linear nature that allows for simpler ray tracing. There are multiple methods for making this correction depending on data acquisition locations and near surface complexities. This study tested three of the most used methods – GLI (generalized linear inversion) one-layer, GLI two-layer and tomostatics. GLI one- and two-layer solutions assume a constant near surface reflector(s). This means, the refracting layer is a constant time layer cake.

First break arrival picks are then inverted to give a “best” least-square fit of the near-surface model (Schneider and Kuo, 1985). An accurate model is then obtained through multiple forward iterations until the observed first breaks (refractions) best match the calculated first breaks (Schneider and Kuo, 1985). This method can be broken into one or two layers depending on the complexity of the near surface. GLI solutions normally perform better when topography is relatively flat. In tomostatic solutions, the near-surface model is determined by a tomographic inversion and corrects the statics predicted by the velocity model (Zhou, 2014). The near-surface is described by cells, not layers, with the goal of accounting for horizontal differences in the near-surface. Generally, tomostatics performs better than GLI solutions in regions of varying topography where the near-surface model might be complex. This, however, was not the case in this Rocky Mountain dataset. Both GLI and tomostatics rely on carefully calculated first-break picks and replacement velocities. The Stone Cabin calculated replacement velocities are calculated by the average velocity of the first-break arrivals (Lawton, 1989). Our calculated replacement velocities are relatively fast due to denser, faster rocks in the regions near-surface.

For the GLI one-layer model, we calculated a replacement velocity of 10,000 feet per second and a datum elevation of 8300 feet were used. For the GLI two-layer model a replacement velocity of 13,000 feet per second and datum elevation of 8300 feet were used. This resulted in the GLI two-layer having better uplift in the vertical seismic display than the one-layer model. Figure 3.2.1 and Figure 3.2.2 show a stacked comparison of the GLI one-layer and two-layer solutions respectively. The increase in uplift in the GLI two-layer model helps align reflectors which increase the horizontal resolution. The black arrows in Figure 3.2.2 point to reflectors that are better resolved in the two-layer model and the green arrows point to areas where the two-layer model provided better uplift to the reflectors.

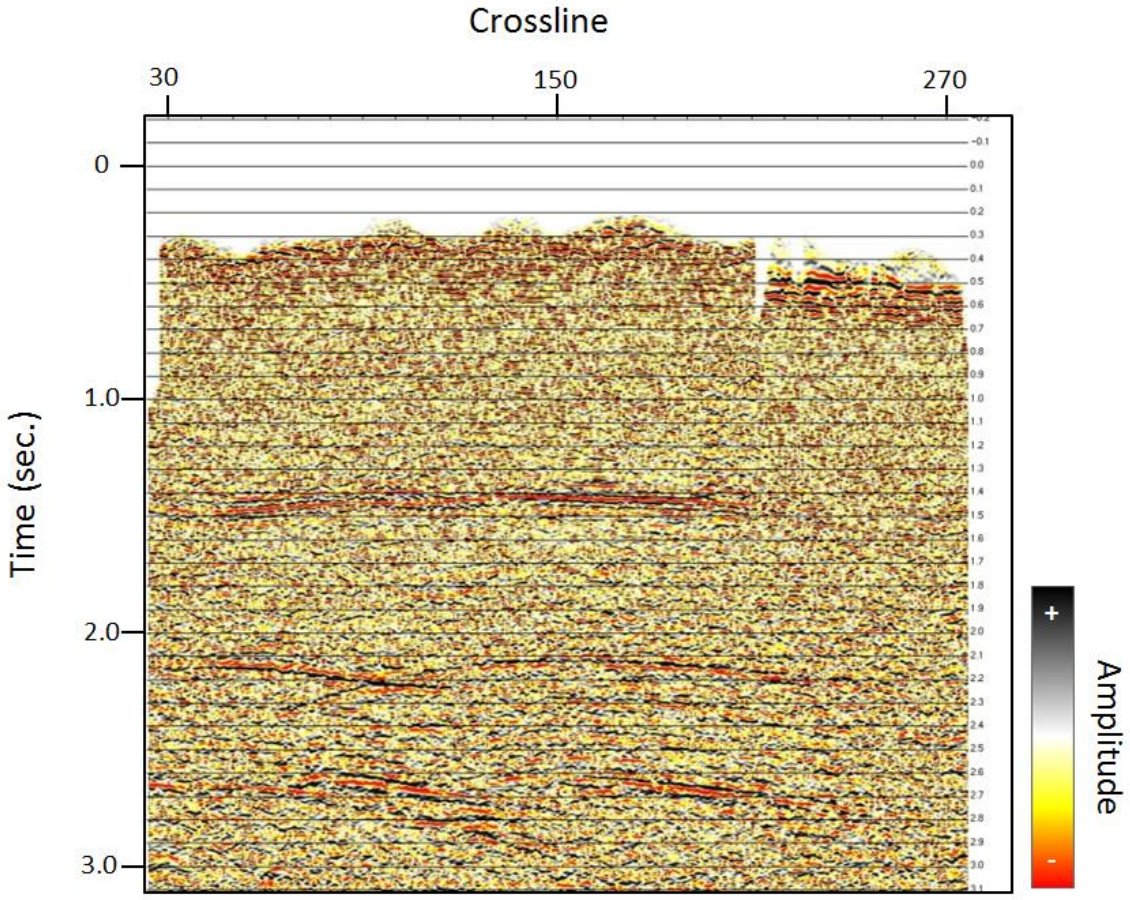

Figure 3.2.1 GLI one layer model with RV=10,000 f/s and datum = 8300 feet. All amplitudes are relative and thus unitless. (1 crossline = 110 feet).

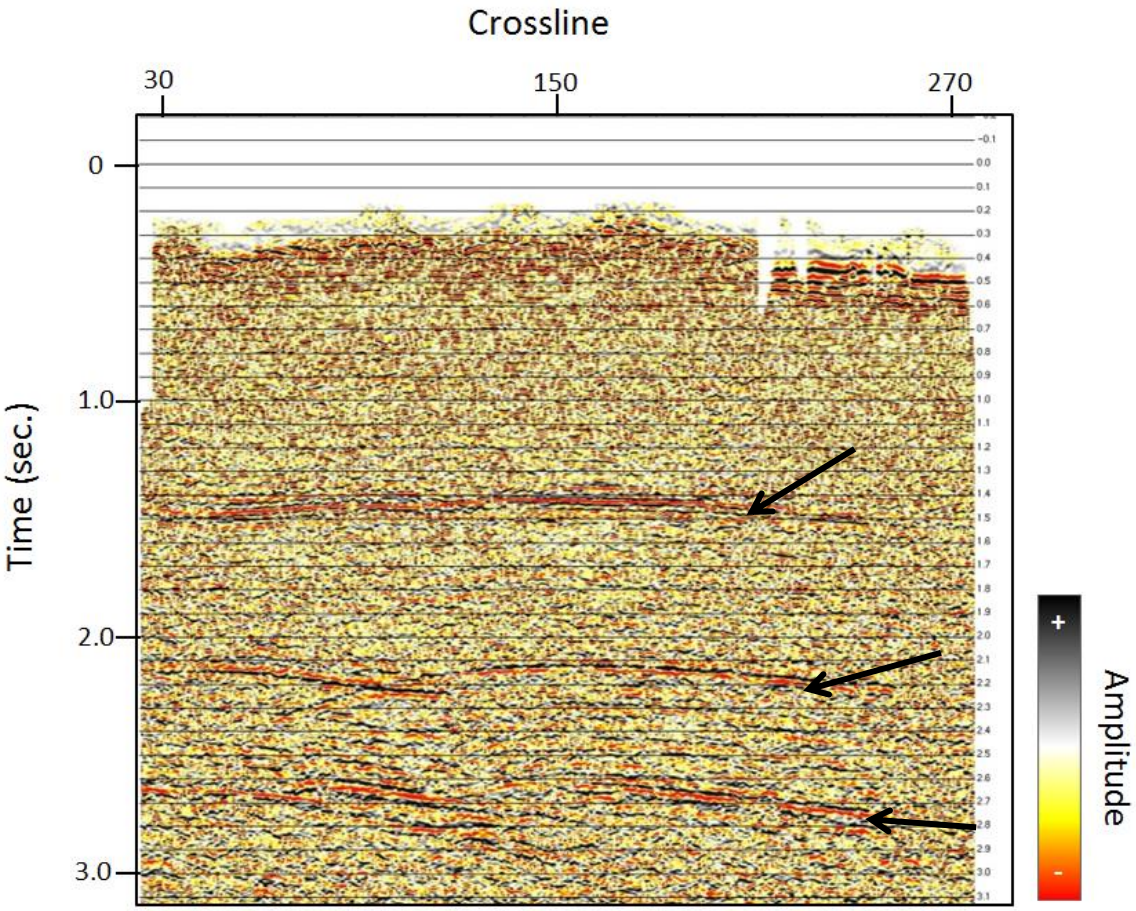

Figure 3.2.2 GLI two-layer model with RV=13,000 f/s and datum=8300 feet. Black arrows point to reflectors that had better solution with two-layer model. All amplitudes are relative and thus unitless. (1 crossline = 110 feet).

Using the GLI two-layer model for a comparison, tomostatics were run with a replacement velocity of 13,500 feet per second and an elevation datum of 8300 feet. The GLI two-layer model produced a better solution than the tomostatics solution (Figure 3.2.3) over the majority of the dataset. This is evidenced by comparing Figure 3.2.3 to the results of Figure 3.2.2.

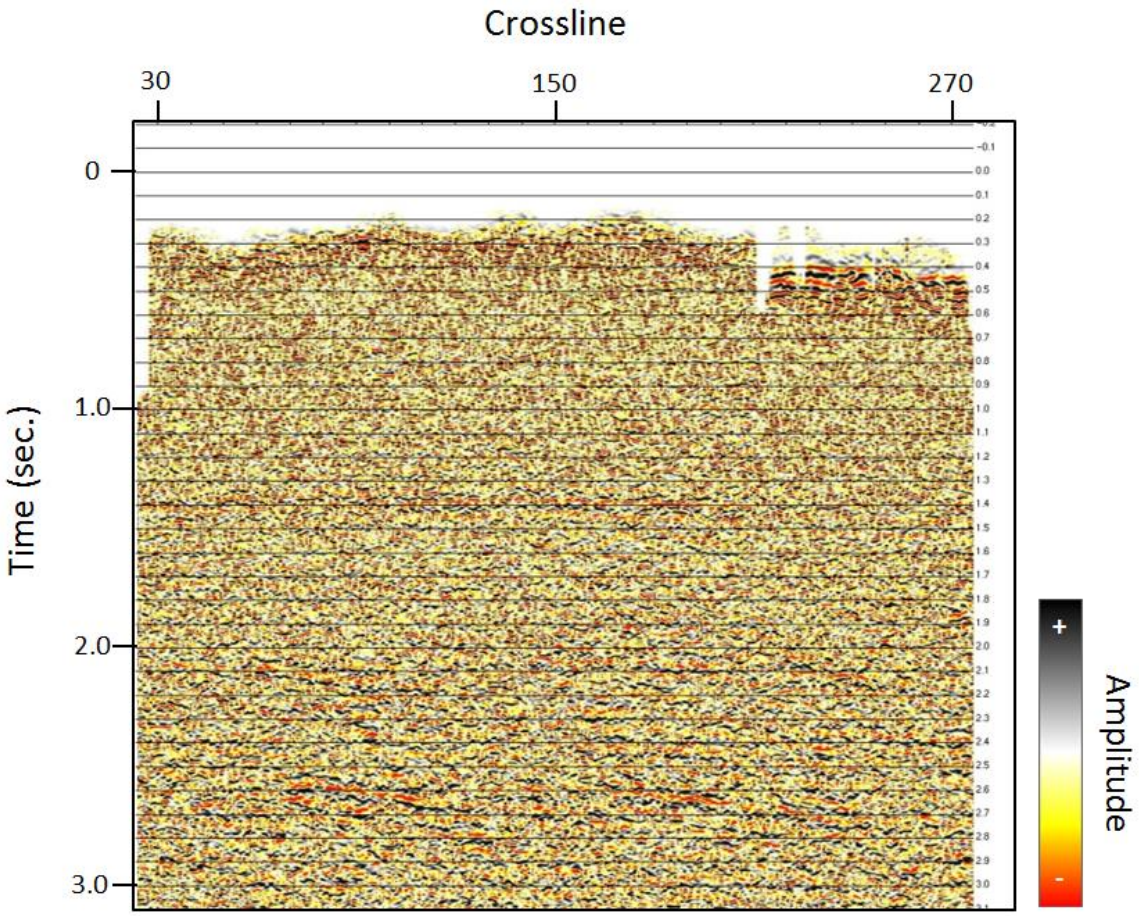

Figure 3.2.3 Tomostatics solution with RV=13,500 f/s and datum=8300 feet. The tomostatics solution provided the poorest results of the statics methods tested. All amplitudes are relative and thus unitless. (1 crossline = 110 feet).

Once settling upon the GLI two-layer refraction statics solution, the next step is noise suppression to clean up noise bursts, linear noise and ground roll. In Figure 3.2.4, a CDP gather can be seen before and after noise attenuation. The long-wavelength noise cone has effectively been removed from the data. This helps bring out signal that otherwise is washed out by the low- frequency noise. A difference gather ensures that primarily noise was removed (Figure 3.2.5).

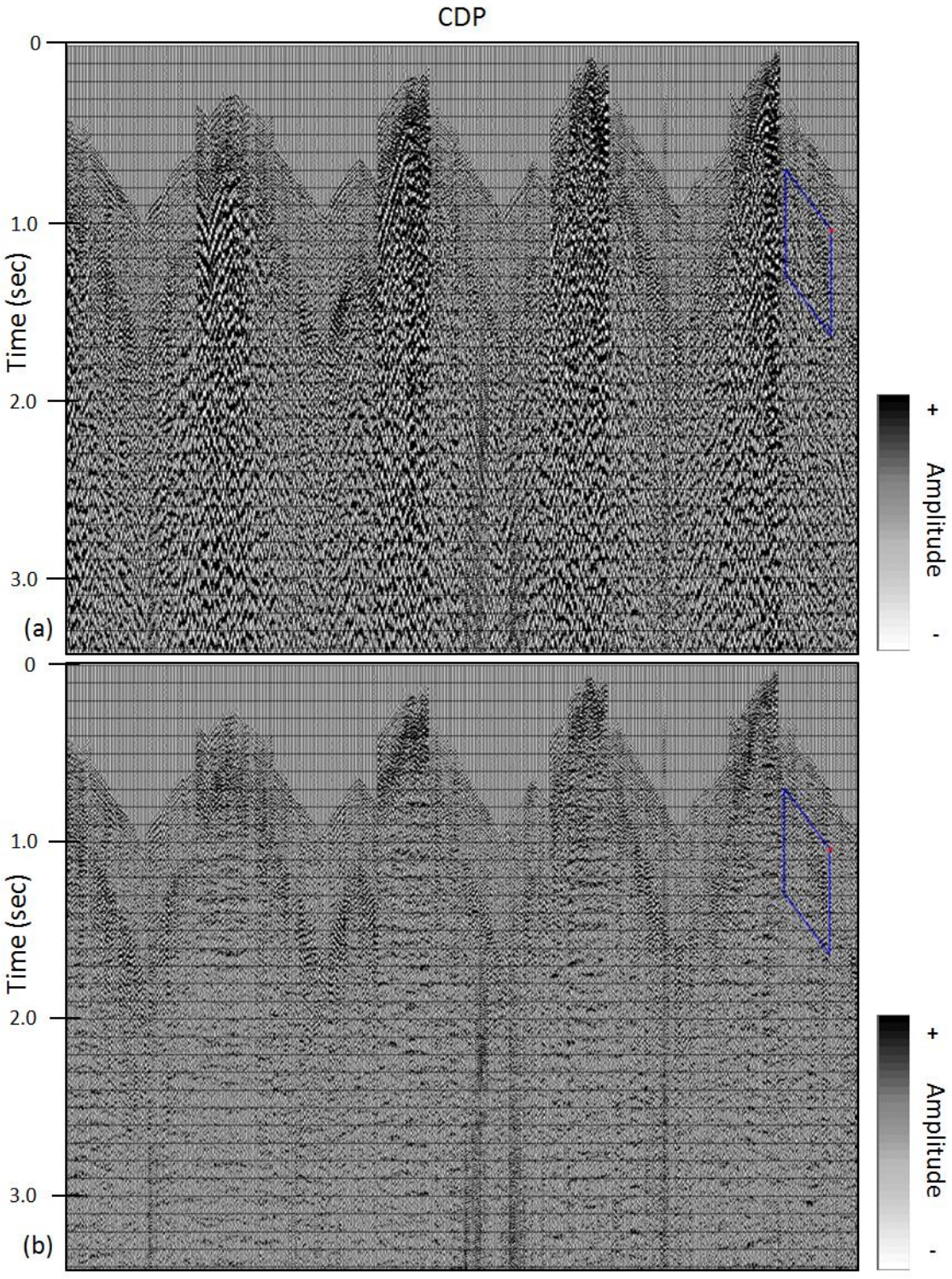

Figure 3.2.4 (a) before pre-deconvolution noise attenuation and (b) noise attenuated gather. Most of the long wavelength noise has been removed from the CDP gather. All amplitudes are relative and thus unitless.

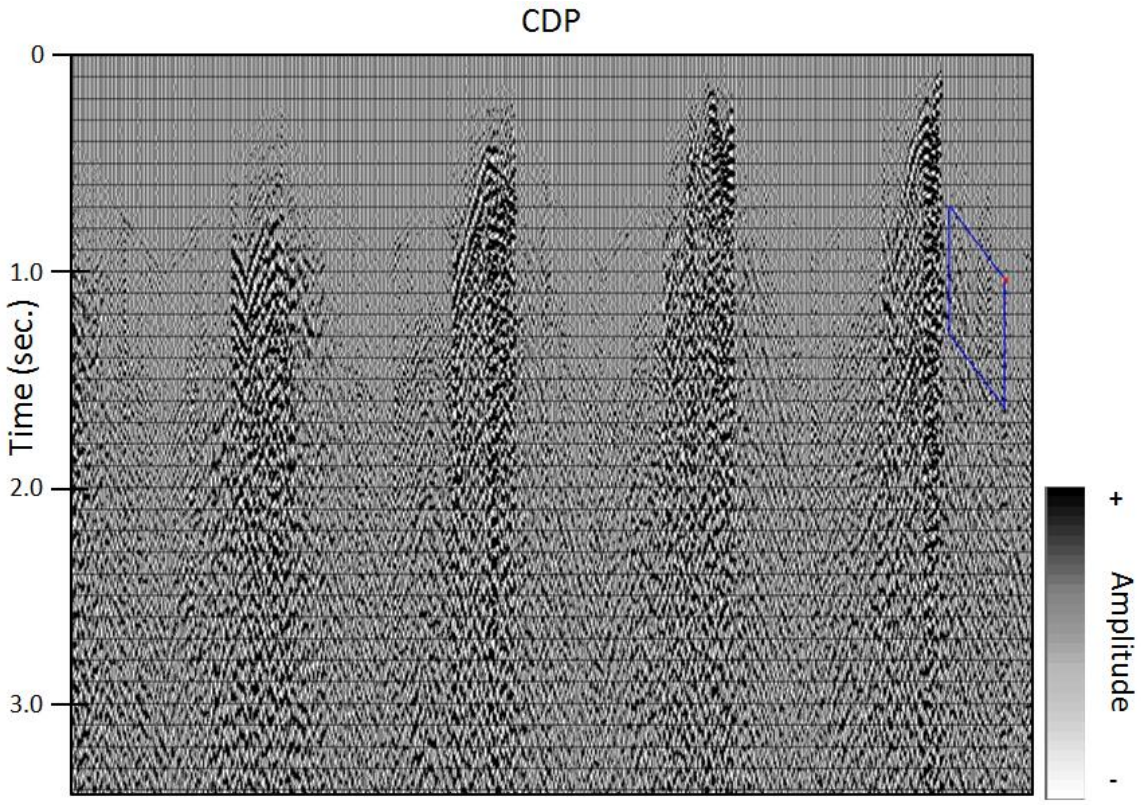

Figure 3.2.5 Residual gather of noise removed from Figure 3.2.4a. Mostly long wavelength noise has been removed and signal was unaffected. All amplitudes are relative and thus unitless.

Surface-Consistent Deconvolution

Yilmaz describes deconvolution as the process of compressing the seismic wavelet to increase the temporal resolution of seismic data (Yilmaz, 1987). A seismic wavelet that is more compressed decreases the "ringy" character in a stack and increases the resolution of a reflector or event. This involves inverting the convolution process that occurs as the seismic wavelet reflects from the reflecting boundaries. Figure 3.2.6 taken from *Practical Seismic Data Analysis (2014)* written by Hua-Wei Zhou visually describes this process in a synthetic example. The earth's reflectivity (a) convolved with a vibroseis (or dynamite) signal (b) gives the earth response (c). To get the recorded data to minimum phase (first step in the processing flow) we first take the minimum phase source wavelet (d) and convolve it with (c) which results in

synthetic data (e). The source (b) when cross-correlated with the synthetic data (e) eliminates the effects of the vibrator's amplitude spectrum resulting in (f). When auto-correlating the vibe signal we retrieve a Klauder wavelet (g) which then is converted to minimum-phase (h). The filter (i) needed for this conversion is computed by dividing (h) by (g). Convolving this filter (i) with (f), the minimum-phase version (j) of (f) is computed. Lastly, when (j) is deconvolved to become spikier the result is (l). The last trace (l) is what we are after in our deconvolution process.

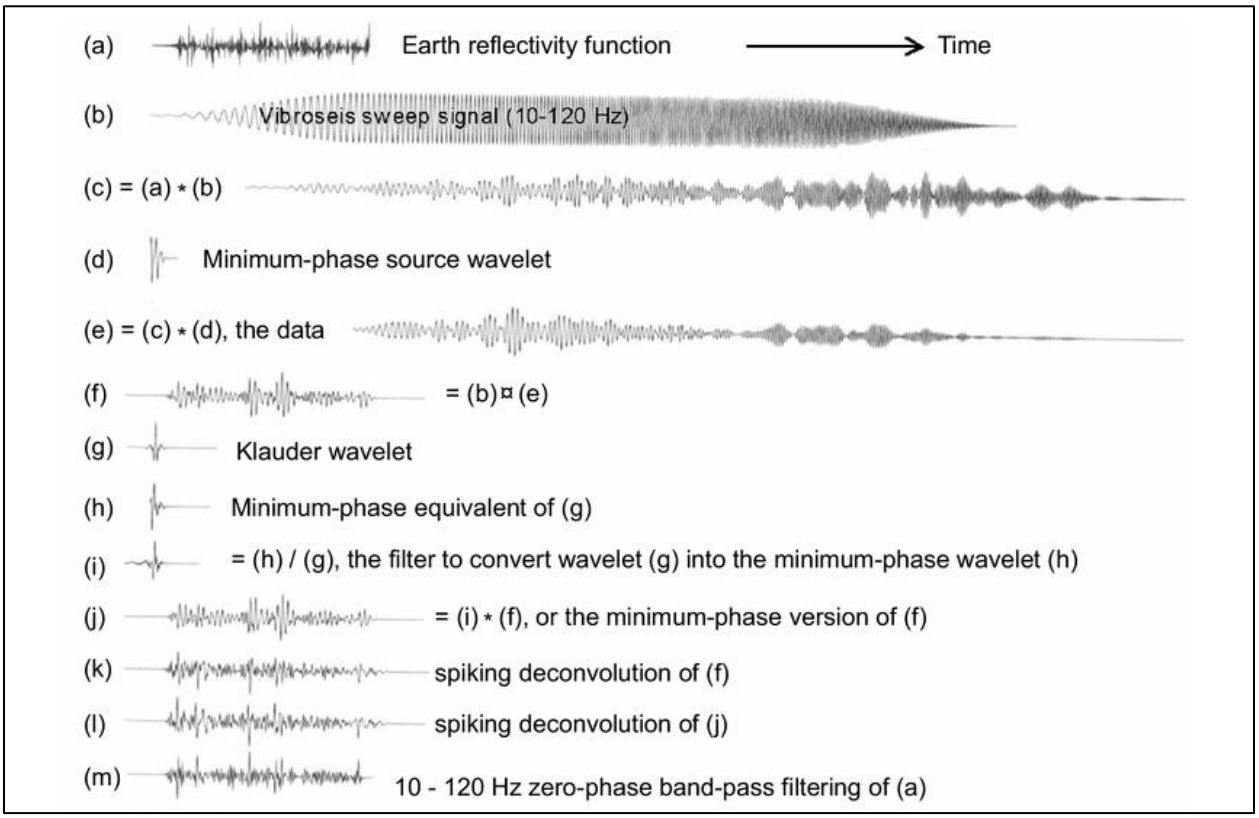

Figure 3.2.6 Convolution process (from Zhou, 2014) taken from (a) Earth's reflectivity function to (l) resulting trace from spiking deconvolution.

Spiking deconvolution inverts the convolution process by inverse filtering the wavelet to a band-limited spike (Zhou, 2014). To examine deconvolution, consider convolution model in equation form (3.1).

$$x(t) = w(t) * e(t) + n(t) \qquad (3.1)$$

where $x(t)$ is the recorded trace, $w(t)$ is the wavelet, $e(t)$ is what is the earth-reflectivity-series and $n(t)$ is the noise term. First, the noise term is ignored and it is assumed the earth reflectivity spectrum is white. Next, we define the earth reflectivity $e(t)$ is represented as the convolution of a filter $f(t)$ with the recorded trace $x(t)$ in Equation 3.2.

$$x(t) = w(t) * e(t) = w(t) * f(t) * x(t) \qquad (3.2)$$

Eliminating $x(t)$ from both sides of (3.2), leaves (3.3) where $\delta(t)$is equivalent to the dirac delta function.

$$\delta(t) = w(t) * f(t) \qquad (3.3)$$

If there were a perfect inverse to the wavelet (which there is not) it could be inverted using the z-transform and convolved with the Dirac-delta function $\delta(t)$ to retrieve the filter.

$$f(t) = \delta(t) * w^{-1}(t) \qquad (3.4)$$

If the system were infinite and not discrete, $f(t)$ would produce a spike when convolved with $w(t)$. In a finite discrete world, to predict the inverse filter that when convolved with the wavelet results in predicted signal $a(t)$ that is more compressed (Equation 3.5).

$$a(t) = f_{pred}(t) * w(t) \qquad (3.5)$$

a least-squares inverse filter $f_{pred}(t)$ is found that minimizes the error between the real output and a true spike (dirac-delta function). This inverse filter when applied to the wavelet produces a spikier version of the wavelet, much like going from (j) to (l) in Figure 3.2.6. This also potentially helps in removing obvious multiplies from the data by removing reverberations in the source wavelet. All of this results in an output that more resembles the earth reflectivity and eliminates unwanted noise (Zhou, 2014). Here, before performing the spiking deconvolution, a

surface-consistent amplitude scaling was applied. Spiking deconvolution was run in three iterations from 100-3200 milliseconds and zero-offset, next at 600- 3000 milliseconds and 3000 foot offset and last at 2000-3200 milliseconds and 16,100 foot offset using a window of 100 milliseconds for each operation. The results (Figure 3.2.7) overall show reflection events in the gather are sharper and more coherent after deconvolution. Some of the noise throughout the gather has been enhanced somewhat, but will be suppressed using further noise attenuation methods.

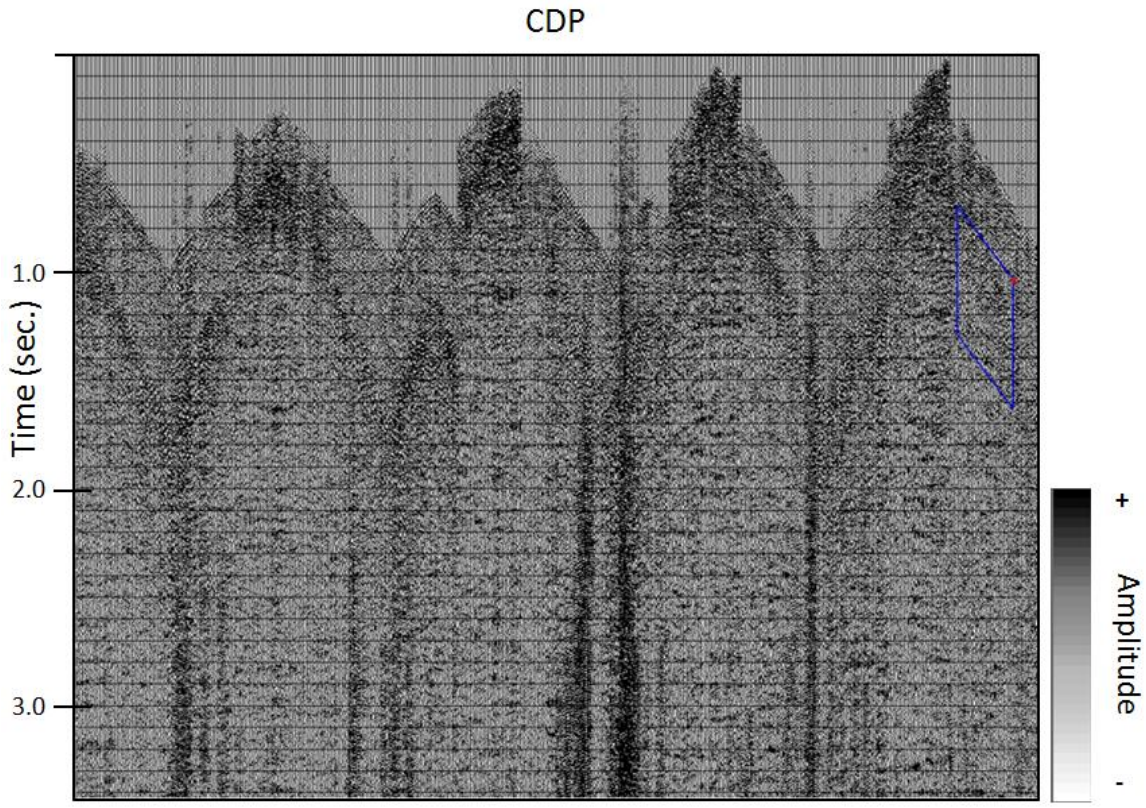

Figure 3.2.7 Results of spiking deconvolution showing useful events are now sharper and coherent. Further noise attenuation will be performed to remove noise boosted by spiking deconvolution. All amplitudes are relative and thus unitless.

Velocity Analysis

Post-deconvolution, normal move out (NMO) to the CDP gathers so reflection events are lined up as close to horizontal as possible so the data can be stacked effectively. Stacking velocities are picked on a semblance plot. Semblance is "a measure of cumulative amplitudes across seismic traces (Zhou, 2014)" This operation takes a raw CDP stack and computes the stacking velocity spectra via hyperbolic move out of reflectors (Biondi, 1992). The stacking velocity spectra are computed by taking the coherency of the hyperbolic paths of reflector amplitudes in offset and time (Biondi, 1992). When these values are summed together in a semblance plot, the most coherent (where energy is the highest and hyperbolically stacked together the best) is the location at which the stacking velocity will correct the reflections the best. On this plot, along the x-axis is the stacking velocity in feet per second and along the y-axis is the two way travel time. The location of the stacking velocity "pick" is placed where the coherency is the brightest. An example of one of these picks is pictured in Figure 3.2.8.

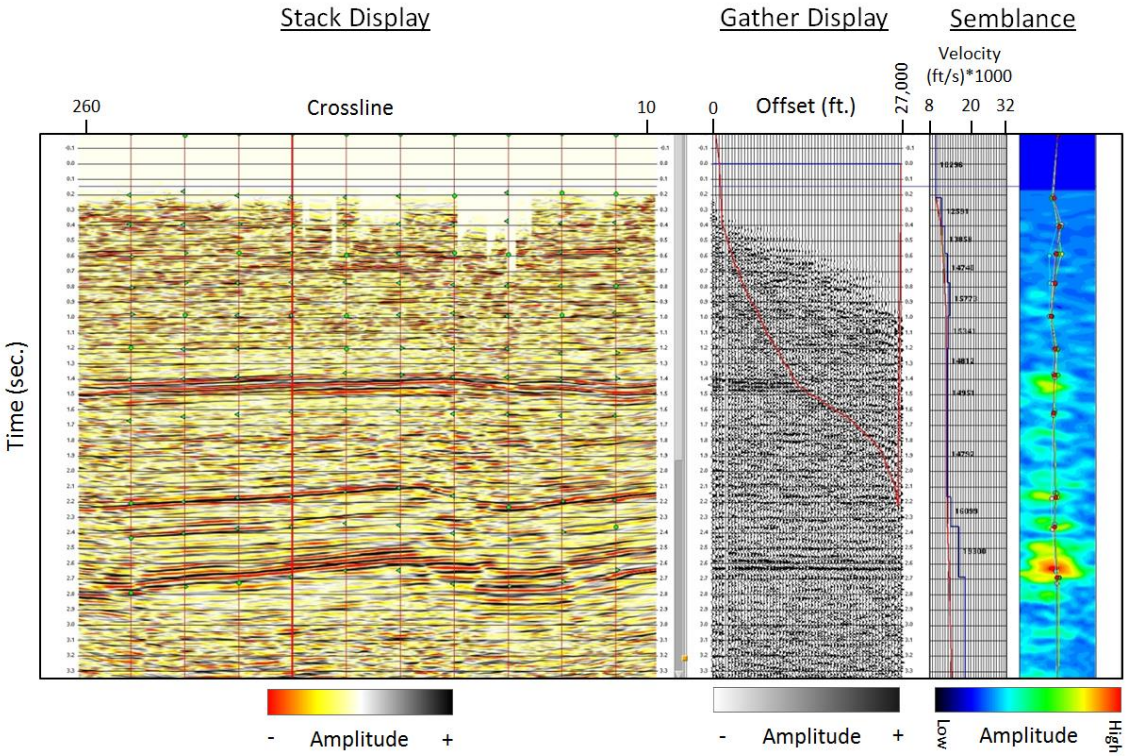

Figure 3.2.8 Example of velocity picking to improve imaging and fidelity of seismic data. In the left panel is the location on the stack of the particular pick. The middle panel displays this location as a CDP. In the right is a velocity function and semblance plot. Velocities are picked where the semblance is brightest as depicted by the overlying line. All amplitudes are relative and thus unitless.

In this study, velocities were picked at a spatial interval of every one-mile in the x and y direction. If the picked velocity is too fast, the event will be over-corrected and tail upward. Likewise, if the pick is too slow, the event will be under-corrected and curve downward. When these picks are correct, the event will line up horizontally, enhancing the stacked image of reflectors.

Residual Statics

Using the computed stacking velocities as interval velocities, further residual statics can be made. Although refraction and elevation statics correct for the bulk of static correction, some remnant static issues still exist from irregularities in reflected travel times from near-surface

anomalies like “large elevation changes, base of weathering layers and weathering velocities (Yilmaz, 1987).” The correction for residual statics is due to short-wavelength delays that are not corrected in refraction statics (Malehmir and Julian, 2010). In residual statics the goal is to estimate these travel time delays, t_{ij}, of a given reflection event via Equation 3.6 taken from Yilmaz (1987). Where s_j and r_i are the residual static shifts at the j^{th} source and i^{th} receiver location and G_k is the structure term at the k^{th} midpoint location. $M_k x_{ij}^2$ is the residual moveout at the k^{th} midpoint location where x_{ij}^2 is the shot-receiver offset.

$$t_{ij} = s_j + r_i + G_k + M_k x_{ij}^2 \quad (3.6)$$

The method of residual statics used is based on the cross-correlation maxima method. In this method, travel times of the delay are estimated by using a pilot trace and cross-correlating it with the NMO corrected traces (Yilmaz, 1987). The pilot trace used for the cross-correlation is a stacked trace from a selected window range (time gate). When the pilot (stacked trace) is cross-correlated with each individual trace in the gather the time shift, t_{ij}, corresponds to the maximum cross-correlation (Yilmaz, 1987). From this travel time delay, residual move out is calculated. Once the residual moveout is corrected, we reanalyze the velocity analysis in a second round to make any needed corrections. This process can be repeated multiple times. In this study, a second velocity analysis was computed every half-mile and a second pass of residual statics was run. In the first pass of residual statics, for the time interval of 300-3000 milliseconds correlation window of 36 milliseconds was used. For the second pass, the window was constrained to 12 milliseconds. The result of this analysis can be found in Figure 3.2.9. Once the velocity and residual statics are complete, the data was checked for phase rotation or bulk shift corrections.

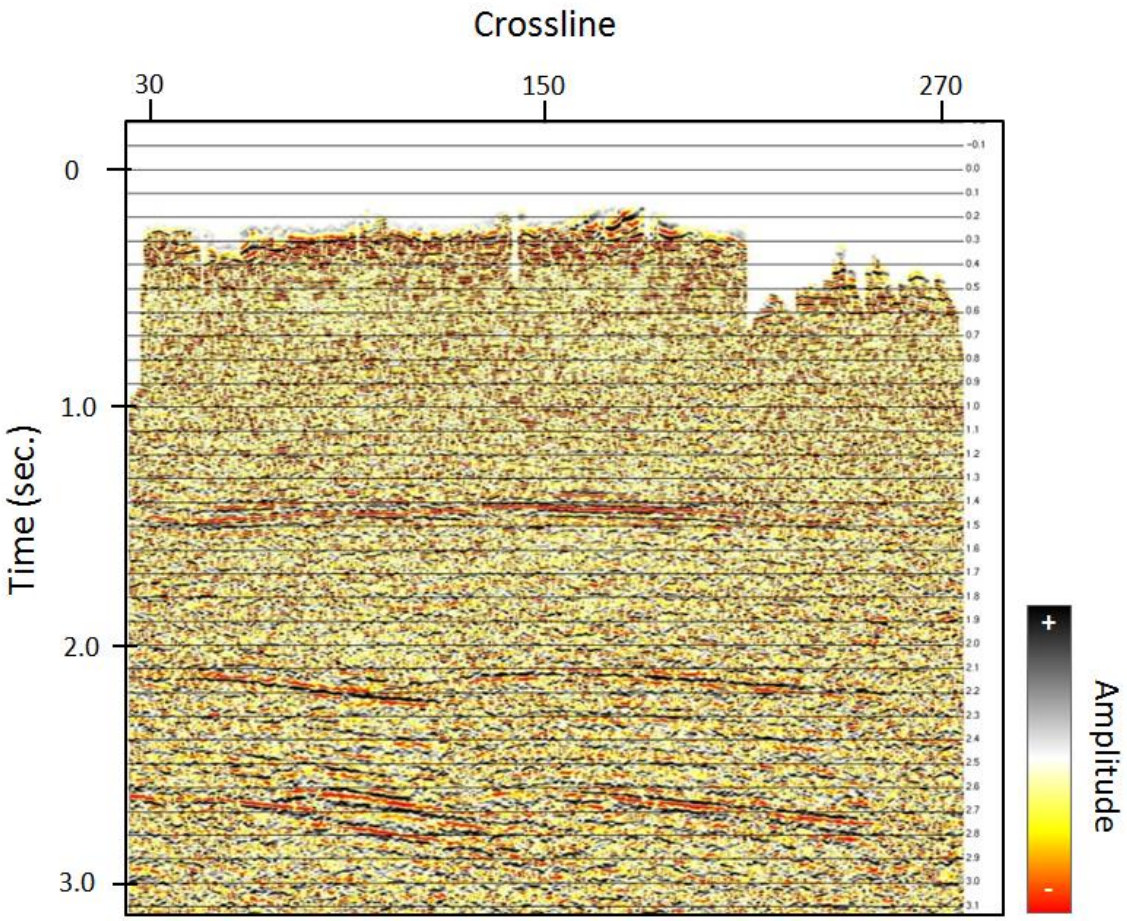

Figure 3.2.9 Results after two passes of velocity analysis and residual statics. All amplitudes are relative and thus unitless. (1 crossline = 110 feet).

Trim Statics & FX-Decon

After correcting the data for any phase rotations and bulk shift, trim statics are applied to flatten events on the gathers with tighter constraints. The goal of trim statics is to make small adjustments to any traces that were not corrected in residual statics. While residual statics focused on aligning major travel-time variations, trim statics focuses on minor variations. Like residual statics, it uses a maximum cross-correlation along a reflector with a window much smaller than residual statics. This window is usually a few milliseconds long. This corrects any subtle changes from trace-to-trace along a reflector and produces a more continuous event.

Lastly, we want to filter out anymore random noise to increase the SNR. This is accomplished using f-x deconvolution. A predictive filter is applied to the data to model signal and removes unwanted noise in the f-x domain. Figure 3.2.10 shows the results of trim statics and FX-deconvolution on a stacked image. Comparing this display to Figure 3.2.9, it can be seen that trim statics helped improve event continuity while the mild f-x deconvolution that was applied suppresses very little noise in the data. Since a vast majority of the noise is still present, additional denoising will be applied in the secondary processing flow.

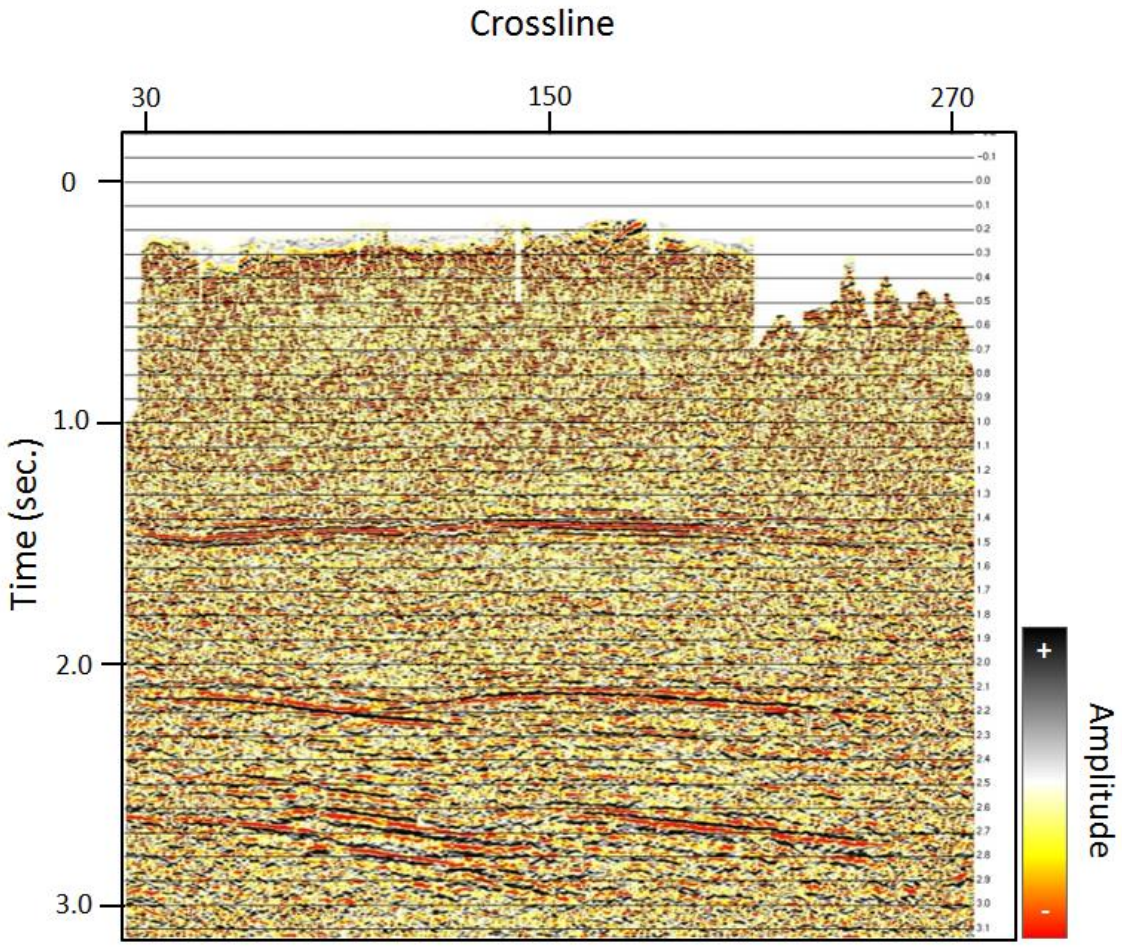

Figure 3.2.10 Trim statics and FX-deconvolution applied. Primary reflectors are more continuous laterally and the thrust fault becomes more coherent. All amplitudes are relative and thus unitless. (1 crossline = 110 feet).

3.3 Wavelet Packet Denoising

To this point in the processing flow, the pre-stack primary processing procedures have been completed. In traditional processing flows, the data could then be migrated (pre-stack or post-stack) and have further noise attenuation efforts made to enhance the SNR. Due to acquisition restraints in the survey, it was noticed early on that an aggressive noise attenuation technique would need to be performed pre-stack. Wavelet packet denoising was run to eliminate residual noise post deconvolution and statics. This was particularly an issue for gathers in the west over the Peter's Point anticline where the signal tends to be far offset and low-frequency. The particular denoising method used is a proprietary algorithm developed by GeoEnergy Incorporated in Houston, TX. Since the algorithm is proprietary, parameterization could not be shared. Here, we are merely concerned with how this technique improves the data from an interpretational point of view and will only briefly touch on the basic principles the method is built upon. The denoising process is based on using a set of wavelet packets (sometimes referred to as a "wavelet dictionary") with a best-basis search to reconstruct seismic data (Woog, Popovic and Vassiliou, 2005). In the wavelet analysis, the signal is decomposed with a library of adapted wavelets to obtain portions of the signal components that we desire. In wavelet analysis, the building block is a "mother wavelet" $\psi(x)$ that is a compactly supported function with a scaling b and translation a (Equation 3.7). The function $f(t)$which represents the data is decomposed via a wavelet transform into a set of basis functions (Equation 3.8). With an inverse wavelet transform, the data can then be reconstructed (Equation 3.9).

$$\psi^{a,b}(x) = |a|^{-0.5}\psi\left(\frac{x-b}{a}\right) \tag{3.7}$$

$$W_{\psi}(f)(a,b) = \frac{1}{\sqrt{a}}\int f(t)\psi\left(\frac{t-b}{a}\right)dt \tag{3.8}$$

$$f(x) = C_{\psi}\iint \langle f, \psi^{a,b}\rangle \psi^{a,b}(x)a^{-2}da\,db \tag{3.9}$$

Equations 3.7, 3.8, and 3.9 are all taken from Woog, Popovic and Vassiliou's (2005) publication. The signal is analyzed using scaled and shifted waveforms of the wavelet libraries and performing a local cross-correlation to hunt for either signal or noise components of the traces. In essence, we want to reconstruct two separate models of the seismic traces. One model that represents the unwanted components of the data (the noise model) and a second that reconstructs the useful information we want to keep (the signal model). Both models are built in iterations, where after each iteration the two models are used compared to one another, in an effort to remove their respective energy from one another (Woog, Popovic, and Vassilou (2005). To do this, a threshold is established to direct the algorithm to choose a basis that represents wanted energy to keep and unwanted energy that will be removed.

In the dataset, this was done with three different thresholds that will remove noise conservatively and moderately. In the conservative approach, the threshold was set so the denoising algorithm would only allow for coherent and continuous noise to be removed. This approach tries to eliminate major noise bursts meaning much of the random noise would still be present post-denoising. In the moderate version, the threshold was opened up so this random noise could be found in the gather and removed. This process was performed on unmigrated CDP gathers prior to 5-D interpolation with statics and NMO applied to the gathers. With the denoised gathers, one version (conservative or moderate) was selected and a third round of velocity analysis and residual statics was applied before the gathers are taken into 5-D interpolation. Figure 3.3.1 shows the same CDP gather before conservative denoising (left), after conservative denoising (center) and a residual gather (right). The raw gather on the left is littered with noise bursts that are vertically continuous throughout the entire gather. After

conservative denoising was applied, the noise bursts have been removed from the data, but some residual random noise still is present. In the residual display on the right, it can be seen that little to no signal was removed from the gather and the noise bursts are clearly displayed.

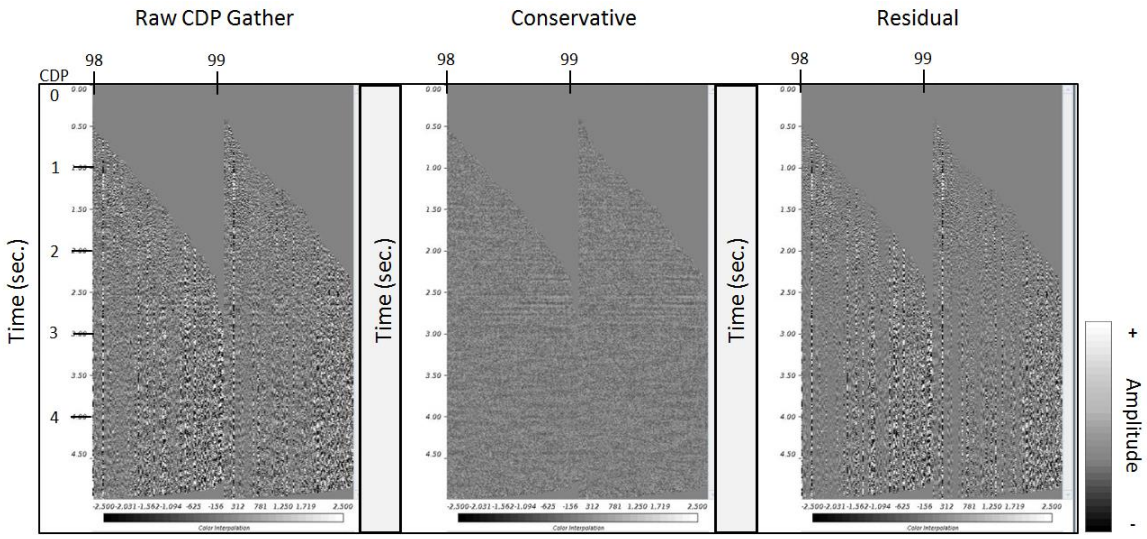

Figure 3.3.1 Conservative wavelet packet denoising on raw gather (left), denoised gather (center) and residual (right). All amplitudes are relative and thus unitless.

In an effort to remove the random noise that is still present, moderate denoising was performed. The same CDP gather with moderate denoising results is shown in Figure 3.3.2. Again, the raw input (left), moderately denoised (center) and residual (right) is displayed. In this iteration, the moderate version has more random noise removed from the gather. The reflections can be easily tracked and the residual shows little to no signal being removed.

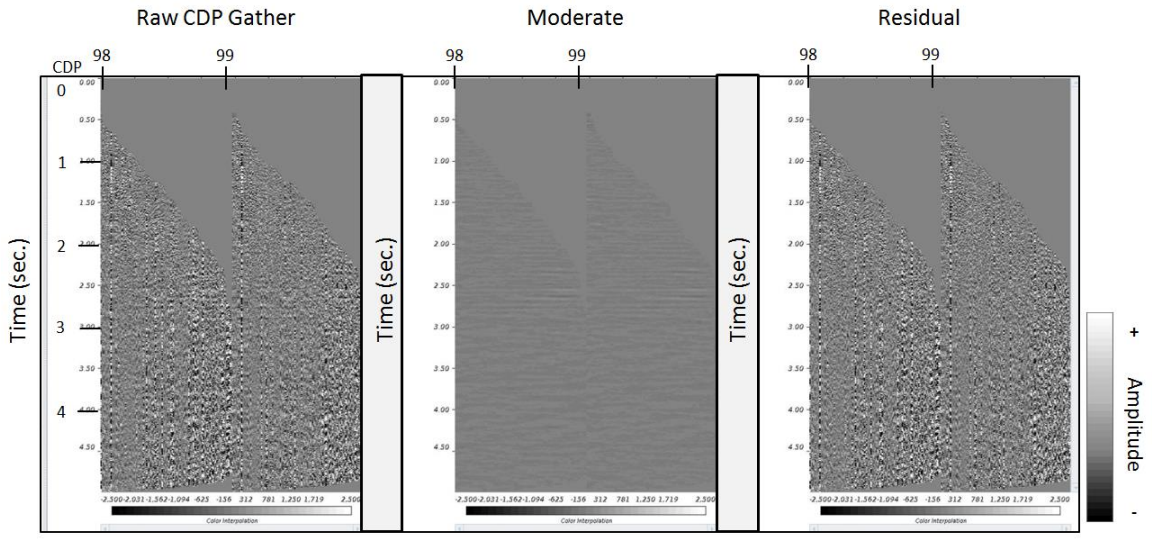

Figure 3.3.2 Moderate wavelet packet denoising on raw gather (left), denoised gather (center) and residual (right). All amplitudes are relative and thus unitless.

When this data is then stacked together, minor differences can be discerned when comparing the conservative to the moderate denoised versions. Figure 3.3.3 and Figure 3.3.4 show the result of stacking the conservative and moderate gathers respectively along inline 166. In both figures the raw stack is on the left, denoised version is in the middle and the residual is to the right. In Figure 3.3.3 the conservative approach causes some of the higher-frequency random noise to still be present in the stack. While in Figure 3.3.4, the events along the fault are better resolved and this noise is mostly removed.

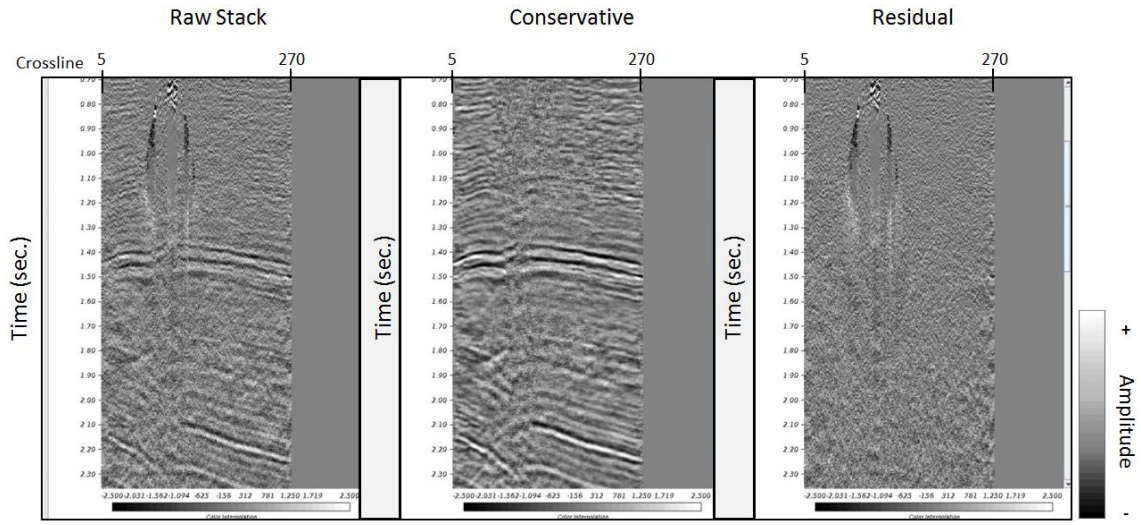

Figure 3.3.3 Conservative wavelet packet denoising on raw gathers and stacked for better visualization. Raw (left), denoised stack (center) and residual stack (right). All amplitudes are relative and thus unitless. (1 crossline = 110 feet).

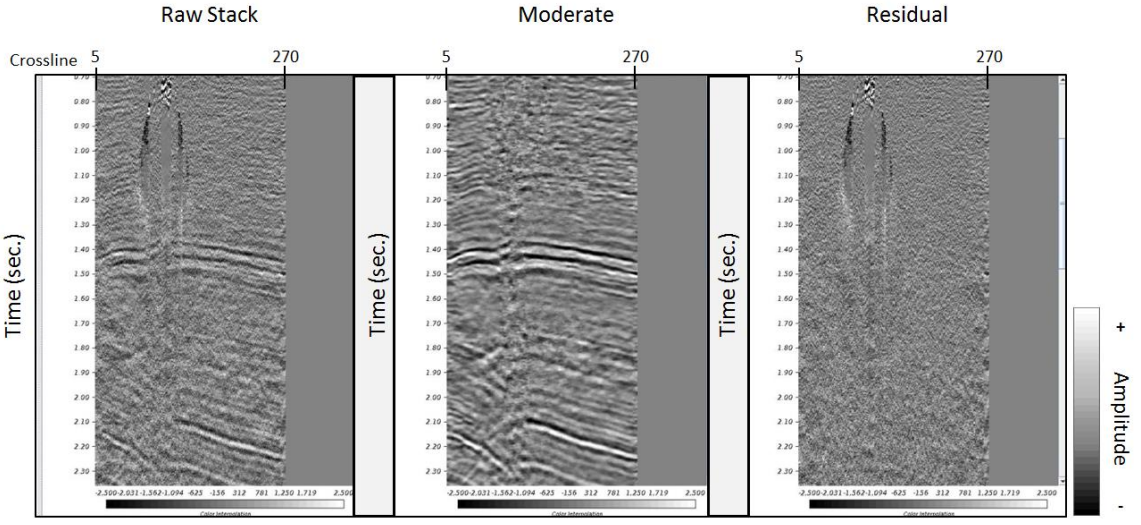

Figure 3.3.4 Moderate wavelet packet denoising on raw gather then stacked for better visual. Raw (left), denoised gather (center) and residual (right). All amplitudes are relative and thus unitless. (1 crossline = 110 feet).

Moving forward, the moderate denoised gathers were used to run the third pass of velocity analysis and residual statics. These gather were only used in the velocity and residual analysis and the result of these third passes were applied to non-denoised gathers for 5-D interpolation. After performing an additional velocity analysis and residual statics, the velocity

picks were not altered most over a majority of the survey. Figure 3.3.5 compares a stack along crossline 250 where (a) is the original stack with second pass of residual statics applied and (b) is the revised version of the stack after third round of velocity analysis and residual statics.

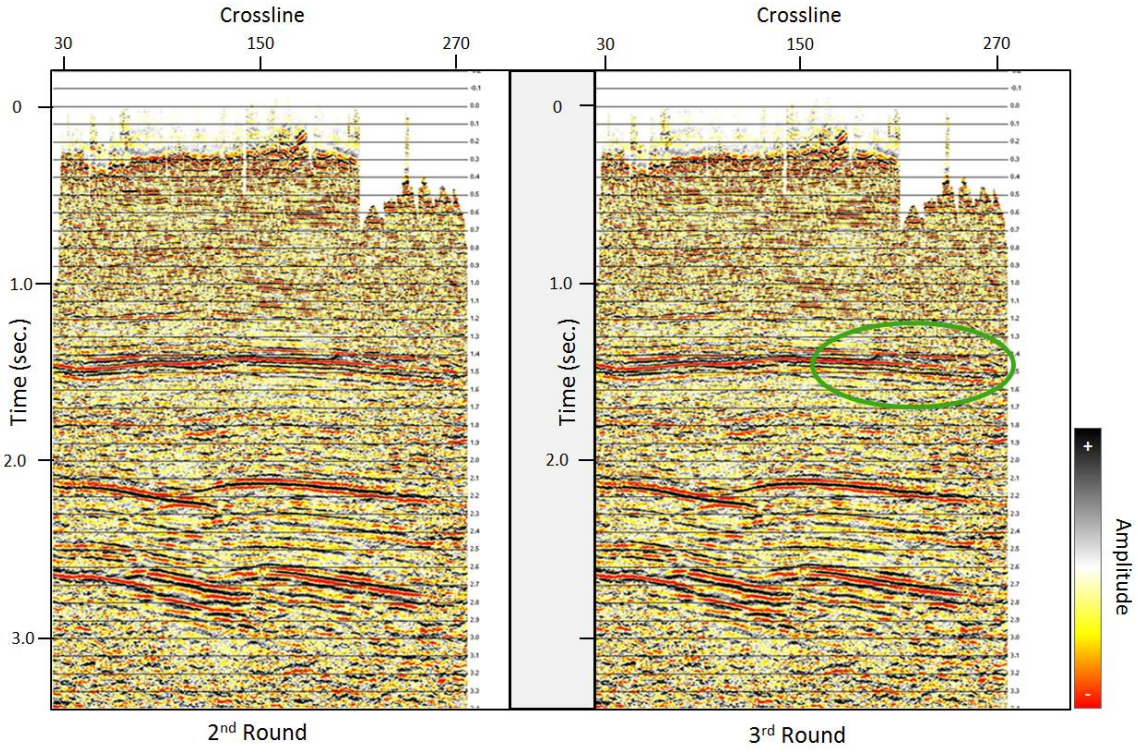

Figure 3.3.5 Comparison of 2nd round of velocities and residual statics with the third round. Not very many obvious uplifts were achieved but minor improvements have been made. All amplitudes are relative and thus unitless. (1 crossline = 110 feet).

No game-changing improvements were achieved, but subtle improvements can be seen circled in green. Trim statics were then applied to the data (see Figure 3.3.6). Again, no major changes have been made but the subtle changes between the stacks leads to more continuous reflectors in areas circled in red.

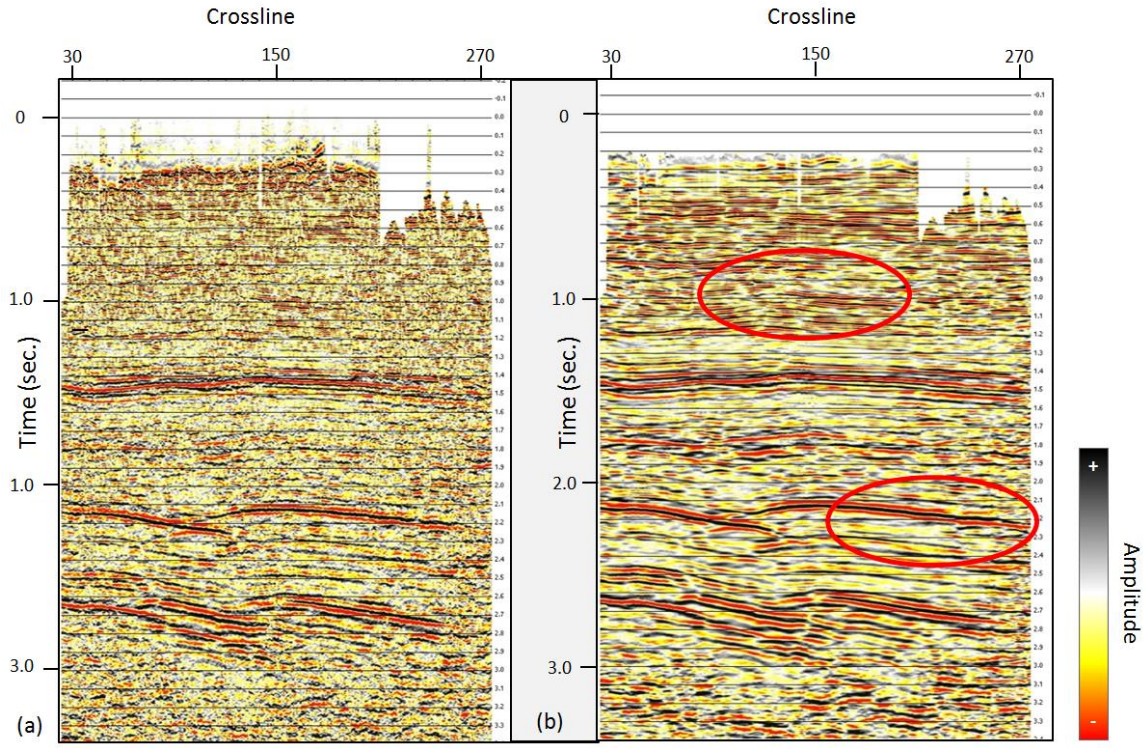

Figure 3.3.6 Comparison of the (a) original stack with trim statics applied and (b) revised trim statics with updated velocity analysis and residual statics. All amplitudes are relative and thus unitless. (1 crossline = 110 feet).

3.4 Five-Dimensional Interpolation

Before the data was migrated five-dimensional (5-D) interpolation was applied to fill in gaps in the data and help repair irregular traces. 5-D interpolation operates in the five seismic domains; inline, crossline, azimuth, offset and time/frequency. Seismic data tends to be very well sampled in certain directions but is under-sampled in others. These holes can be caused by unrecorded azimuths and offsets in seismic gathers or under-sampling in the crossline direction (Marfurt and Chopra, 2013). Marfurt and Chopra (2013) showed that seismic attributes (coherence, curvature, etc.) greatly benefit from 5-D interpolation when seismic footprint is suppressed and SNR is increased. The goal of 5-D interpolation is to come in and fill these holes by interpolating seismic traces from neighboring areas to the gaps of missing data. When this

data is interpolated into gaps, we want to make sure not to smear any discontinuities (faults, karst, channels, etc.) the data may hold. By doing this, we hope to increase the SNR and provide increased lateral resolution of seismic reflection events.

5-D Interpolation Background

Although there are differing methods to interpolating a seismic trace, each comes back to a simple model proposed by Liu and Sacchi (2004). This model requires solving a complex system of equations to take real data (**d**) and interpolate it into an unknown model (**m**) via a sampling matrix (**T**) in Equation 3.10 that has been altered from Liu and Sacchi (2004) and Trad (2009).

$$\mathbf{m} = \mathbf{T}\mathbf{d} \qquad (3.10)$$

where **m** is a length-M vector of data sampled at $\mathbf{m} = (\mathrm{m}_1, \mathrm{m}_2, \mathrm{m}_3, \ldots, \mathrm{m}_\mathrm{M})$ and the observations **d** are given by $\mathbf{d} = [\mathrm{m}_{\mathrm{n}(1)}, \mathrm{m}_{\mathrm{n}(2)}, \mathrm{m}_{\mathrm{n}(3)}, \ldots, \mathrm{m}_{\mathrm{n}(\mathrm{N})}]$. The position of known samples is given by η where $\eta = \{\mathrm{n}(1), \mathrm{n}(2), \mathrm{n}(3), \ldots, \mathrm{n}(\mathrm{N})\}$. The sampling matrix **T** is defined as $T_{i,j} = \delta_{n(i),j}$ and δ is the Kronecker delta. To properly and accurately interpolate the data, a constraint is made in the frequency domain. The interpolated data must have the same multidimensional spectrum as the original data (Trad, 2009). To do this, we take a CDP gather in the t-x domain and transform it into the frequency domain via the Fourier Transform. Each trace is then interpolated in the spatial domain (x) for each temporal frequency (*f*) or frequency slices (Liu and Sacchi, 2004). At every frequency slice, a cost function is defined and minimized to ensure the data being interpolated matches a predicted model. Both the discrete (DFT) and fast (FFT) Fourier transforms can be used, but due to costs and computing time the algorithm produced by Arcis Seismic Solutions uses an FFT. In an FFT, the data has to be binned into a grid with exactly one trace per location (Trad, 2009). The bin interval must be kept small enough to

avoid smearing data, but usually the existing CDP bins can be used. This binning has already been done in the geometry assignment and the same bins will be used for our analysis.

In Equation 3.11 we use the FFT to transform the data in multidimensions from the t-x domain to the f-x domain. Equation 3.12 then defines the inverse FFT where *H* denotes the complex conjugate transpose and $\mathbf{F}^H = \mathbf{F}^{-1}$. **M** is the unknown data (**m**) in the frequency domain.

$$\mathbf{M} = \mathbf{F}\mathbf{m} \qquad (3.11)$$

$$\mathbf{m} = \mathbf{F}^{\mathrm{H}}\mathbf{M} = \mathbf{F}^{-1}\mathbf{M} \qquad (3.12)$$

To solve for this unknown data (**m**), the cost function (**J**) is defined frequency by frequency as Equation 3.13,

$$\mathbf{J} = \|\mathbf{d} - \mathbf{T}\mathbf{m}\|^2 + \boldsymbol{\lambda}\|\boldsymbol{m}\|_{\boldsymbol{W}} \qquad (3.13)$$

where $\|\ \ \|^2$ is an *L_2-norm* and $\|\ \ \|_{\mathbf{W}}$ is an *L_W-weighted norm* and $\boldsymbol{\lambda}$ is a hyperparameter that controls the balance between fitting the data and enforcing sparseness on the spectrum (Trad, 2009). The *L_W-weighted norm* is calculated by Equation 3.14 below. In the equation, $\mathbf{m}^{\mathrm{H}}$ is the complex conjugate of the model **m**, $\mathbf{p}_k$ is the multidimensional spectrum of the unknown data at wave index **k** and $\mathbf{F}_n$ is the multidimensional Fourier transform with *n* number of spatial dimensions of the data (Trad, 2009).

$$\|\mathbf{m}\|_{\mathbf{W}} = \mathbf{m}^{\mathrm{H}}\mathbf{F}_{\mathrm{n}}^{-1}|\mathbf{p}_{\mathrm{k}}|^{-2}\mathbf{F}_{\mathrm{n}}\mathbf{m} \qquad (3.14)$$

The vector $\mathbf{p}_k$ contains weights defined in the temporal frequency-wave number domain (or ω-**k** domain) that link the frequency slices where the interpolated trace has the same support and shape to those of the signal to interpolate (Liu and Sacchi, 2004; Trad, 2009). Although the frequency domain acts as the fifth-dimension, the interpolated data is done in the spatial

domain meaning it is more accurately a 4-D interpolation. Therefore, the model **m** is in the ω-**x** domain and **x** is a vector defined by inline, crossline, azimuth and offset. By using a minimum-weighted norm method, the data will try to find a location in the observed data closest to the model that best represents the predicted data.

Another restriction to the interpolation is then made to define how far the algorithm can look in the spatial domain to "grab" data for the model. This restriction, known as the *culling factor,* ensures the model has as little change to fidelity as possible. The culling factor (C.F.) is simply the Euclidean norm (square root of the sum of the squares) of the number of bin distances a trace was away from our interpolated location (Equation 3.15). Bin distances are given a value from zero to infinity where one bin distance is equivalent to the bin spacing.

$$C.F. = [(inline\ bins)^2 + (crossline\ bins)^2 + (azimuth\ bins)^2 + (offset\ bins)^2]^{\frac{1}{2}} \quad (3.15)$$

For instance, if one defines an interpolated trace(*f) as* a function of bin distances and a trace is interpolated from a data point located at one inline, zero crossline, one azimuth and one offset bin away, the resulting culling factor is:

$$f(inline\ bins, crossline\ bins, azimuth\ bins, offset\ bins)$$

$$f(1,0,1,1)$$

$$C.F. = \sqrt{1^2 + 0^2 + 1^2 + 1^2} = \sqrt{3} = 1.73$$

The culling factor can also range from zero to infinity. A culling factor of zero means the data is in its original form, or that no interpolation was performed. A culling factor of infinity (often called *no-culling*) means the algorithm was allowed to search an unlimited extent of bins to find an original trace for interpolation. No-culling and zero-culling are often confused with one another, but are complete opposites. Selecting the culling factor is the most important part of 5-

D interpolation. If the algorithm is under-culled, the missing data will not fully be interpolated. If the data is over-culled, the interpolated data may come from a location that is not consistent with the model location. This will greatly affect the fidelity of the data. Finding a healthy balance where the data is interpolated precisely is done by running tests on ranges of culling factors. Culling factor testing is broken into single bin distance increments going from 0 to infinity($0-1, 0-2, 0-3, \ldots, 0-\infty$). With each iteration, the interpolated data tends to be more complete until a point where little to no change is seen. This point is typically where the culling factor cut off is selected. As a QC for the interpolated data, a leakage display is used to make sure no signal was removed. A leakage plot is a residual plot that first takes the interpolated traces with no-culling and produces a fully synthetic version of the data. This data is then subtracted from the original data that has the interpolated traces with the given culling factor included.

5-D Interpolation on Stone Cabin 3D

The changes in topography and acquisition geometry resulted in large gaps in the near-offsets of the CDP gathers on the Stone Cabin 3D. 5-D interpolation was used to fill in the offset gaps and correct traces that have low SNR. The 5-D interpolation was performed on the pre-stack moderately denoised CDP gathers (corrected for NMO) before migration had been carried out. Five different culling tests were performed with culling factors of (1) C.F. from 0-1 (2) C.F. from 0-2 (3) C.F. from 0-3 (4) and C.F. from 0-4. The original input (un-interpolated) gathers were compared to the five culling factors test to decide the proper culling factor for interpolation. Figure 3.4.1 illustrates the result of each culling factor test up to a C.F of 0-4 on a CDP gather (located at inline 600 and crossline 250) with data holes due to a neighboring valley.

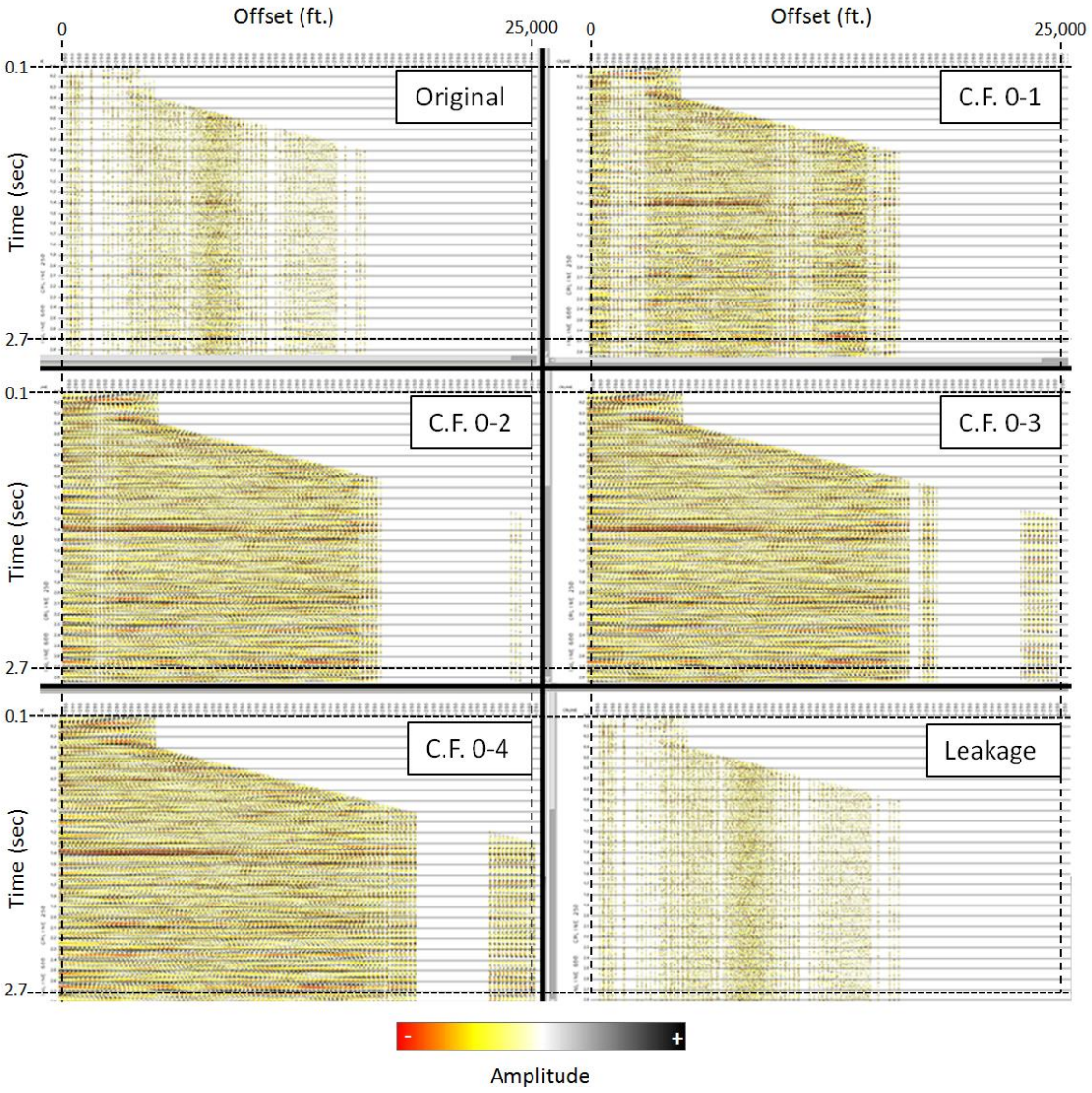

Figure 3.4.1 5D interpolation culling factor (C.F.) test from original, 0-1, 0-2, 0-3, 0-4 and leakage. At a C.F. of 0-3, most of the relevant data is filled in. The leakage plot shows very little signal being removed from the gather. All amplitudes are relative and thus unitless.

As the culling factor increases from 0-1 to 0-4 these holes are progressively filled in. At a culling factor of 0-3 nearly all the near-offset gaps are filled in and the reflectors are aligned. Moving past a culling factor of 0-3 to 0-4, the data shows no obvious change. For this reason, a culling factor of 0-3 was used to execute 5-D interpolation over the entire 3-D survey. The data were then stacked and a leakage plot produced confirming that no useful signal had been lost

and anything removed can be classified as noise. Figure 3.4.2, shows the tremendous uplift 5-D interpolation provided to the stack when comparing the original data (*3.4.2a*) and the interpolated model (*3.4.2b*).

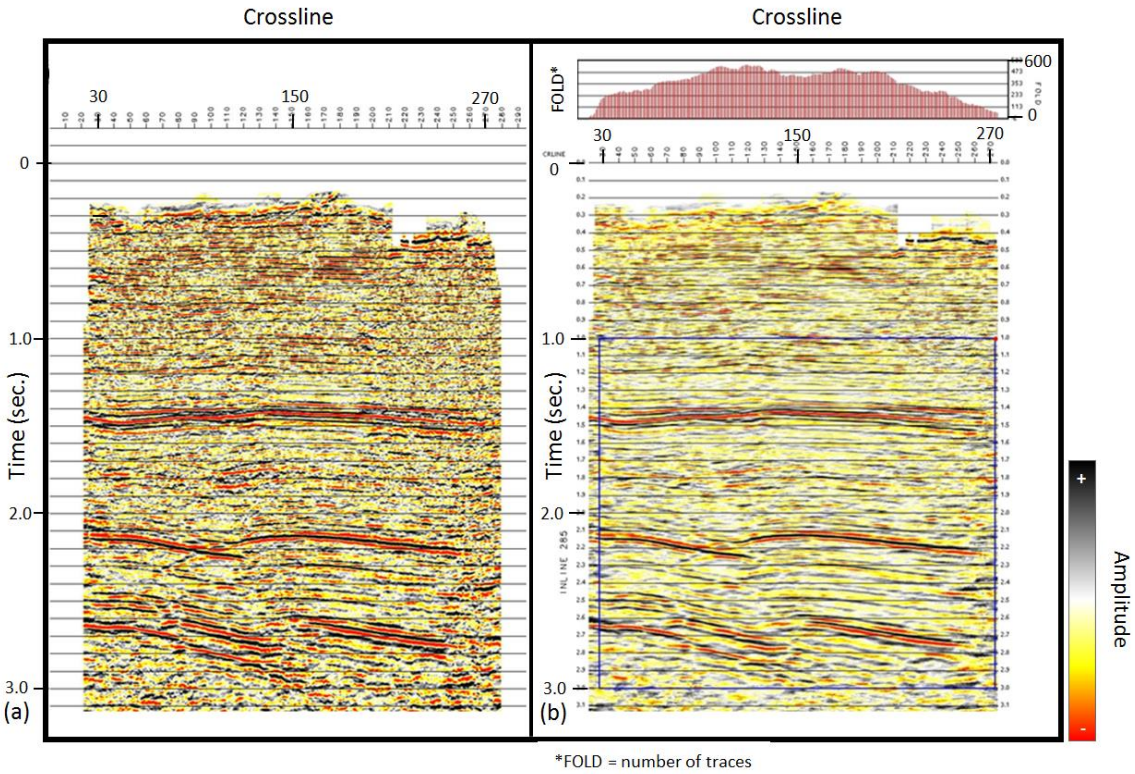

Figure 3.4.2 Comparison of (a) input to 5D interpolation and (b) a 5D interpolated stack. Above (b) a plot of the fold shows the increase with 5D interpolation has added to our survey. Also, the reflectors are more laterally continuous and some noise has been removed. All amplitudes are relative and thus unitless. (1 crossline = 110 feet).

3.5 Pre-Stack Migration, Post-Migration Denoising & Angle Muting

Kirchhoff Migration

With the improved 5-D interpolated CDP gathers with a culling factor from 0-3 applied, a pre-stack Kirchhoff migration was performed to adequately place the events in their proper spatial location and increase the fidelity of the seismic data. In particular, the objective was to correct data where reflectors are steeply dipping and diffractions off these events cause the

data to be in an improper location. These diffractions are caused by a phenomenon known as *Huygens's Secondary sources* that produce hyperbolic shaped responses in the t-x space when a traveling wave meets a reflector (Yilmaz, 1987). The impact of the initial wavefront on the dipping event acts as a secondary point source with energy propagating in a hyperbolic path. When the amplitudes at each point are then summed along this hyperbolic path and moved to zero-offset, a correct positioning of the data can be achieved (Yilmaz, 1987). This is termed the diffraction summation method of migration which Kirchhoff migration is built upon. The method collapses the hyperbola by summing the amplitudes along the hyperbolic path and shifting it to the apex of the hyperbola. According to Yilmaz (1987), three factors that affect amplitudes along hyperbolic propagation must first be corrected before the Kirchhoff diffraction summation migration is performed.

1. The amplitude response of the diffracted wave varies with propagation angle making the amplitudes angle-dependent. An *obliquity factor* correction that describes the angle dependence of amplitudes must be made by finding the cosine of the angle between the z-axis (vertical and zero-offset) and the direction of propagation.
2. The diffracted waves also experience a *spherical spreading* f*actor* that describes the spherical divergence of the amplitudes as the diffracted wave propagates. The spherical spreading factor is proportional to $(1/vr)^{1/2}$ for 2-D propagation and $(1/vr)$ for 3-D propagation, where r is the distance from the source to the wavefront and v is equivalent to the root-mean-squared (RMS) velocity.
3. The diffracted wavelet response has a certain phase and frequency characteristic. The waveform that results from the summation along the hyperbolic path must be restored in phase and amplitude. This correction is termed the *wavelet shaping factor*. For 2-D

propagation, this wavelet shaping factor is designed with a 45-degree constant phase spectrum and an amplitude spectrum equal to the square root of the frequency. For 3-D propagation, a 90-degree phase shift is used and the amplitude is equal to the frequency.

Once these three corrections are made, the Kirchhoff migration method multiplies the input data by the obliquity and spherical spreading factor and a filter (with the predetermined specifications) is applied. The method then sums along the hyperbolic path and places the result at the apex of the hyperbola where $\tau = t(0)$ (Yilmaz, 1987). This process leads to three corrections in the time section that properly place the reflected event in its true location. Migration (1) steepens reflectors, (2) shortens reflectors and (3) moves reflectors in the updip direction.

A Kirchhoff migration can be done either pre-stack to the CDP gathers or post-stack to a stacked section. In the past, when computation power was limited, post-stack migrations were more common. With advancements in computation power migration is now usually applied pre-stack. Performing migration on pre-stack gathers results in a more accurate solution but is much more expensive. Lastly, migration typically responds to 5-D interpolated data better for the simple reason that interpolated data is more complete. When migration is performed on the non-interpolated gathers false migration "swings" are then introduced where data is missing. For these reasons migration was applied pre-stack to non-denoised gathers with 5-D interpolation (see Figure 3.5.1). When compared to the unmigrated stacks in Figure 3.4.2, the steep reflector along the thrust (reverse) fault at 2.1 seconds is steepened and the reflector can now be tracked from the upthrown flank to the downthrown flank. Migration has also helped the continuity and fidelity of multiple events in the vertical display, especially at 1.0 – 1.2

seconds. Before migration, this shallow event could hardly be tracked (Figure 3.4.2); with migration applied (Figure 3.5.1) the package is coherent and continuous laterally. However, since the input gathers to migration did not have the wavelet packet denoising applied; a fair amount of high frequency noise is still present in the data making it look ringy. To eliminate this noise a second pass of wavelet packet denoising was run pre-stack on CDP gathers that had both 5-D interpolation and Kirchhoff migration applied.

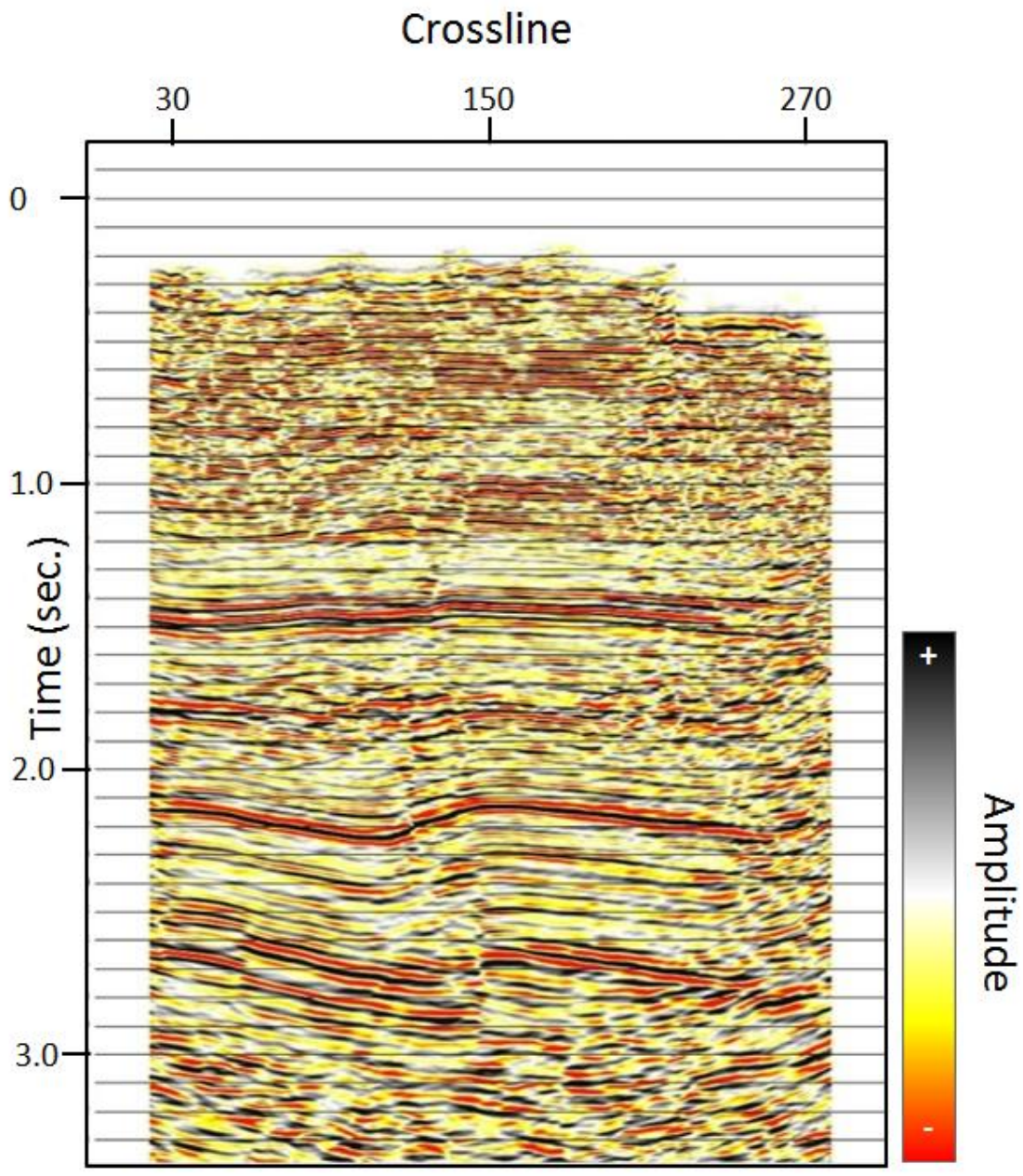

Figure 3.5.1 Kirchhoff migration results with 5D interpolation. Faults are easily trackable and overall lateral continuity has improved. All amplitudes are relative and thus unitless. (1 crossline = 110 feet).

Post-Migration Wavelet Packet Denoising

The first round of denoising was only used for a third round of velocity analysis and a third pass of residual statics prior to 5-D interpolation. The 5-D interpolation was then run on pre-stack CDP gathers with the third velocity analysis and residual statics applied and without the denoising solution applied. Therefore, the remaining residual noise remains in the gathers. To attenuate the residual noise, a second round of the wavelet packet denoising was performed in three iterations – conservative, moderate and aggressive. The threshold was altered in each of the three cases to allow for the wavelet dictionary to either replicate unwanted data by searching primarily for noise bursts (conservative), search for continuous random noise and noise bursts (moderate) and search for anything that could be considered noise (aggressive). While the aggressive denoising theoretically should give the best result, it can be very detrimental to wanted signal. When signal is not horizontally flat and continuous, the wavelet packet analysis will replicate it as noise and remove it from the gather. To illustrate this, we look at a gather in the most severe case that is extremely noisy. The results of the conservative, moderate and aggressive denoising iterations are seen in Figure 3.5.2 along with the raw input gather. In the raw gather (*3.5.2a*), large amounts of both low and high frequency noise dominate the gather.

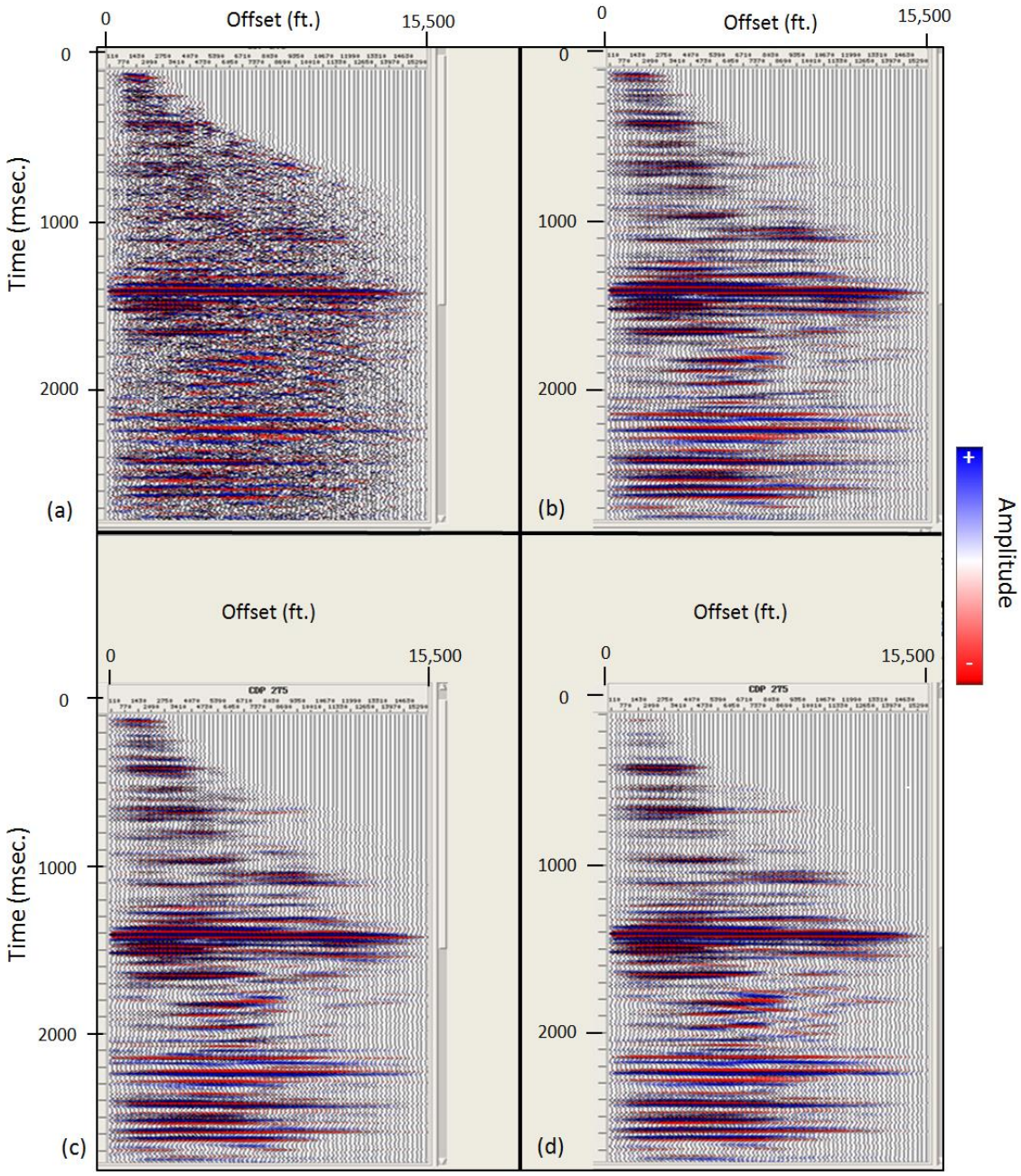

Figure 3.5.2 Comparison of (a) raw stack, (b) conservative denoising, (c) moderate denoising and (d) aggressive denoising. All gathers are post-5D and post-migration. All amplitudes are relative and thus unitless.

When a conservative denoising is applied (*3.5.2b)*, the near offset noise bursts are mostly removed along with some residual random noise. The reflectors (signal) are now horizontally continuous and easily trackable. However, some residual high-frequency noise is still left. In the

moderate denoised (*3.5.2c*) the bulk of this high-frequency random noise is now removed and reflections are more pronounced. Moving to an aggressive denoised approach (*3.5.2d*) anything that can be considered noise is almost entirely removed and the deeper reflectors are a little flatter and horizontally continuous. Yet, highlighted by the green circle in the shallow portion of the gather, some of the shallow reflectors we can interpret in Figure 3.5.2c have now been removed. When the gather is then stacked, there will be almost no signal in the shallow sector. This leads to the decision of using the moderate denoised gathers as the input moving forward. The conservative denoised gathers did not remove all the unwanted noise and the aggressive denoising removed what can be interpreted as signal. In the moderate denoised solution the component that is clearly interpreted as noise has been removed and the signal has been enhanced. Using the moderate denoised gathers with 5-D interpolation and Kirchhoff migration, is a last attempt to remove unwanted noise pre-stack. A pre-stack mute is then used to eliminate any far offset tails that will degrade the quality and resolution of the stack.

Post-Denoising Angle Mutes

In the last step of processing to increase the SNR and seismic resolution of the entire dataset a far angle mute was applied. A mute is a method commonly used in processing flows to attenuate noise by zeroing out parts of the gather that are unwanted. This could be noise associated with ground roll, noise bursts, residual move out tails, etc. A mute can be applied by either using an inner mute fused on removing ground roll, an outer mute focused on removing noise past reflection events or a polygon mute that targets noise in a specific area. Mutes are usually made as time-offset pairs where processors will manually place picks in the time-offset domain (t-x domain) that are connected by straight lines with a muting criteria given (i.e. mute anything inside or outside these picks).

To keep things consistent through the entire dataset, a constant-angle mute was applied to the gathers. For seismic AVO analysis work, angle mutes are applied from the surface rather than final datum with the consideration of how amplitudes vary at different angles. However, the processing flow is not geared toward seismic AVO analysis but rather seismic resolution. We chose to apply these mutes from the final datum since the datum is higher than the highest topographic elevation. This means the start time of the gathers is delayed from a few milliseconds to hundreds of milliseconds depending on topographic location. When the mute is then applied, it is done so at a constant-angle from the final datum. This allows the mute to reach further offsets in the shallow section where the near-offsets are thousands of feet away and have limited the number of traces.

These mutes are applied at the surface using the pre-stack time migration (PSTM) velocity volume generated during Kirchhoff migration. PSTM velocity analysis was conducted after migration, but is discuss it in this section due to application timing. In PSTM velocity analysis, RMS velocities are broken into blocks at each major reflection event to save computing time. The RMS velocity blocks are calculated by stripping the NMO correction from the migrated gathers and performing a velocity analysis in the same manner discussed in Section 3.2. In this PSTM velocity analysis, manual velocity picks were performed every half-mile in the inline and crossline direction from datum and let the program use our picks as a guide to automate picks between our manual picks. This results in a PSTM velocity volume that defines RMS velocities for each block. For quick QC, the PSTM velocity volume was inspected to see if the RMS velocity blocks imitate the overall structure.

The location in offset that produces the desired mute angle was calculated using these RMS velocities. For the first layer, a simple straight-ray tracing method where the tangent of the

angle is equal to the offset location in feet divided by the depth of the first layer (d_1 in equation 3.16) is used. Here t_1 is equal to the time it took the wave to travel to the base of d_1 times the RMS velocity of the first layer (Equation 3.17). Substituting 3.16 into 3.17 and rearranging, the offset distance needed to achieve the desired angle can be found (Equation 3.18).

$$\tan(\vartheta) = x/d_1 \qquad (3.16)$$

$$d_1 = t_1 V_{RMS_1} \qquad (3.17)$$

$$x = \tan(\theta)\, t_1 V_{RMS_1} \qquad (3.18)$$

Snell's Law is used for subsequent layers. The ray parameter, p, is given by the Equation 3.19. Taking the NMO travel-time equation (3.20) and differentiating t in terms of x gives the ray parameter of the NMO travel-time equation (3.21). Substituting this equation back into Equation 3.19 and rearranging gives the equation needed to calculate the offset location for the specified angle (Equation 3.22).

$$p = \frac{\sin(\theta)}{V_{int}} = \frac{dt}{dx} \qquad (3.19)$$

$$t^2 = t_0^2 + \left(\frac{x^2}{V_{RMS}^2}\right) \qquad (3.20)$$

$$\frac{dt}{dx} = \frac{x}{tV_{RMS}^2} \qquad (3.21)$$

$$x = \frac{tV_{RMS}^2 \sin(\theta)}{V_{int}} \qquad (3.22)$$

In these equations, t is the travel time to the base of the layer and V_{int} is calculated using V_{RMS} by using the Dix Equation. Once the angles have been calculated at each RMS velocity block, data at large offsets are muted out. Three separate angle range mute tests were performed on gathers using a tight mute (0-25 degrees), a moderate mute (0-35 degrees) and an open mute (0-55 degrees). Any data that is not between these mute ranges was muted out

(zeroed) for each case. Figure 3.5.3 displays a set of gathers with each of the three mute tests overlaid. In our analysis, we see that using a tight 0-25 angle mute eliminates a large portion of the data in the shallow time section. A tight mute also eliminates useful signal from 1400 to 2400 milliseconds.

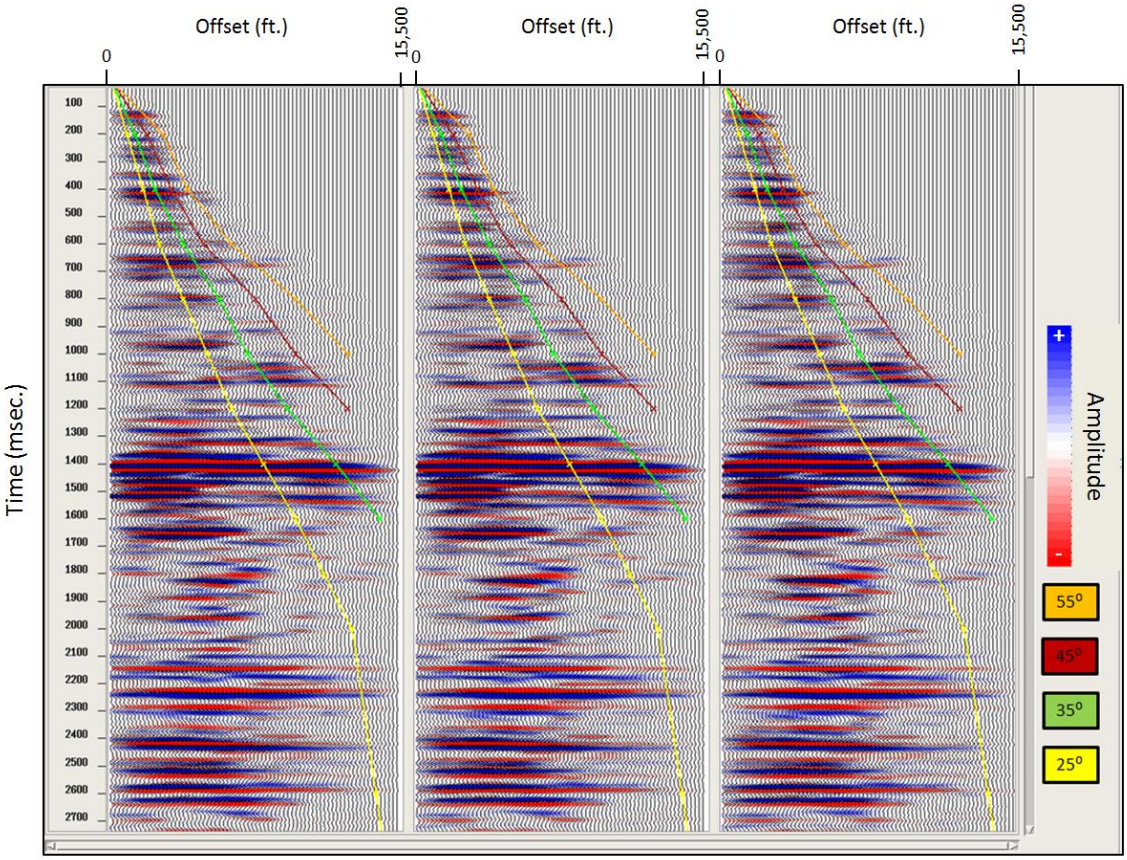

Figure 3.5.3 Angle mute tests conducted on a gather from datum (8300 ft.). Degrees range from 0-25 (yellow), 0-35 (green), 0-45 (red) and 0-55 (orange). All amplitudes are relative and thus unitless.

The moderate 0-35 degree mute does a little better job of including these shallow events from 500-1400 milliseconds and captures deeper events (1400-2400 ms) while eliminating the unwanted noise as well. The open 0-55 degree mute preserves almost all the data in shallow section but comes with the cost of including all the outside noise in the deeper

section. Considering the goal is to preserve shallow reflections while still eliminating the outside noise in the deeper section, the moderate 0-35 angle mute was selected.

Section 3.6 Initial Processing Wrap-Up

To this point every processing tool used was geared toward providing a solution with better SNR, vertical and horizontal resolution, and data fidelity over the entire vertical section. Primary processing procedures that must be performed in any processing flow were combined with secondary procedures. Secondary procedures (4-D wavelet packet denoising, 5-D interpolation and angle mutes) helped dramatically in removing unwanted noise, filling in data gaps due to acquisition restraints and enhancing reflection continuities.

Early in the processing flow, it was realized that to achieve the high SNR in the data a truly AVO compliant workflow could not be followed. Without boosting and scaling the amplitudes, amplitude decay with time makes picking velocities virtually impossible. There is simply not enough coherence between the decayed amplitudes to provide a semblance display where one can confidently pick velocities. In some cases, the semblance may not even be strong enough to make a showing. Thus, the non-AVO-compliant noise suppression was necessary to increase continuity of reflectors and resolution for thin beds and enhance fault imaging by cutting down on the amount of noise in the initial data set.

Chapter 4 Well Log Control and Thin Bed Enhancement

4.1 Well Log Interpretation

It is known that geologic well logs provide the best resolution vertically, but fail to provide good horizontal coverage. Inversely, seismic data provides excellent horizontal sampling but poor vertical resolution. In this chapter, well logs are used to interpret vertical layering. To this point in the study the main focus has been to provide a seismic data set that overall has better signal-to-noise ratio (SNR), vertical resolution, and event continuity. With this data, we can analyze how the local structure evolved over time. This was done by focusing on the entire data set in the processing flow instead of one interval. Now, the study shifts to a focus on resolving the Navajo sandstone (Jurassic in age) so accurate structure and isopach maps can be produced. To understand the seismic response of the Navajo interval, we first need to understand the geologic interval as revealed by well log data. Using a well log (named "Type Log") from outside our study area as a type log, formation tops were picked in the eight wells that penetrate the Navajo. Once formation tops were picked, two wells that have well-behaved sonic logs were used to tie the well logs to the Stone Cabin 3D and horizons were picked at major continuous boundaries. A dynamic depth conversion was then performed to place the other 6 wells at appropriate time-depth locations that correlate to the picked horizons. Altogether, this allows us to locate the Navajo interval on the seismic data. Using this information as a guide, spectral whitening and low-frequency spectral shaping were applied to enhance the data in the interval to resolve the Navajo sandstone on the seismic data.

Before picking formation tops, the logs were divided into either open hole or cased hole groups. An open hole well log is run before the well has been cased or cemented. With an open hole well log, the instrument is exposed directly to the rock formation and provides a more

accurate reading in gamma ray, resistivity, and density porosity logs. In some instances, borehole stability requires the log to be run after casing and cementing. This places an unnatural barrier between the instrument and the formation which results in skewed or inaccurate tool readings. Therefore, we will give open hole logs a higher importance. The Type Log used was to make picks at the eight well locations that can be seen in Figure 4.1.1a located in the back.

To properly orient the successive picks, a key surface was used as a vertical mark in all ten well logs. Typically, erosional unconformities, marine flooding surfaces and transgressive surfaces are good marks for vertical orientation as they are obvious and continuous throughout an entire section. The Dakota Silt marker was used as the key surface for orientation. The beginning of the Dakota Silt is marked by a marine flooding surface that abruptly separates shale above to sand below. The top of the Dakota Silt is marked by a sudden low gamma ray and high resistivity reading. In the well-to-well cross section in Figure 4.1.2 (fold out in back pocket), the marker is in red in all eight wells and the type log. A secondary marker was placed at the Entrada formation that indicates another abrupt change from shale to sandstone, where the neutron and density porosity come together and sonic (slowness) decreases.

With these marker picks, the Dakota, Morrison and Curtis formations were correlated between the Dakota Silt and Entrada. At the base of the Entrada formation, a low-resistivity response and separation of neutron and density porosity indicates a change to clay-rich shale. This clay-rich shale is the Carmel formation which directly overlies the Navajo sandstone providing a dense, low-porosity hydrocarbon seal. This shale is important in the future when analyzing the seismic response of the Navajo. Below the Carmel, the Navajo sandstone is marked by a low gamma ray, low resistivity and a neutron-density porosity cross over. When neutron porosity crosses density porosity, this indicates the formation may be filled with

hydrocarbons. When a formation is filled with gas, this results in an apparently low neutron reading from absorption of neutrons by the gas. Figure 4.1.1b shows the mnemonics and shading used for the well-to-well correlation.

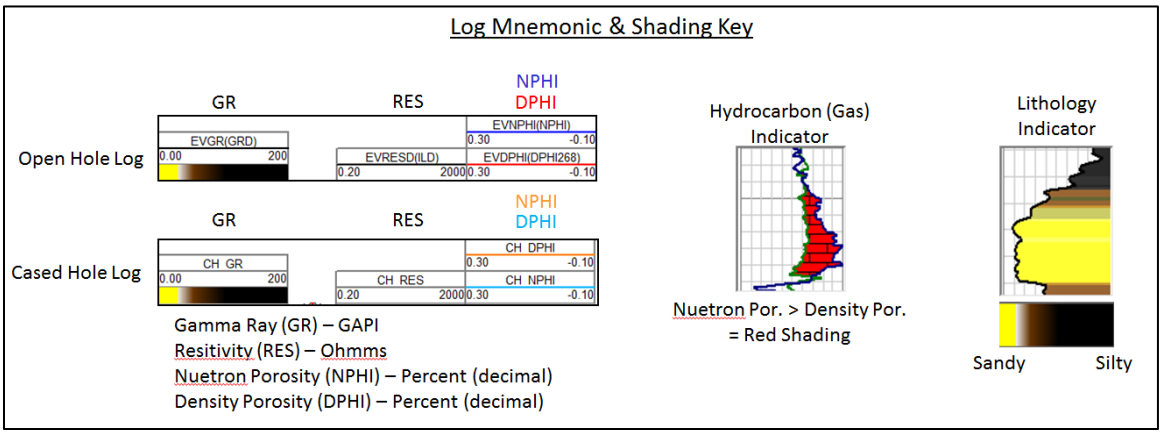

Figure 4.1.1b Mnemonics and shading used for well-to-well correlation. Lithology is roughly shaded using the gamma ray curve. When neutron porosity crosses the density porosity is shaded red to indicate the presence of natural g

This apparently low neutron reading causes the log to crossover the density porosity log when they are laid over each other at the proper scale. This is also reflected in the resistivity log which exhibits moderate to low resistivity reading in the presence of porous sands. Based on the crossover of the neutron and density porosity logs, the Navajo is then broken into two parts (lower and upper) based on their respective reservoir quality. The lower Navajo formation top is placed approximately halfway where there occurs larger neutron-density porosity cross over and a slightly lower resistivity reading. At the base of the Navajo interval, the Kayenta is marked by a much higher resistivity reading. The Kayenta is marine deposited formation composed of shales and sandstones with interbedded limestones.

Using what we know about the Carmel, Navajo and Kayenta formations we correlate these picks from the type log to the remaining nine wells. Over the Peter's Point gas field, where

all of the current production data comes from, the Navajo sandstone is stratigraphically thinning and thickening. In Figure 4.1.3 (fold out in back pocket), a well-to-well cross section shows the sand thins by approximately 15 feet from Well 2 to Well 4 and continues to thin to the Well 7. From Well 7 to Well 8, the upper Navajo was eroded away, leaving only the lower Navajo section. In Well 8, the entire Navajo package is only 20-30 feet thick. From the Peter's Point anticline (east) to the Prickly Pear anticline (west), the Navajo becomes relatively thicker. In order to map this stratigraphy, seismic data must be brought in to provide a more complete picture.

4.2 Navajo Sandstone Resolution

In order to map the Navajo interval on seismic data, we must first use synthetic seismograms to locate the Navajo (and other formations) on the seismic section. A synthetic seismogram is created by convolving a wavelet with a seismic impedance profile to predict the resulting seismic response on the seismic data. Using a check shot survey from a nearby well, an initial time-depth curve is applied. The synthetic trace is made by taking a density and inverse of the sonic slowness and multiplying them together to retrieve an impedance profile (Eqn. 4.1), where the inverse of the slowness is proportional to the velocity.

$$Impedence = \left(\frac{1}{sonic\ slowness}\right)(bulk\ density)$$

$$I = v\rho \qquad (4.1)$$

Next we extract a statistical wavelet around the borehole matched in frequency to the seismic data. This wavelet is then convolved with the reflectivity series, *r(t)*, derived from the impedance profile to give a synthetic trace (Eqn. 4.2).

$$w(t) * r(t) = synthetic\ trace \qquad (4.2)$$

This synthetic trace is then cross-correlated with the true seismic response to give a cross-correlation value between 0 and 1, where 1 is a 100-percent match. The synthetic trace is then bulk shifted and stretched or squeezed in time until the correlation coefficient is at a maximum. In typical synthetic ties, noise in the seismic traces prohibits a perfect tie with the synthetic trace. A successful tie, therefore, can be as low as 30-40%. A synthetic tie was made at the Type Well location that had well behaved sonic and bulk density logs and was vertical (not deviated). In Figure 4.2.1, the analysis is displayed with the extracted statistical wavelet. This was first done with the moderately denoised and 35 degree angle muted stack (prior to enhancement) data set was discussed in Chapter 3. Ass well logs indicate that moving from the Carmel, which is a dense shale, into a clean porous sandstone results in a decrease in impedance. When this decrease is large enough (as is our case) the resulting seismic response produces a trough.

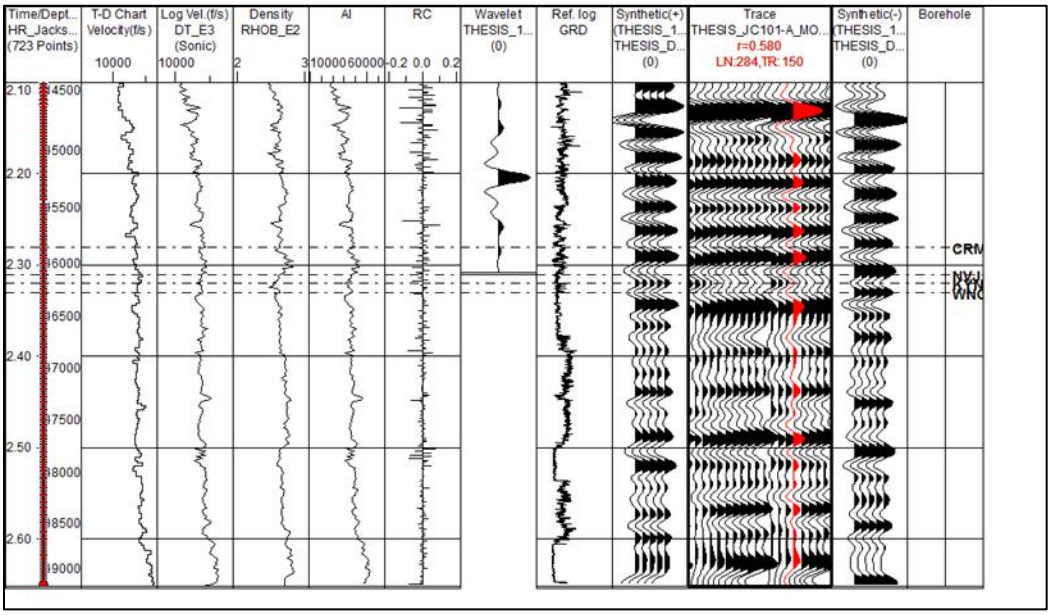

Figure 4.2.1 Synthetic well tie on the Type Log (vertical well) after 5D interpolation moderate denoising, and angle muted (0-35 degrees). The Kayenta (KYNT) peak is barely to non-visible with the current data. Further tertiary processing techniques are needed. All amplitudes are relative and thus unitless.

This proves to be accurate at the synthetic location. However, the underlying Kayenta formation is hardly visible in the data. As the clean Navajo sandstone meets hard shale at the base, this generates a peak at the Kayenta. In the type log synthetic, this peak is hardly seen. Taking an arbitrary line through four wells (Figure 4.2.2) it can be seen that the Kayenta cannot be mapped. This leads to the need of performing further post-processing enhancement with the objective of resolving the peak at the Kayenta. To do this, simple processes are applied in the frequency domain to boost frequencies in the data. These processes are known as spectral whitening and spectral shaping which are tertiary processing techniques in the processing flow.

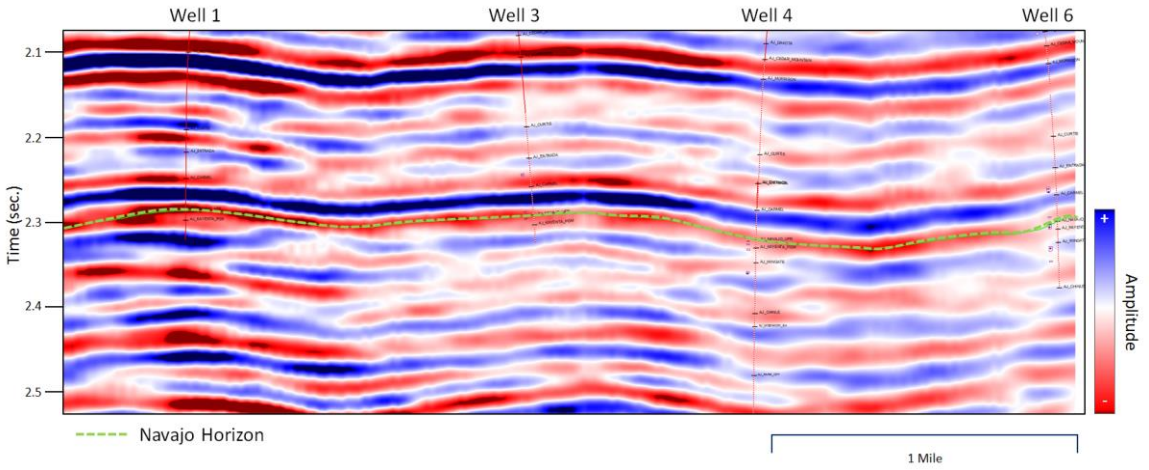

Figure 4.2.2 Arbitrary lines through four wells showing existing resolution issues. The Kayenta peak is completely unresolved throughout the entire cross section. All amplitudes are relative and thus unitless.

4.3 Frequency Domain Spectral Enhancement

To this point in the processing flow we have used spiking deconvolution as the main operator to compress the seismic wavelet and increase resolution. It is known that seismic wave propagation can be described as non-stationary; which means properties are time or spatially variant (Zhou, 2014). In seismic wave propagation, amplitudes decay over time differently at different frequencies causing the seismic wavelet to change with time. That is, amplitudes at

higher frequencies decay at a faster rate than amplitudes at lower frequencies as time or depth increases. This causes events later in time to have diminished high frequencies. In the study area, the Navajo sand interval is over 14,000 feet in depth (approximately 2.3 seconds) and only 30-90 feet thick. It also sits beneath massive sections of shale including the Mancos shale that is thousands of feet thick. All this considered, it is easy to see that once the seismic waves reach the Navajo the high frequencies have been significantly diminished. This loss in high frequencies combined with the thin nature of the Navajo results in the package dropping below seismic resolution and essentially being unresolved. At the top of the Navajo, the sharp impedance contrast between the hard Carmel shale and clean Navajo sandstone is large enough that the top reflection is still visible despite loss in high frequencies. However, at the base of the Navajo (Navajo to Kayenta) the impedance contrast is lower. High frequencies are needed to resolve this boundary. In order to boost the high frequencies, a spectral whitening operator was applied in the frequency domain. The ultimate goal is to produce an amplitude spectrum that is whiter and increases seismic resolution.

In the spectral whitening operation, a zero-phase frequency domain deconvolution was used to apply boosts at different frequencies and time gates to flatten the amplitude spectrum (Yilmaz, 1987). This is a method that can flatten the amplitude spectrum without disturbing the phase of the data. It works by taking an input trace with minimum-phase spiking deconvolution applied and transforming it into the frequency domain via the Fourier Transform over a specified number of temporal gates. Within each temporal gate, the spectrum is bandpass filtered over narrow frequency bands and the spectrum is then whitened or flattened. The whitened frequency bands are then summed together to give a whitened version of each temporal gate. Then the temporal gates are summed together and an inverse transform is

applied to give the resulting output trace that is the whitened version of the input trace. Figure 4.3.1 provides a simple flow chart of this process.

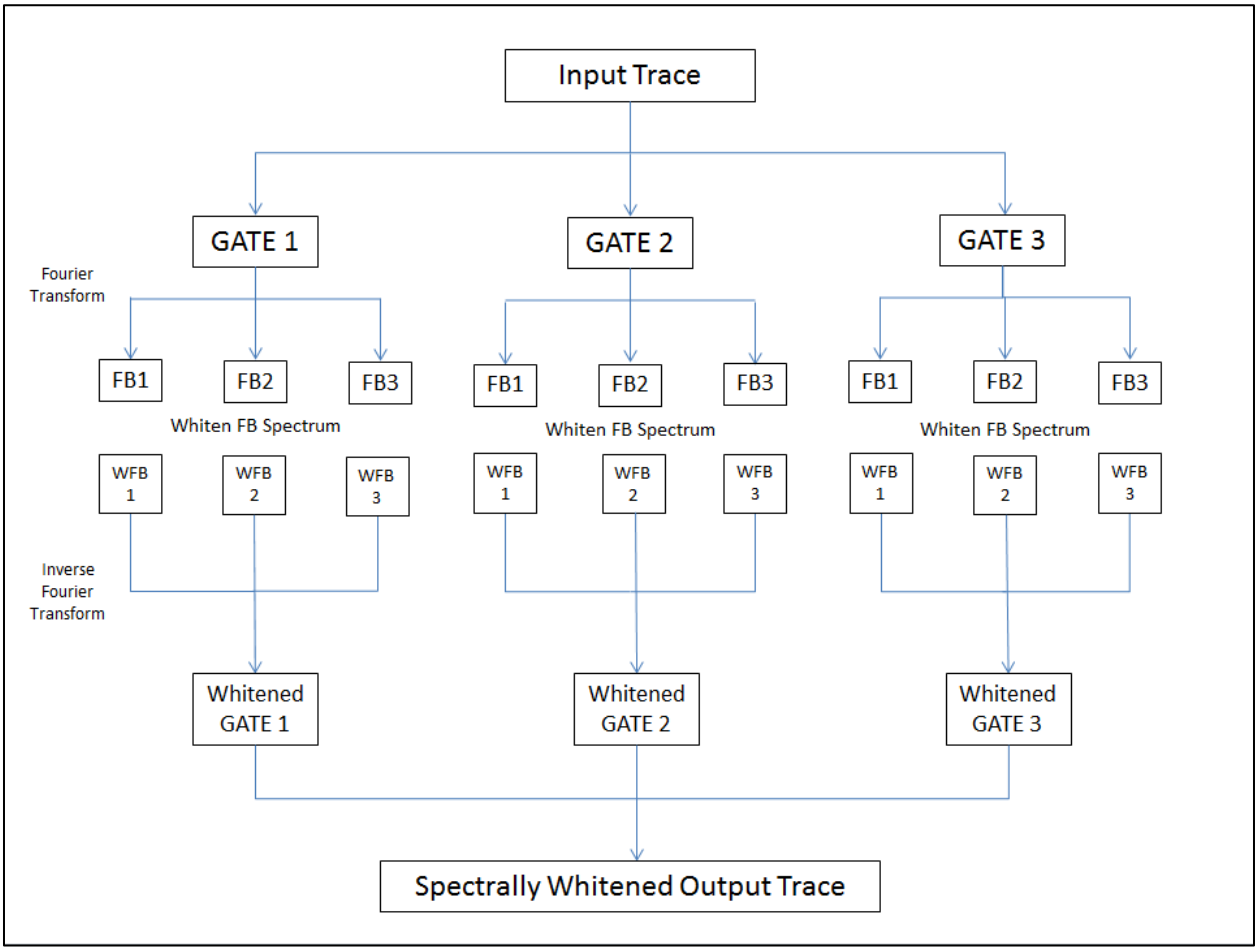

Figure 4.3.1 Flow chart showing how spectral whitening occurs from trace to trace. The result of this process is a broader bandwidth which results in a sharper wavelet with the end goal of providing better resolution to stacked data (image created in PowerPoint using Yilmaz, 1987 description of spectral whitening).

When this process is performed in the frequency domain over multiple time gates the resulting whitened trace is equivalent to applying a time-variant whitening operation (Yilmaz, 1987).

For Stone Cabin, the spectral whitening was applied to help compensate for the differing frequency content in the east compared to the west. Since it is known that the frequency content to the east is relatively poor due to acquisition restraints and a complex near

surface, the spectral whitening parameters were chosen to enhance the high frequencies in this area. Figure 4.3.2 shows a spectrum over the useful portion of a CDP gather (1000-3000 milliseconds) in the eastern portion of the survey.

The blue line laid over original spectrum (green) displays the desired spectrum after whitening. From 41-70 Hertz the frequency content is lacking. The low frequencies (5-11 Hz) and moderate frequencies could also use some boosting. Whitening parameters were chosen in a manner that will whiten the spectrum without introducing any frequencies that were not initially in the spectrum. The designed operator was run over five temporal gates where the amplitude spectrum in each gate is bandpassed into sixteen spectral bands from 8-65 Hertz. Each spectral band (8-11.5, 11.5-15,…,57.5-61, 61-64.5) was then whitened and multiplied together to give the whitened version of each temporal gate and summed to give the whitened trace.

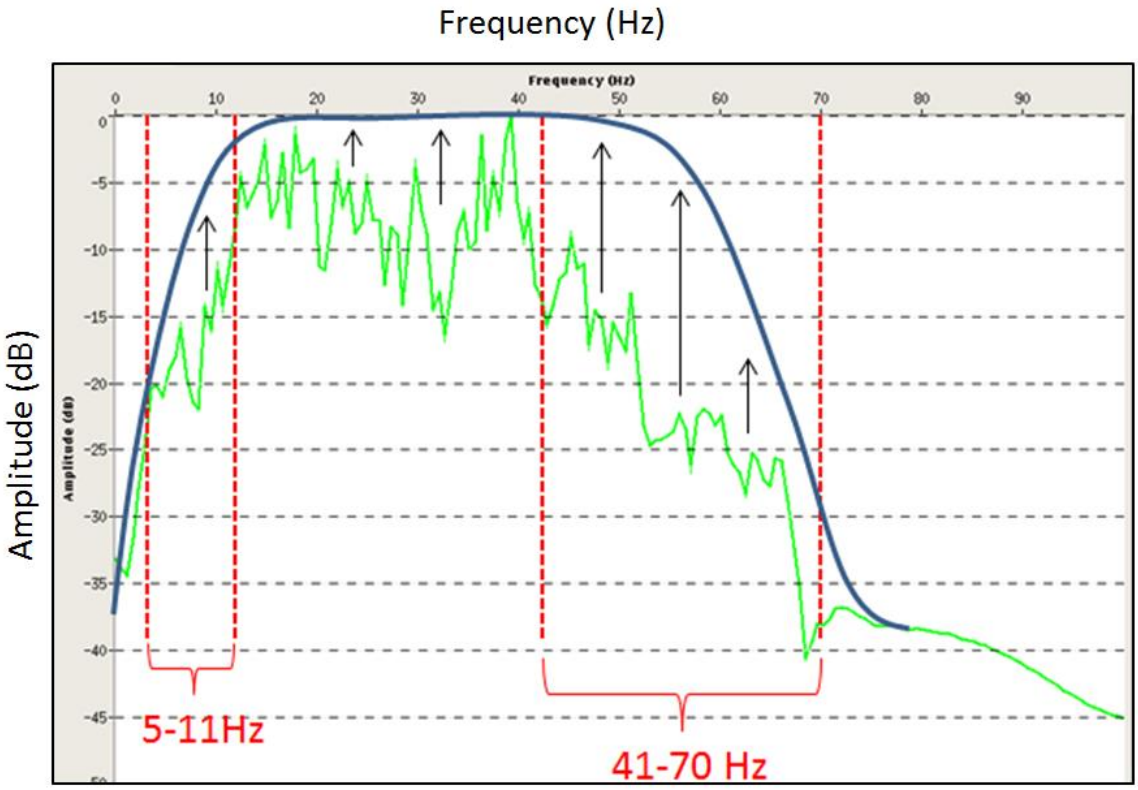

Figure 4.3.2 Current amplitude spectrum for 5-D interpolated, migrated, denoised and muted data. The blue outline represents a desired spectrum. To reach this goal the blocked frequencies in red will whitened and spectrally shaped to bump them up to our desired spectrum via the black arrows.

This process was conducted over every CDP gather and the amplitude spectrum for the entire CDP gather was then calculated post-whitening. It is important to note that spectral whitening, while useful, can boost high frequency noise. So, analysis of the resulting whitened spectrum a round of FX deconvolution is applied to rid the data of any lateral noise that the whitening may have boosted. Figure 4.3.3 shows the resulting amplitude spectrum post-whitening with FX deconvolution applied. Comparing the spectra before and after deconvolution (Figure 4.3.2 and 4.3.3), reveals a more desired shape has been achieved and the overall bandwidth between half amplitude points has greatly improved. Figure 4.3.3 shows that the low frequencies either didn't get boosted enough or the FX deconvolution knocked them back down a little. It is commonly misunderstood that high frequencies are the essential part of resolving thin beds. In

fact, resolution is more dependent on bandwidth as a broader bandwidth produces a spikier wavelet. Since seismic resolution is a function of bandwidth, we want to first recover the lower frequencies before examining the staked section for resolution. To recover these low frequencies, we apply a +9 dB increase centered around 10 Hertz in the frequency domain over a sliding window 200 milliseconds in temporal length. This spectral shaping will help recover the weakened low frequencies and provide a slightly broader bandwidth. A second round of FX deconvolution is applied after the low frequencies have been boosted. The resulting spectrum is shown in Figure 4.3.4. When comparing this spectrum to the whitened spectrum in Figure 4.3.3, it can be seen that the low frequency shaping produces a broader bandwidth which, in theory, will help resolve the Navajo sandstone. The CDP gathers to this point have been carried through 5-D interpolation, pre-stack migration, wavelet packet denoising, spectral whitening and low-frequency spectral shaping. All of these processes were carried out pre-stack with the hope that any residual noise would be attenuated once the data is stacked.

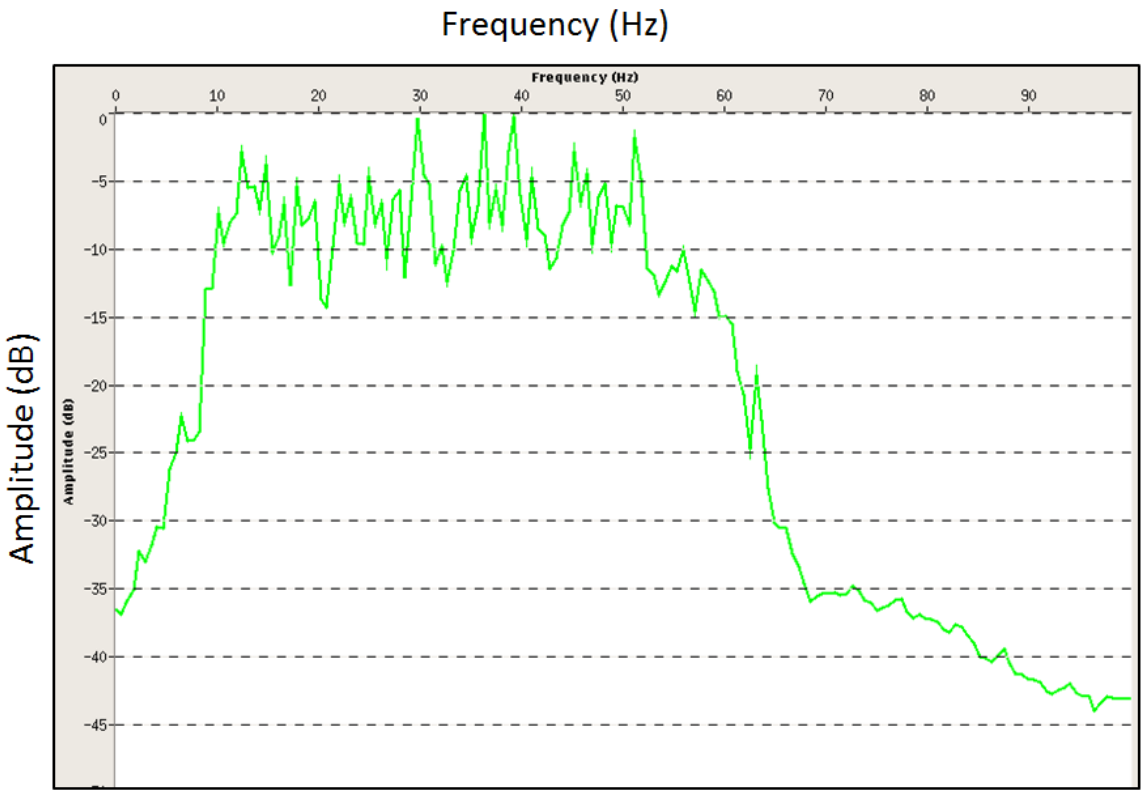

Figure 4.3.3 Amplitude spectrum post-whitening and low frequency shaping. Increasing the bandwidth of the data will provide better frequency resolution to our output stacks.

4.4 Spectral Enhancement Analysis

To evaluate whether spectral enhancement has improved resolution, the spectrally enhanced stack is compared to the type log synthetic seismogram. First, the statistical wavelet was re-extracted around the well. The wavelet extraction from the spectrally enhanced stack is more desirable for interpretive purposes (Figure 4.4.1).

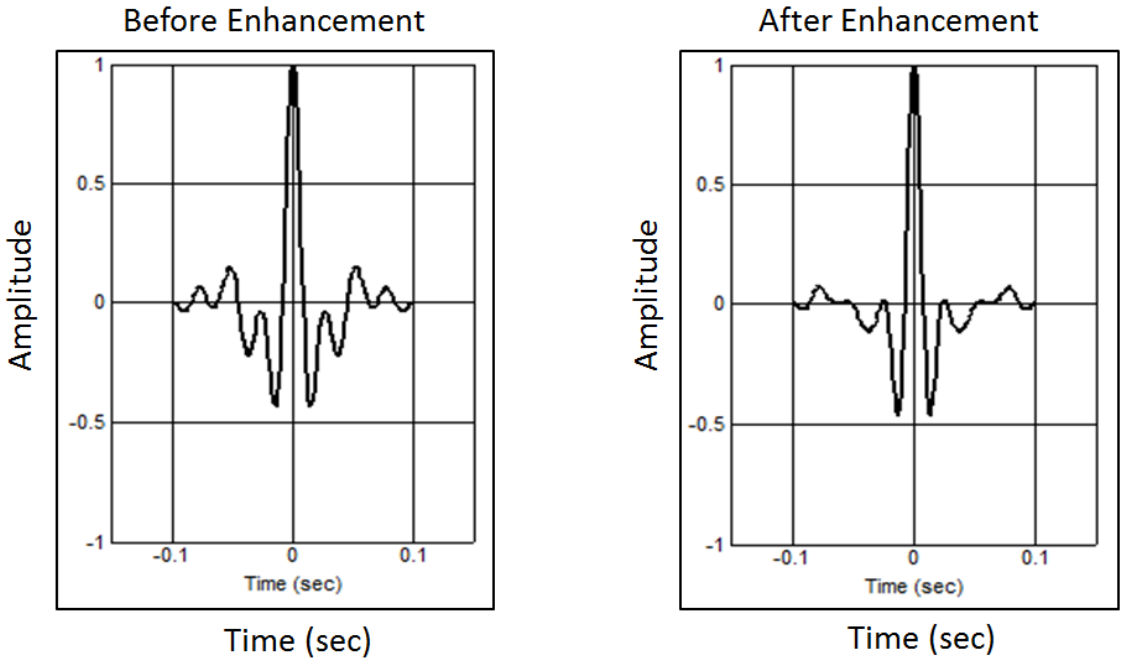

Figure 4.4.1 Comparison of the wavelets from the Type Log over a 1-3 second window with a 500 foot radius around the borehole. The wavelet pre-frequency enhancement (left) is broader and has greater side lobe energy. The wavelet post-frequency enhancement is spikier and the side lobes are knocked down.

The wavelet from the spectrally enhanced data is generally spikier and the side lobes have been compressed. This is a direct result of the spectrally enhanced data having broader bandwidth than the original data. Using extracted traces from the spectrally enhanced stack a new synthetic tie was generated (Figure 4.4.2).

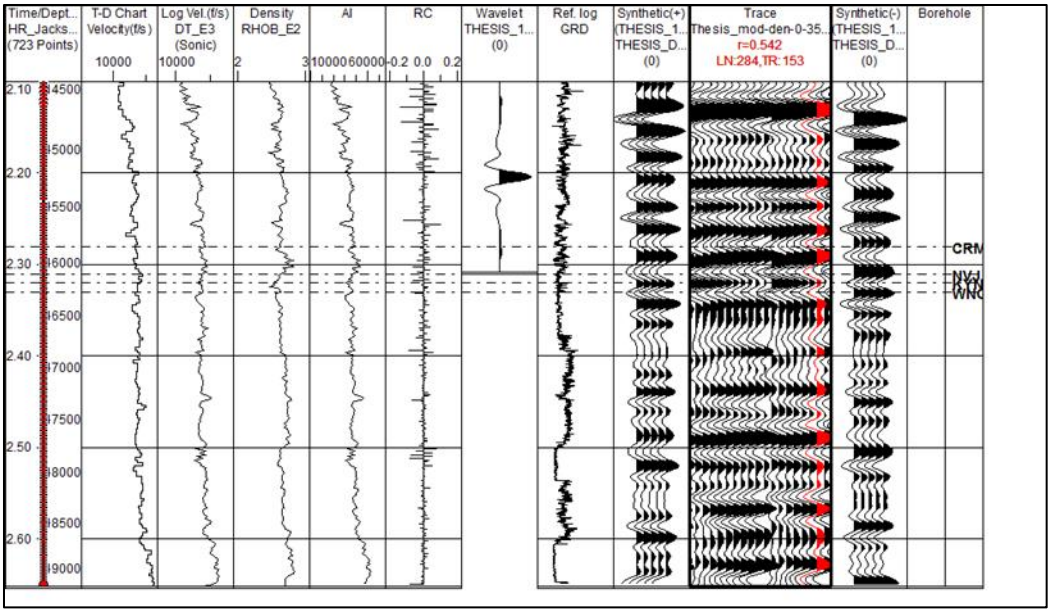

Figure 4.4.2 Synthetic well tie post-frequency enhancement. The Kayenta (KYNT) peak is now visible (resolved) across the full trace length. This is a result of the increased bandwidth. All amplitudes are relative and thus unitless.

The correlation coefficient has dropped slightly from 0.580 to 0.542. In boosting the high frequencies, the amount of high frequency noise has also been boosted, thereby reducing the correlation coefficient. However, though the correlation coefficient has been reduced overall, the correlation has actually increased in the zone of interest. This is a common trade off in seismic data processing. It is more important for bandwidth to increase even if that means boosting a small amount of noise in respect to resolving thin beds. If the correlation window is limited to only the zone of interest (Figure 4.4.3) the correlation coefficient slightly increases and the peak at the Navajo-Kayenta transition is sharper. This indicates better resolution for the purpose of this study from the spectrally enhanced stack.

When an arbitrary line (Figure 4.4.3) from the spectrally enhanced stack is taken through multiple wells and extended to the far east portion of the survey, the amplitudes diminish a significant amount to the east. For this reason, a large window AGC (2.5 seconds) was

applied trace-by-trace to stabilize amplitudes across the entire survey and facilitate mapping.. This will help the fault mapping comparison between the spectrally enhanced version of the data and the original denoised with 0-35 angle stacks version of the data.

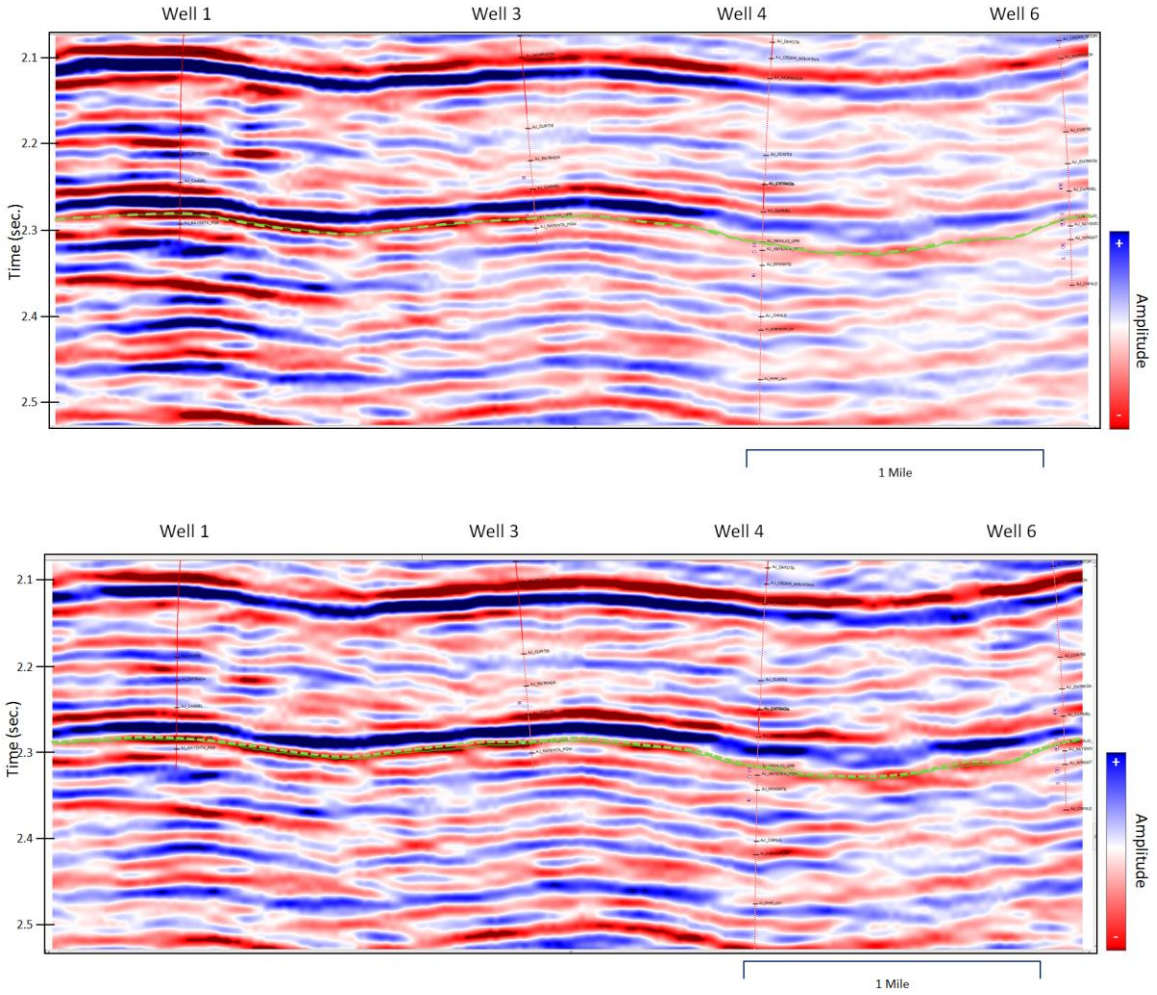

Figure 4.4.3 Comparison of stacked data through well control after frequency enhancement (top) and after applying a 2.5 second automatic gain control. Amplitudes now are more balanced resulting in events being easier to track. All amplitudes are relative and thus unitless.

Chapter 5: Structural and Stratigraphic Mapping of Navajo Sandstone

5.1: Comparison of Processed Versions

Figure 5.1.1 compares the results from the (a) 5D interpolated pre-stack migrated, (b) moderately denoised, (c) angle stack from 0-35 degrees, (d) spectrally enhanced (whitened and shaped) and lastly (e) enhanced with 2.5 second AGC.

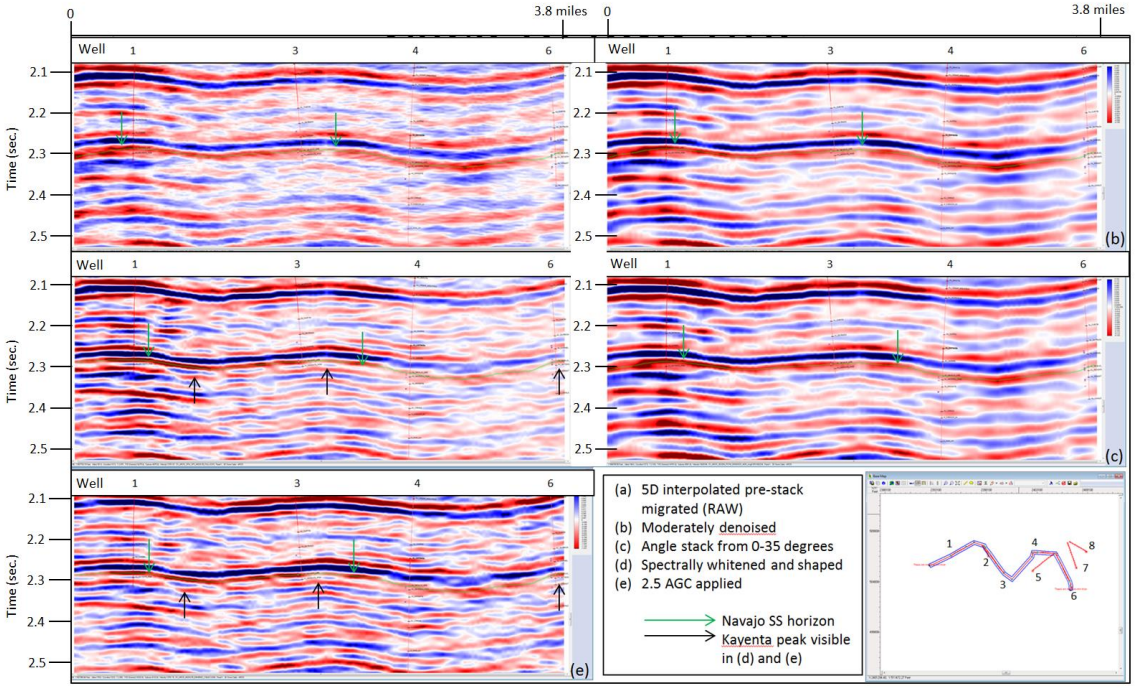

Figure 5.1.1 Comparison of stacked data throughout the processing sequence. (a) 5D interpolated and pre-stack migrated, (b) moderately denoisied, (c) angle muted 0-35 degrees, (d) Spectrally whitened and shaped and (e) 2.5 AGC applied. Each step is the result of the combination of previous steps. All amplitudes are relative and thus unitless.

On the 5D interpolated stack at Well 2, the Navajo is well resolved and the Kayenta peak below is present. Moving away from Well 2 toward Well 3, resolution is lost and the Navajo-Wingate begins to interfere into one trough. At Well 3 the Kayenta is completely unresolved and the Navajo-Wingate is combined into one reflection. Overall there is still high frequency noise in the section which causes the Navajo to degrade in lateral continuity. When applying the wavelet packet moderate denoising in (Figure 5.1.1b) a great portion of the noise has been removed and

the Navajo reflector increases in lateral continuity, but the Kayenta is still below resolution. The 0-35 degree angle stack (Figure 5.1.1c) has very little visible changes in the zone of interest but, it has helped boost some amplitudes around Well 3 slightly. The largest improvement to the zone of interest occurred when the spectrum was whitened and shaped in low frequencies (Figure 5.1.1d). This dramatically improved the resolution of the Kayenta. By slightly extending the spectrum, the base of the Navajo was resolved for a good portion of the section. The Kayenta is present until Well 3 where the coarsely acquired data and large canyons have caused the frequency content to degrade rapidly. In addition, these canyons and proximity to the edge of the survey have caused a drop in fold. Some may want to interpret this as a truncation of the Kayenta, but due to the issues previously discussed in this area there isn't sufficient data to resolve the base of the Navajo. If an arbitrary line is drawn down dip through Well 3 in Figure 5.1.2 the Kayenta is still present on both sides of the well where data quality is a slightly improved.

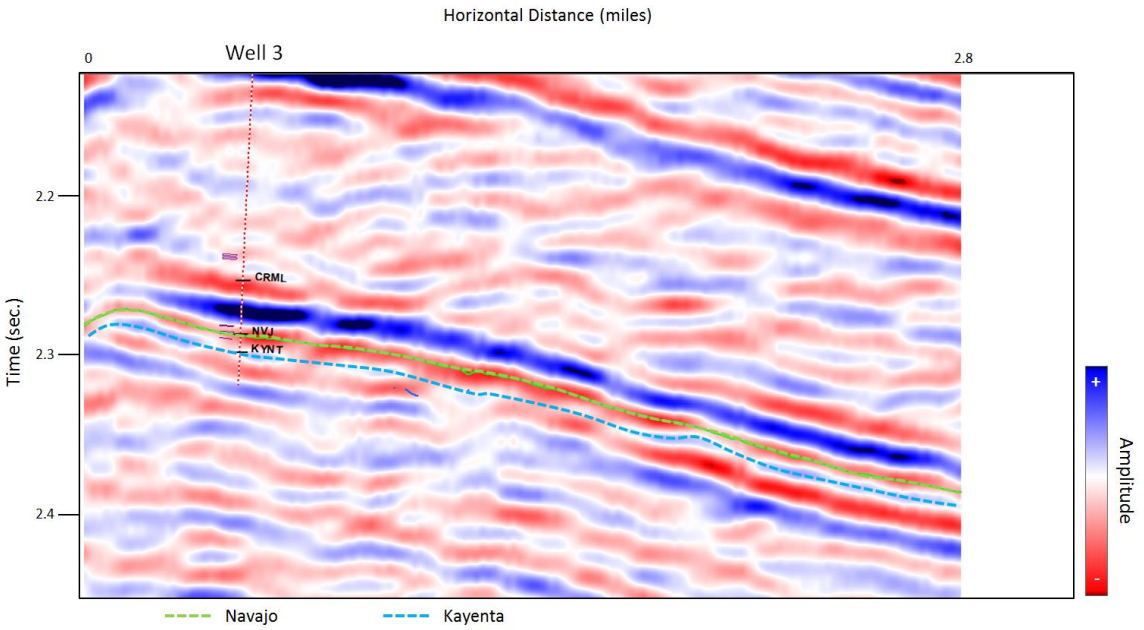

Figure 5.1.2 Arbitrary line through Well 3. The Kayenta peak is clearly visible on both sides of the well throughout the entire line. All amplitudes are relative and thus unitless.

Returning to Figure 5.1.1, when a 2.5 second AGC is applied, the amplitudes are balanced laterally which helps in mapping the Navajo horizon in poor data quality areas. The processing sequence applied eliminated a great portion of the noise resulting in a higher SNR, improved overall lateral continuity of the Navajo sandstone and resolution of the base of the Navajo in a portion of the data where frequency content and fold were sufficient.

Seismic Bandwidth Extension

To further test how well frequency enhancement was able to resolve the base of the Navajo sandstone, bandwidth extension via a sparse-layer reflectivity inversion was applied (Zhang and Castagna, 2011). The technique assumes the same convolutional model previously discussed and that the wavelet is known. Using basis pursuit decomposition (Liang et al., 2014) the seismic trace is decomposed with a wavelet dictionary of odd and even reflectivity patterns (Zhang and Castagna, 2011). The reflectivity pairs are then scaled, shifted and summed together to produce the hi-resolution seismic traces. The resulting traces have broader bandwidths and

contain frequencies that are not in the original bandwidth. For more information refer to Zhang and Castagna (2011) and Liang (2014). For this study, a 10 square-mile area around the Peter's Point gas field was cut out where the data tends to be relatively stable and there is enough well control for the technique.

To keep things consistent between the comparisons the same data that was used as input to our spectral enhancement was input to the bandwidth extension technique. We then allowed the algorithm to push the bandwidth as high as half the Nyquist frequency (125 Hertz) to bring in frequencies that are well outside the original seismic bandwidth. Figure 5.1.3 shows a well to well cross section of the bandwidth extended results.

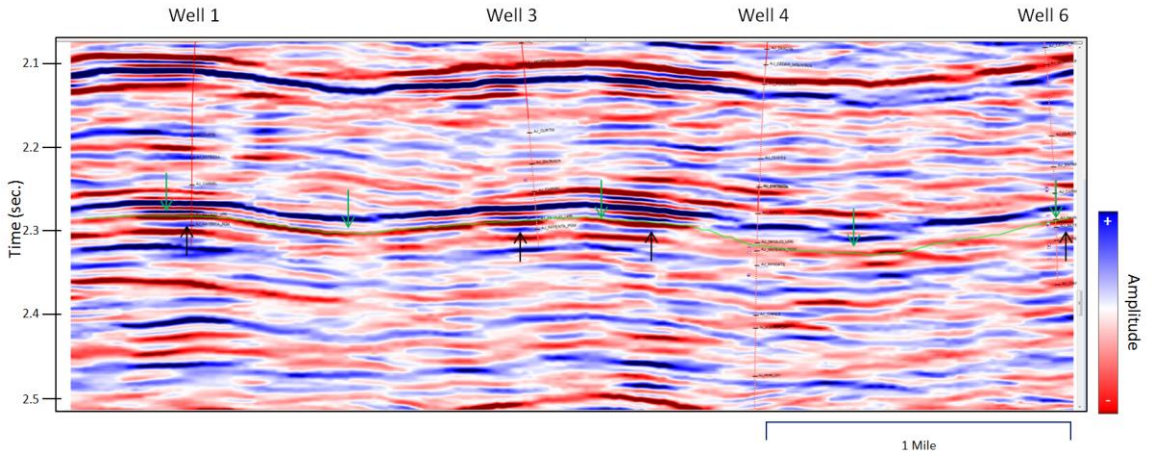

Figure 5.1.3 Results of the sparse spike bandwidth extension. The green arrows point to the Navajo trough and the Black arrows point to the Kayenta peak. The Kayenta trough has improved in resolution when compared to previous attempts. All amplitudes are relative and thus unitless.

The technique resolved the base of the Navajo (top of Kayenta). To compare these results to The prior spectral enhancement more closely, the bandwidth extended volume was bandpassed back to the spectrum of the spectrally enhanced volume (Figure 5.1.4).

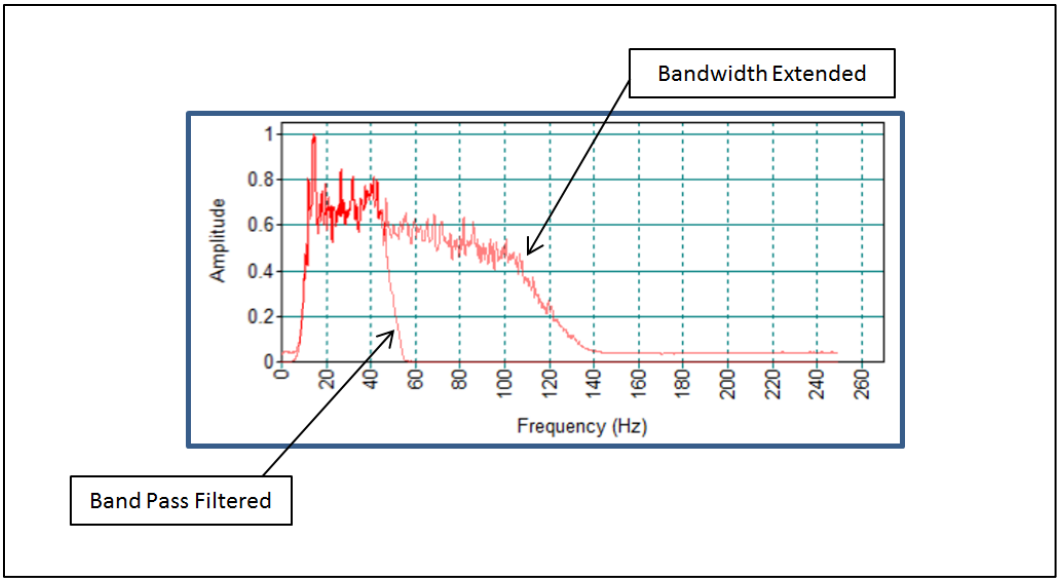

Figure 5.1.4 Comparison of the spectra after bandwidth extension and with a band-pass filtered applied from 5/10 (low pass/high cut) and 45/55 (high cut/ low pass). A filter was applied in an attempt to reduce the high frequency noise boosted when pushing the frequencies to well outside the data range.

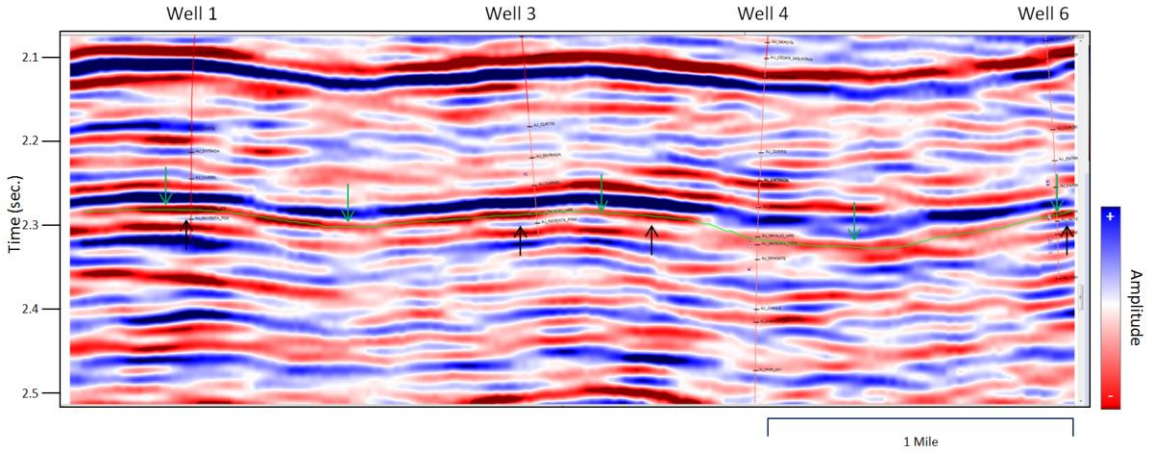

Figure 5.1.5 Result of bandwidth extended with the band pass filtered applied along the same arbitrary line in Fig. 5.1.3. The Kayenta peak is still well resolved while some of the high frequency noise has been removed. All amplitudes are relative and thus unitless.

The low-pass filtered bandwidth extended result is shown in Figure 5.1.5. Even with a band limited version of the bandwidth extended data the base of the Navajo is still well resolved to a large degree. It is quite evident that the bandwidth extended and filtered version exhibits some improvement over the spectrally enhanced volume in terms of resolution and continuity, in that

within the band of the original data it can boost high frequency signal more than noise at those frequencies. When comparing Figure 5.1.5 to Figure 5.1.1a, we notice the results look similar but the filtered bandwidth extension still provides a better solution for Navajo resolution. This is because spectrally whitening and spectrally shaping only allows you to work within the original spectrum to retrieve stable results. While the spectrum of the two may look almost identical, the spectral shape of the bandwidth extended volume is different which allows for better resolution. To conclude this comparison, it is evident that bandwidth extension provides much better results than just spectral enhancement. It is recommended that processors seek this solution over a simple spectral enhancement. However, a spectrally enhanced solution is a viable option for those who do not have access to bandwidth extension.

5.2: Seismic Attributes for Structural and Stratigraphic Mapping

Seismic attributes have been used for many decades as tools to map subsurface geology, aid in reservoir characterization, and as indicators for hydrocarbon accumulation. A seismic attribute can be defined as any measurable characteristic of a seismic trace and provides interpreters a view into seismic data from multiple perspectives. Commonly, attributes can be broken into time, amplitude, frequency, attenuation or a hybrid of these types. Our focus will be primarily on attributes that aid in fault mapping and thin bed analysis of the Navajo sandstone. Since Enervest Operating Co. currently holds leases in the Stone Cabin 3D, all attributes will be restricted to the 10-square-mile cutout where well control exists. In addition, the bandwidth extended (filtered) volume will be used for all attribute analysis as it returned the best result and seems to be the most stable.

The first two useful attributes extracted were simple time and amplitude values along the Navajo horizon. Displayed in Figure 5.2.1 is a time extraction with contours along the Navajo horizon (full data). This is useful in obtaining an overall sense of the broad structure where the warmer colors represent structural highs and cooler colors structural lows. We can see on this time structure map a favorable structure for hydrocarbon accumulation where the blue line represents a trap against the regional thrust fault.

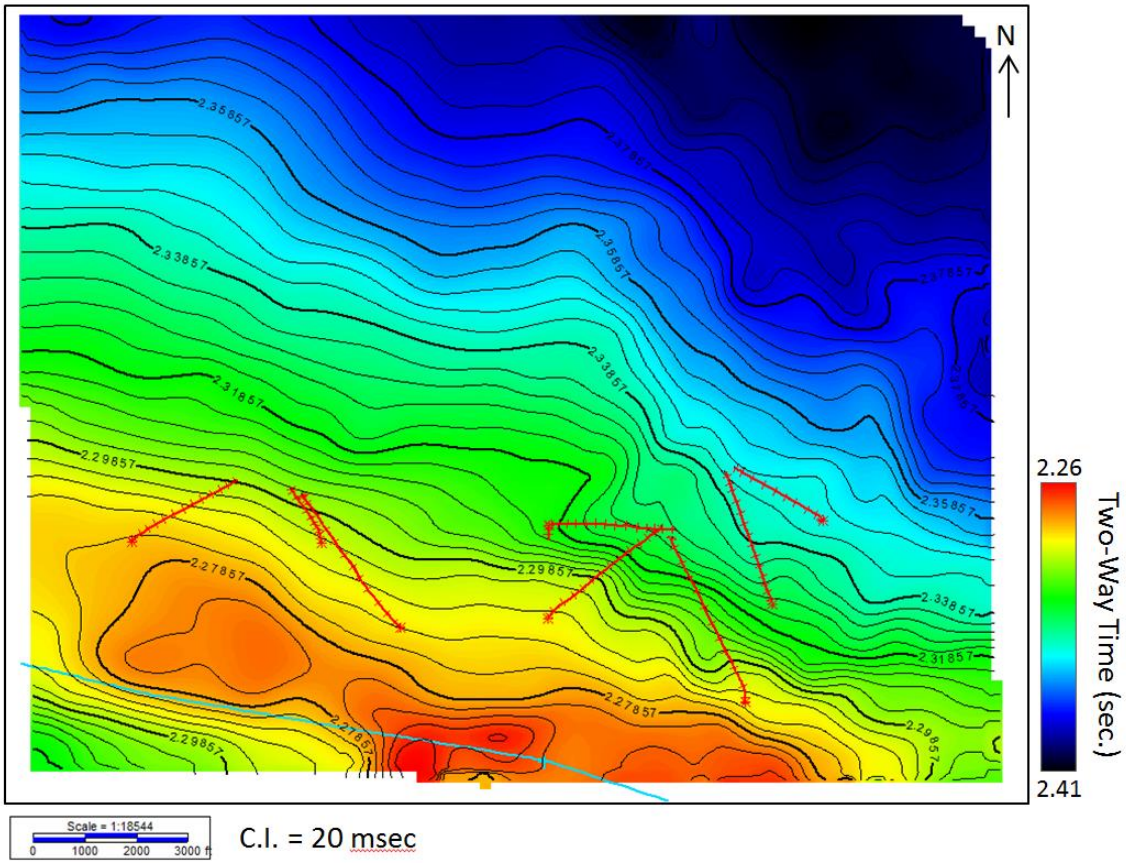

Figure 5.2.1 Time Structure map extracted on Navajo horizon over the Peter's Point anticline/gas field. Warmer colors represent structural highs and cooler structural lows. The light blue line at the bottom shows the position of the regional thrust fault that acts as a hydrocarbon trap.

Switching to the bandwidth extended volume, amplitudes were extracted along the Navajo horizon displayed in Figure 5.2.2. Typically, amplitude extractions are more useful in areas such as the Gulf of Mexico where high porosity thick sands filled with gas exhibit

amplitude “bright spots” that can be interpreted as direct hydrocarbon indicators (DHI). For the Navajo, the sand is buried very deep, is stratigraphically thin and has limited porosity. Therefore, the bright amplitudes in the display are not a director indicator of hydrocarbons. It is known that the Navajos seismic response returns a trough (negative amplitudes). The black arrow in Figure 5.2.2 points out a strip that has anomalously high positive amplitudes and may indicate the presence of a fault. We investigate this further using an attribute called coherence (energy ratio similarity).

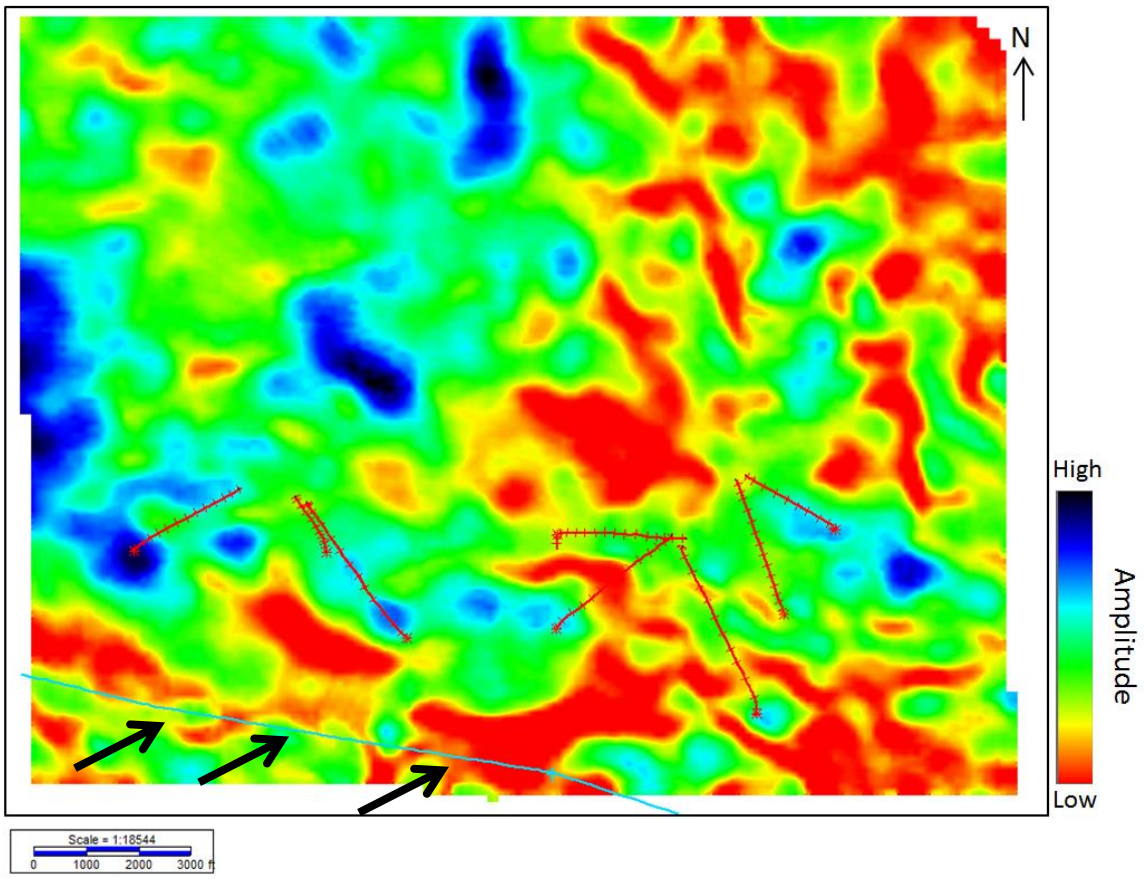

Figure 5.2.2 Amplitude extraction on the Navajo horizon. Warmer colors represent high amplitudes and cooler represent low amplitudes. The black line points to the NE-SW striking thrust fault. All amplitudes are relative and thus unitless.

Coherence (Energy Ratio Similarity)

When extracted along a horizon slice, coherence will highlight changes in seismic waveforms that can then be expressed as changes in structure or stratigraphy. We will avoid using time slices as they can be misleading when in present of structural dip where a single time slice can cross multiple horizons. This can inaccurately display anomalies as changes in structure and stratigraphy. For the coherence calculation we used an algorithm developed by Dr. Kurt Marfurt and his team at The University of Oklahoma. This coherence algorithm is called energy ratio similarity (ERS) and is available in the AASPI attribute software package. ERS uses dip calculations in the inline and crossline directions to use as an input to the coherence calculation. Figure 5.2.3 from Marfurt (2006) is an illustration defining these two calculations where Θ_x and Θ_y are the apparent dips of a reflector in the inline (x-direction) and crossline (y-direction).

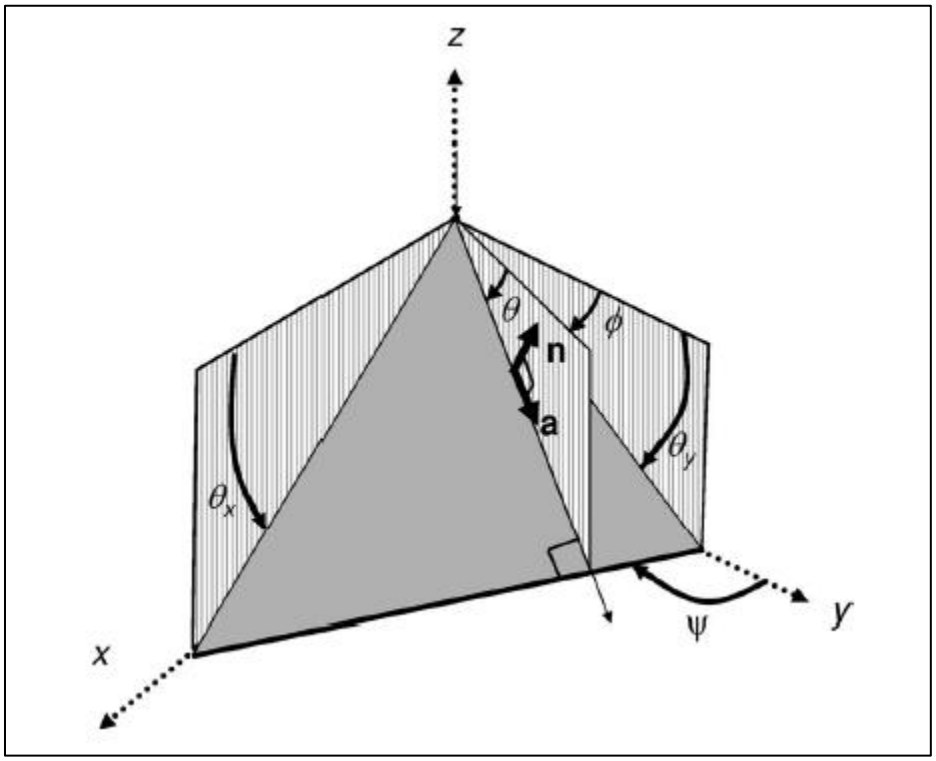

Figure 5.2.3 Representation of inline and crossline dip used for calculating energy ratio similarity (coherence) from Marfurt, 2006.

Using these apparent dips, apparent time dips can be calculated using equations 5.1 and 5.2 (Marfurt, 2006).

$$p = \frac{2tan\theta_x}{v} \qquad (5.1)$$

$$q = \frac{2tan\theta_y}{v} \qquad (5.2)$$

Where *p* and *q* are the respective apparent time dips in the inline and crossline direction and the velocity (v) is constant. The dip calculation then scans the data in the inline and crossline direction in angle increments to find the maximum semblance along a reflector (surface) shown in Figure 5.2.4 from Marfurt (2006).

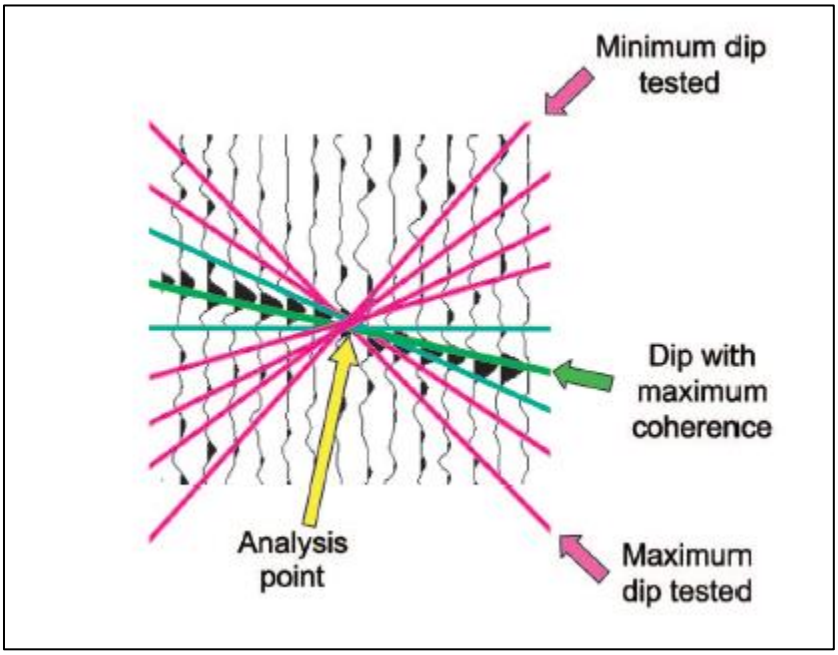

Figure 5.2.4 Depiction of maximum and minimum dip calculations for inline and crossline dip. The pink lines represent all dip searched windows while the green show the dip along maximum coherence. From Marfurt, 2006.

It then writes these volumes out to a file that is used in the coherence calculation along with the seismic amplitude volume. Using these three files, ERS uses an eigenstructure-based calculation to compare the energy of an analysis point to that of the neighboring traces. Simply, it scans the

volumes using the dip calculations as a sort of guide. At each analysis point it calculates the energy of the input traces in an analysis window then calculates a waveform that best represents the waveform of each trace and replaces the initial trace with the calculated trace. By comparing the calculated waveforms to the original waveforms, the algorithm assigns a value between 0-1 where 1 represents maximum semblance (or coherence). A schematic representation of this can be seen in Figure 5.2.5 taken from Marfurt (2006).

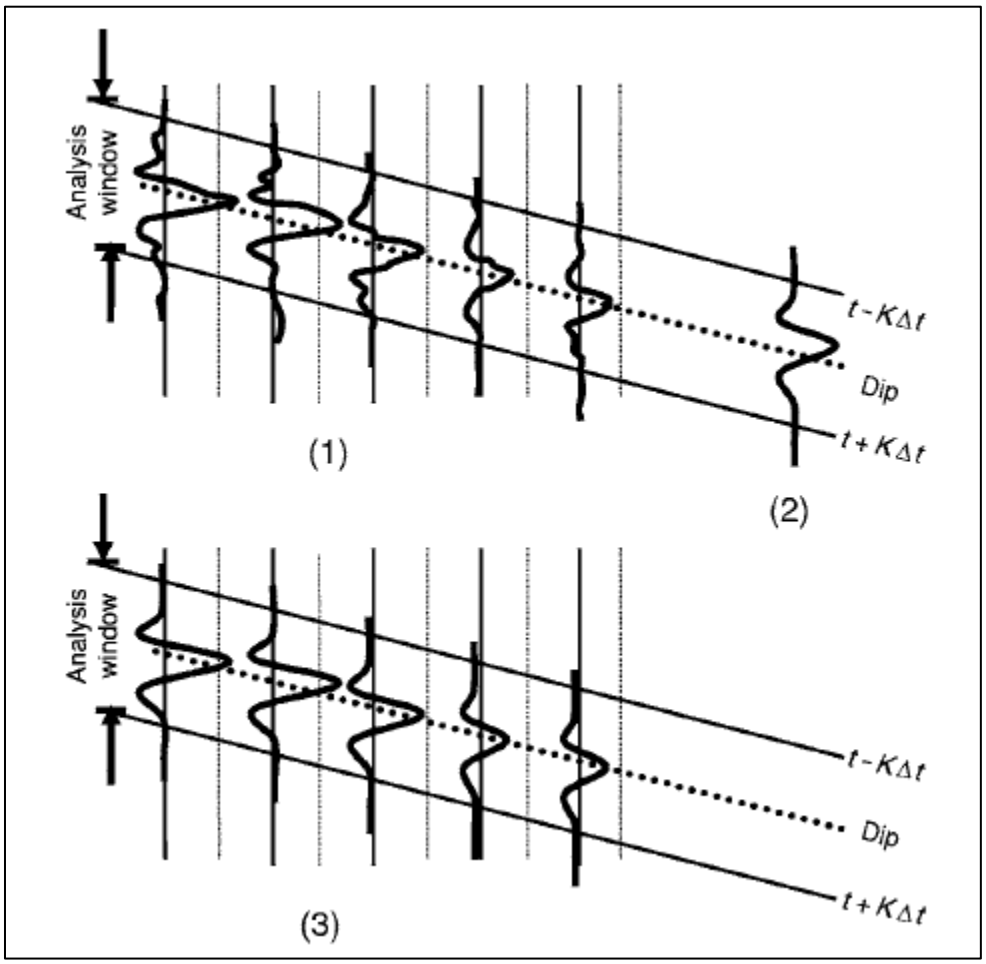

Figure 5.2.5 Example of coherence calculation from Marfurt, 2006. (1) The original traces are compared with (2) a model trace. (2) is used to create a model of the original data where each trace is compared to neighboring traces based on how similar they are. Each trace is assigned a value from 0-1 where 0 means they are dissimilar and 1 means they are the same.

For fault mapping the bandwidth extended (filtered back) data were used. In the dip calculation, parameters were set to allow a 5-degree search scanning every 1-degree. A window of 64 milliseconds was used as a temporal scan. The inline and crossline dip calculated volumes were then input into the energy ratio similarity calculation which allowed for a 10-millisecond half window for temporal scanning. The results of the ERS calculation are displayed along the Navajo horizon in Figure 5.2.6. In this image, faults (or anomalies) are highlighted in black where traces are dissimilar to one another (value less than 1). Areas in white represent where traces are very similar (value equal or close to 1).

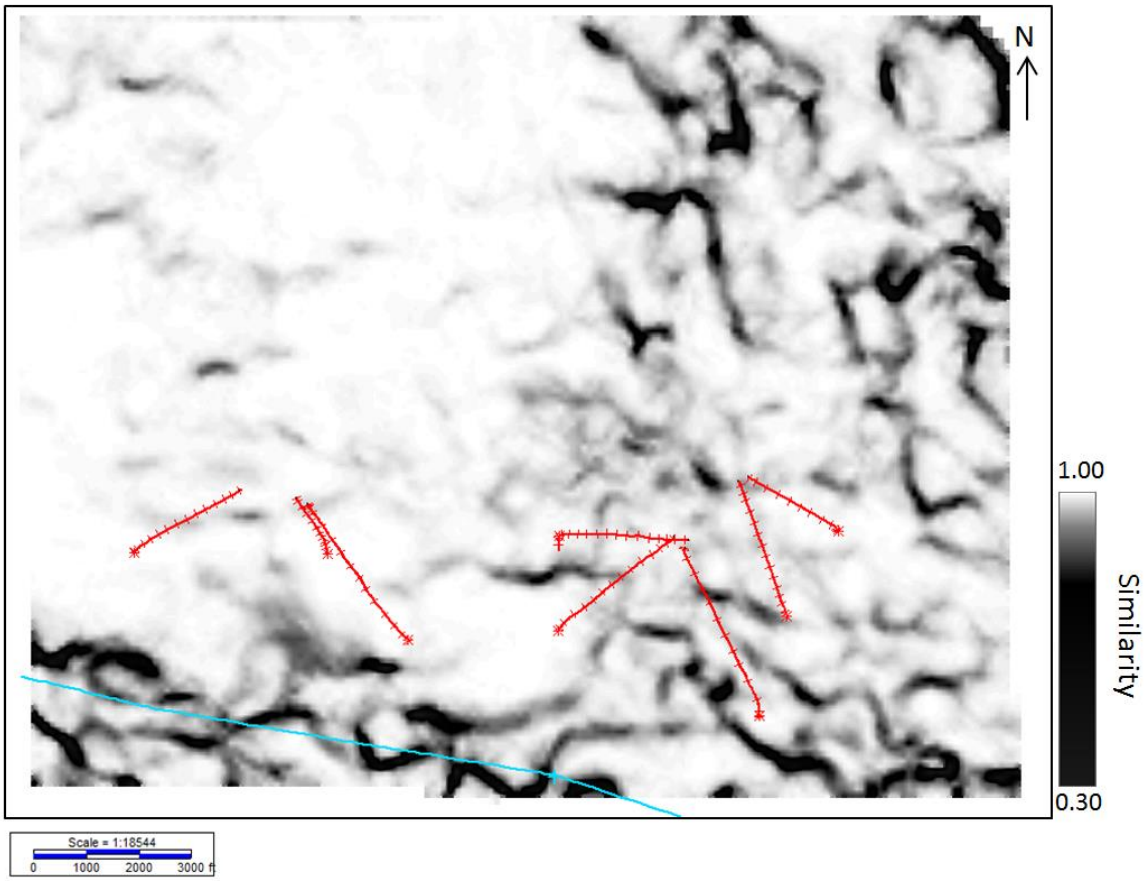

Figure 5.2.6 Energy ratio similarity extraction on the Navajo horizon. Black lines represent where possible faults or horizon truncations may occur. White space represents sand continuity.

An arbitrary line (Figure 5.2.7a) through the black anomalies show structural (faults) or stratigraphic (truncations) of the Navajo interval. The blue line on both the horizon slice and vertical section represent the thrust fault where the upthrown side is to the north and downthrown to the south. The fault can be tracked from the Mississippian basement up to the massive Mancos shale. This thrust fault is important for the Navajo as it acts as a structural trap for natural gas accumulation. Stepping to the east (Figure 5.2.7b) is another set of minor faults highlighted by the orange arrows which can be tracked from the Wingate to the Carmel shale. Moving further down dip to the edge of the survey are more anomalous signatures that could be mistaken as faulting or changes in stratigraphy. These false anomalies (red arrows) are the results of poor data quality due to acquisition restraints. The boost in higher frequencies caused areas to have some lateral noise that can be misleading. This is a common issue in coherence displays where data is noisy. To confirm real faults from noise other seismic attributes are used later in this chapter. The true faults should then be present in multiple attribute displays.

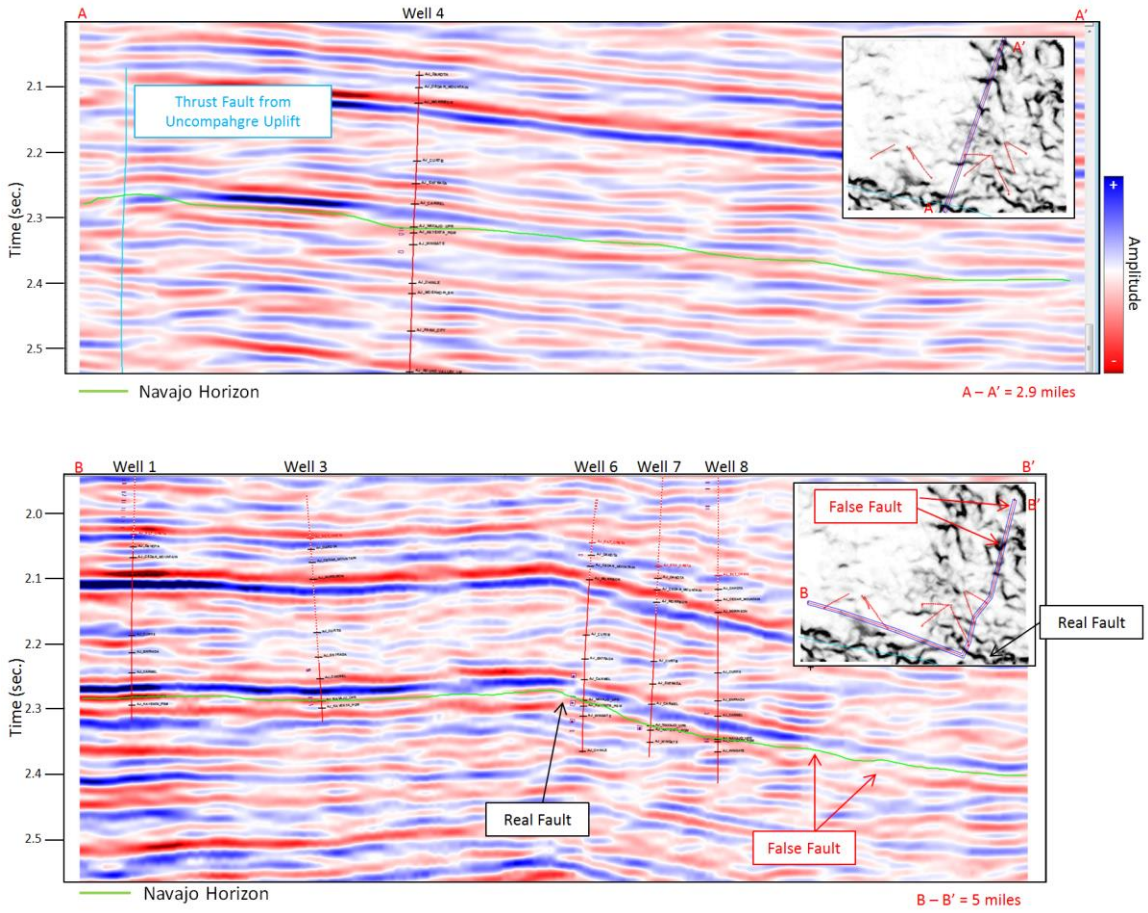

Figure 5.2.7 Top figure shows an arbitrary line through the ERS extraction. Highlighted in blue is the thrust fault that was created from the Uncompaghre uplift. Bottom image represents areas where true faults exist (black box) and areas where false faults due to data stability exist (red box). The green line shows the Navajo horizon pick. All amplitudes are relative and thus unitless.

Spectral Decomposition (Complex Matching Pursuit)

It is known from the well logs that the Navajo sand varies in thickness from well-to-well ranging from 30-90 feet. Using the complex matching pursuit (CMP) spectral decomposition algorithm in the AASPI attribute software iso-frequencies on a single inline through two wells are analyzed. The technique used was developed by Liu and Marfurt (2005) in the AASPI attribute calculator. Using a Ricker wavelet, CMP computes a complex wavelet dictionary for a sampled suite of frequencies (Chopra and Marfurt, 2007). Using a Hilbert transform a complex

trace is generated and the instantaneous envelope and frequency is calculated for each trace (Chopra and Marfurt, 2007). The algorithm then searches for the largest values of the envelope and the corresponding instantaneous frequency (Chopra and Marfurt, 2007). Then it fits the suite of wavelets to the complex trace in a least squares sense and solves for complex coefficients that corresponds to the amplitude and phase of the complex wavelet (Chopra and Marfurt, 2007). By subtracting the amplitude and phase-rotated complex wavelet from the original trace to compute a residual trace. This process is then carried out until the residual falls below a threshold (Chopra and Marfurt, 2007). For this evaluation, we are looking for single frequencies that have the largest spectral magnitude at the known well-locations and use these single frequencies to map the stratigraphic variability in the Navajo.

It can be difficult to analyze spectral decomposition outputs without first having an underlying model. For this reason, we start our analysis by taking the Type Log and simulating the variable thickness of the Navajo sandstone in a wedge model. At the center of the model, the interval thickness is equal to 20 feet, and at the edges is 150 feet. The Kayenta thickness constant throughout the entire model. A constant velocity was placed above the Navajo using the Carmel shale average sonic slowness where the inverse is equal to the velocity. The same was performed below the Kayenta using the Wingate's average sonic slowness. By doing this, only the Navajo-Kayenta impedances are used in the calculation of the synthetic traces, thereby isolating just the local response of these layers. Taking a wavelet extracted from the same well-logs previously used the synthetic wedge model was created (Figure 5.2.8). The wavelet used for the model is pictured in the top left corner of this figure.

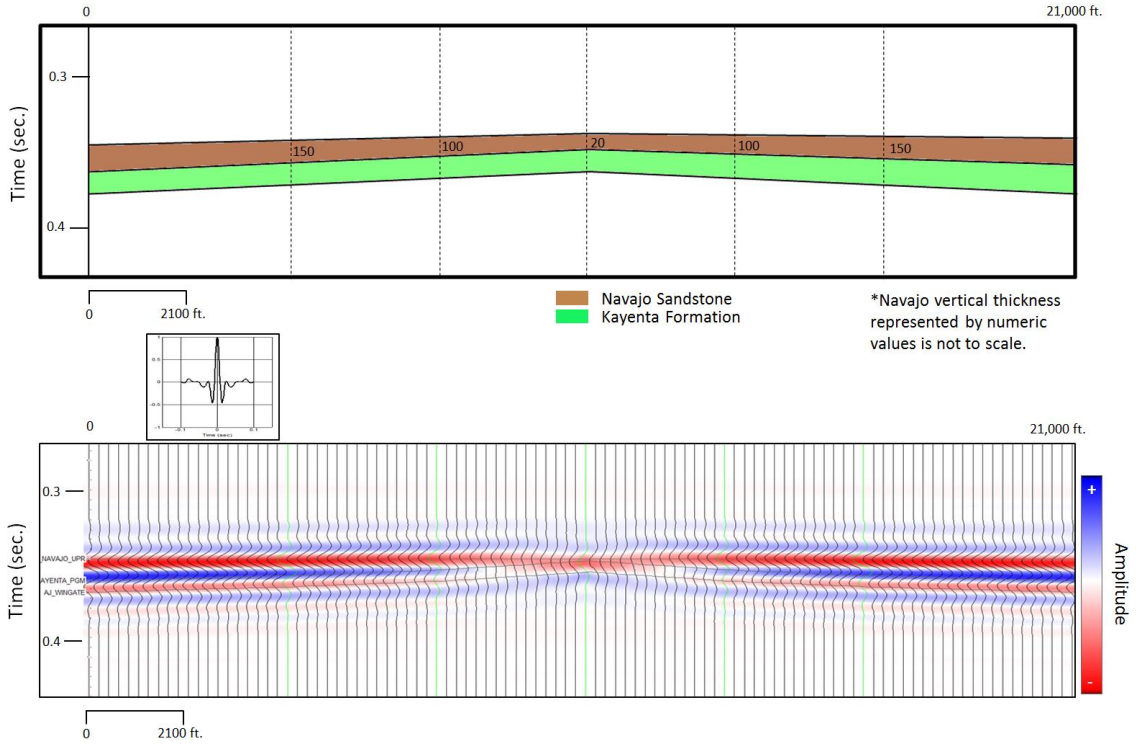

Figure 5.2.8 Synthetic model created by stretching Well 4 thickness at the Navajo to 150, 100, 20, 100, 150 feet. The Kayenta was kept at constant thickness. A wavelet was extracted from the bandpass filtered/bandwidth extended data and convolved with the impedance profile. The layer above the Navajo was kept at constant velocity matching the Carmel shale log velocity. The same was done for the layer Below the Wingate below the Kayenta formation. All amplitudes are relative and thus unitless.

This synthetic thin wedge model was then run through the complex matching pursuit spectral decomposition using a Ricker wavelet tabled from 2-120 Hertz incrementing by a half-frequency. The output was the filtered to a bandwidth of 5-10-45-55 Hertz. Each iso-frequency from 5-55 Hertz was output. The results of this analysis are shown in Figure 5.2.9. At the center of Figure 5.2.9a where the Navajo is the thinnest there is a peak magnitude at around 15 Hertz. It is obvious that at this thickness there is tuning with the base of the Kayenta formation instead of the base of the Navajo (due to the thin Navajo package). Stepping up to 30 Hertz (Figure 5.2.9b) the peak magnitude at 20 feet thickness starts to diminish and brighten at 100 feet. Moving

even higher to 45 Hertz (Figure 5.2.9c) the peak magnitude is practically zero at 20 feet thickness and still giving a response at approximately 75 feet.

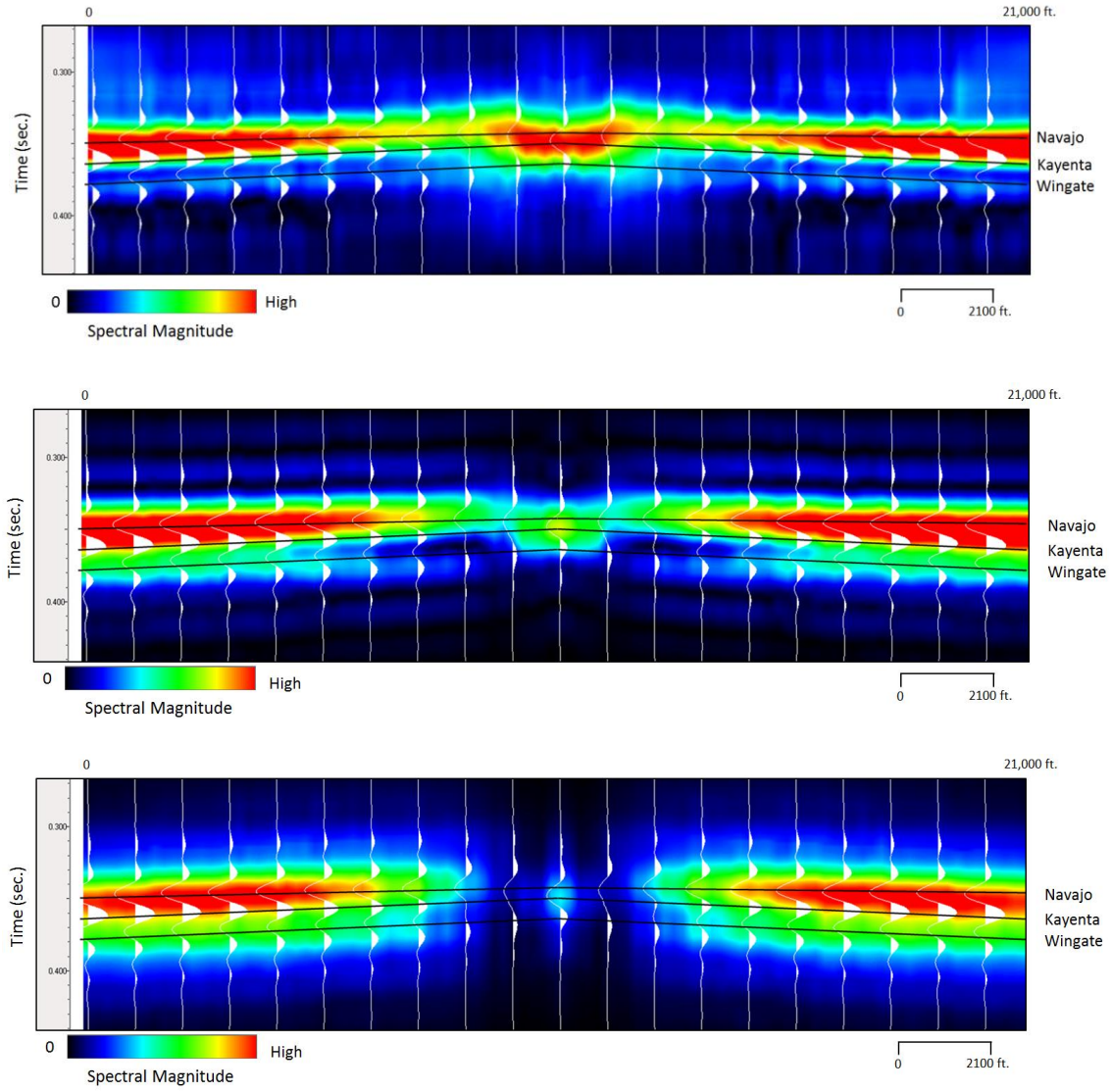

Figure 5.2.9 Iso-frequency response from synthetic wedge model at (a) 15 Hz (b) 30 Hz and (c) 45 Hz. At 20 feet Navajo thickness, the peak magnitude response is greatly diminished at 45 Hz.

Based on the synthetic model, the expectation is for the real data to have peak magnitudes at lower frequencies where the sand is thinner. As the sand thickens to approximately 100 feet, the higher frequencies will better represent in map view where the sand is thicker. In other

words, with a high frequency map (around 45 Hertz) one should be able to map where the sand is dramatically thin.

Using spectral decomposition which iso-frequency is best for mapping the thin and thick sediments separately as a whole for the real data can be determined. The spectral response is illustrated in inline 140 displayed in Figure 5.2.10.

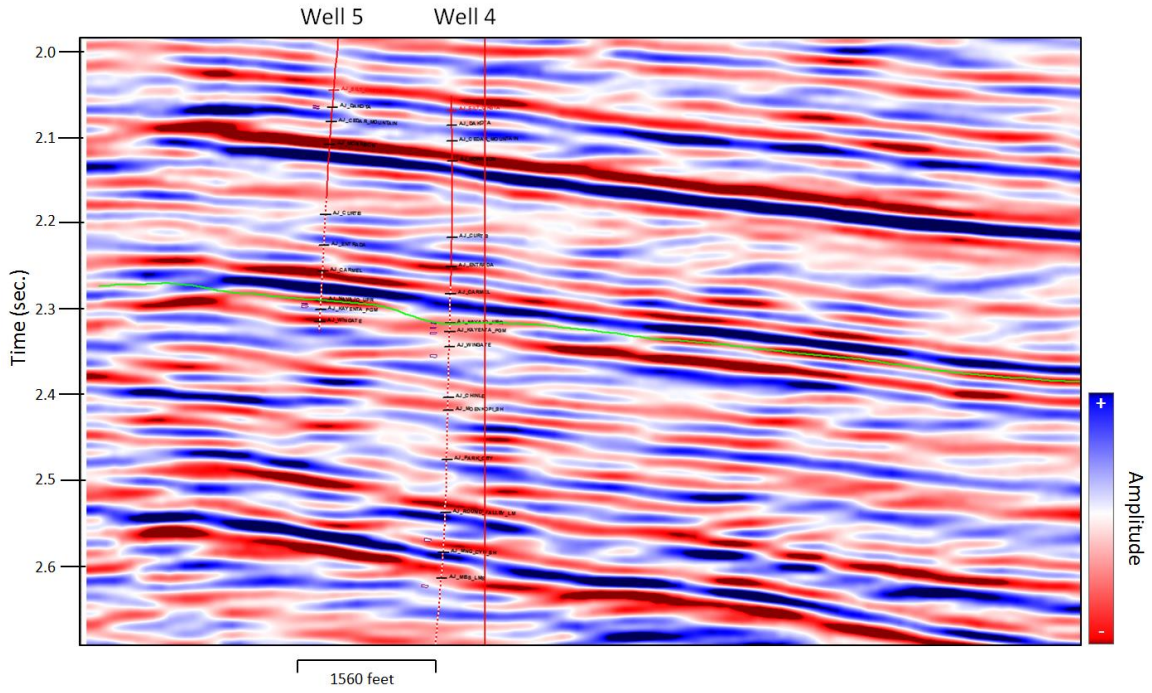

Figure 5.2.10 Inline 140 through Well 4 and Well 5. Well 4 represents where the sand is thin and Well 5 where it is thick. Notice the disappearance of the Kayenta peak in Well 4. All amplitudes are relative and thus unitless.

The CMP decomposition was run using a Ricker wavelet table from 2-120 Hertz and from 5-55 Hertz using a single Hertz increment with an Ormsby filter applied to the output from 5-10 and 45-55 (low pass- low cut and high cut-high pass) to filter the spectrum back to the original bandwidth. A single line analysis for the most part agrees with the synthetic model. In Figure 5.2.11a at roughly 18 Hertz the thin interval is still giving a peak magnitude signature. But, when the frequency is bumped up to 43 Hertz the peak magnitude has diminished to almost zero.

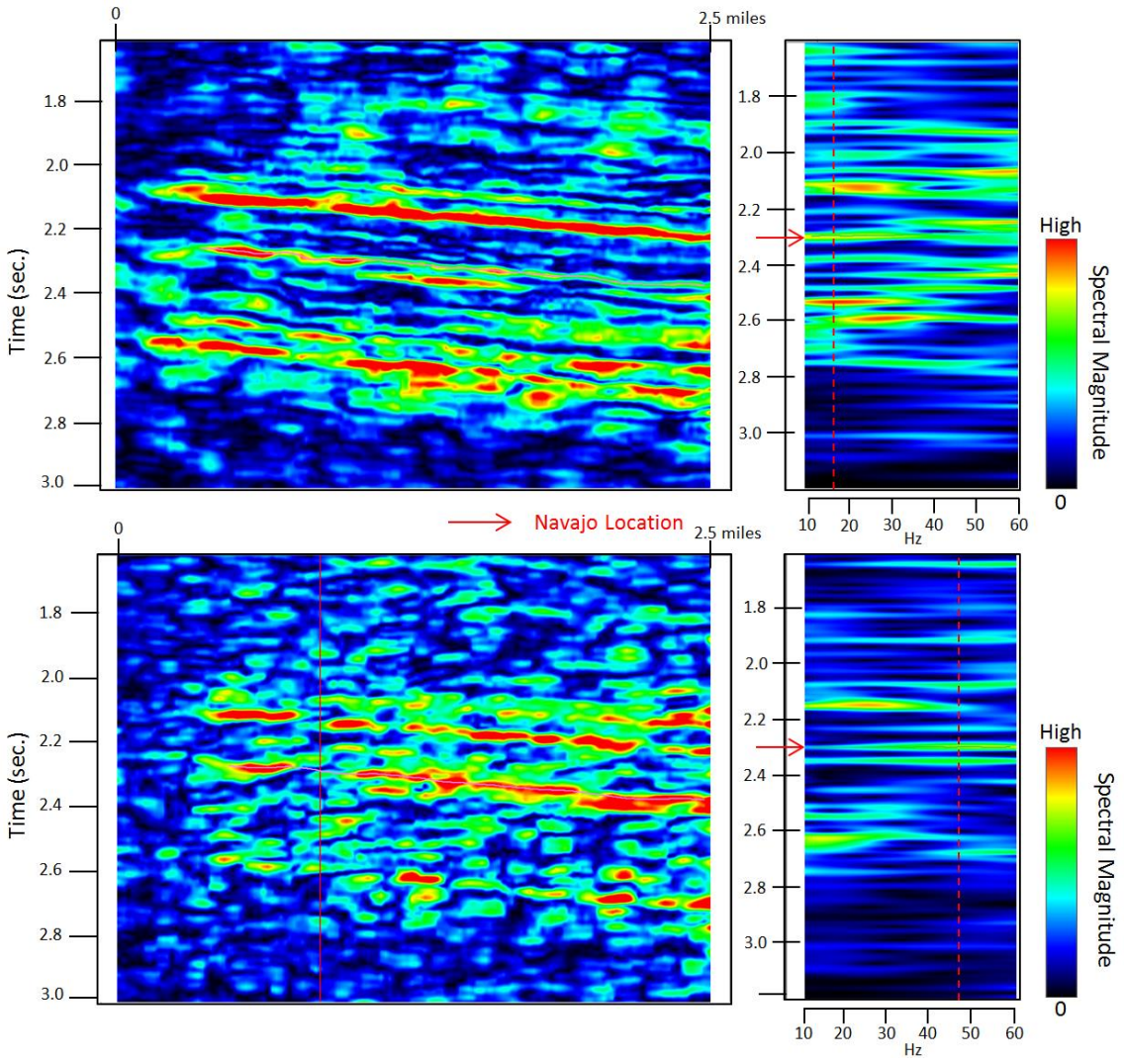

Figure 5.2.11 Iso-frequency response of Inline 140 at (a) 18 Hz and (b) 43 Hz. On the left is the iso-frequency response on the inline and to the right is the range of spectral magnitude at separate frequencies (10-60 Hz) at the well locations. At Well 4 location, the response is gone at 43 Hz but exist at 18 Hz.

Before running a full spectral decomposition, it was useful to output the peak magnitude and peak frequency components to highlight expected trends in the iso-frequencies. The CMP peak frequency component is displayed in Figure 5.2.12 where frequencies range from

10 to 55 Hertz. Where the Navajo is considerably thin (#4, #7, and #8) corresponds to lower peak frequencies between roughly 21-27 Hertz.

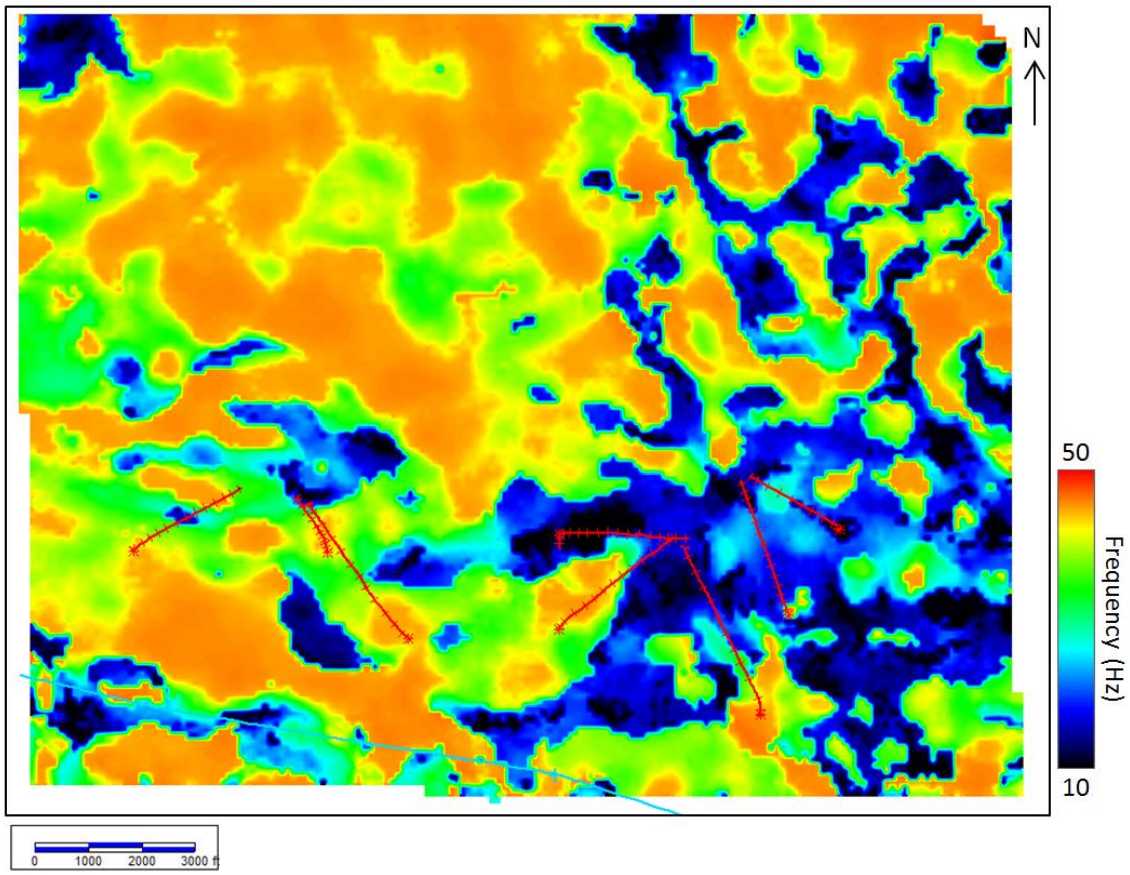

Figure 5.2.12 Peak frequency response on the Navajo horizon. From this map one anticipates the sand to thin in the east and thicken in the east.

Well locations with thicker sand accumulation (#1, #2, #3, #5, and #6) correspond to higher peak frequencies between 41 and 47 Hertz. This trend is relatively odd, considering one would expect thinner sands to correspond to higher peak frequencies. However, the Kayenta is still either unresolved or only slightly detected even with the bandwidth extended volume. One explanation is that the low peak frequencies result from the Wingate below where sediment is dense and thick. The thicker portions of the Navajo where the base (top of Kayenta) is well

resolved respond as one would expect. Displaying the peak magnitude component in Figure 5.2.13 reveals that a similar trend is occurring at the same well locations.

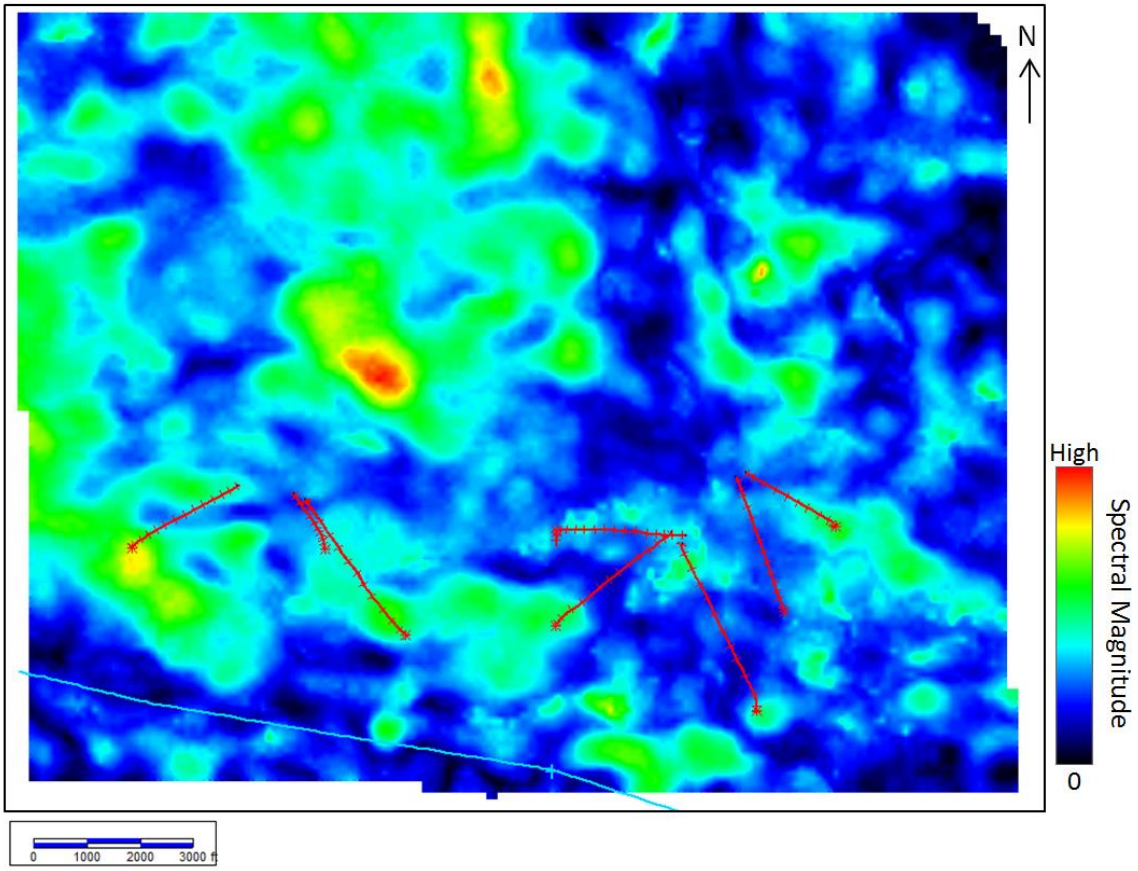

Figure 5.2.13 Peak magnitude response on the Navajo horizon.

The peak magnitude tends to be higher (warmer colors) where the sand is thicker and has a high peak frequency response. Wells that have relatively thin sand accumulation tend to have lower peak magnitudes (cooler colors) and lower peak frequencies. This could be due to the fact the base of the Navajo (Navajo-Kayenta transition) is unresolved and too thin to exhibit any frequency response. By using the low-frequency response from the Navajo-Wingate, one can map places where the sand is too thin using these responses. Figure 5.2.14 shows a map

extracted from (a) 23 Hertz and (b) 43 Hertz iso-frequencies. At 23 Hertz, the sand is interpreted as being roughly the same thickness across all 8 well locations.

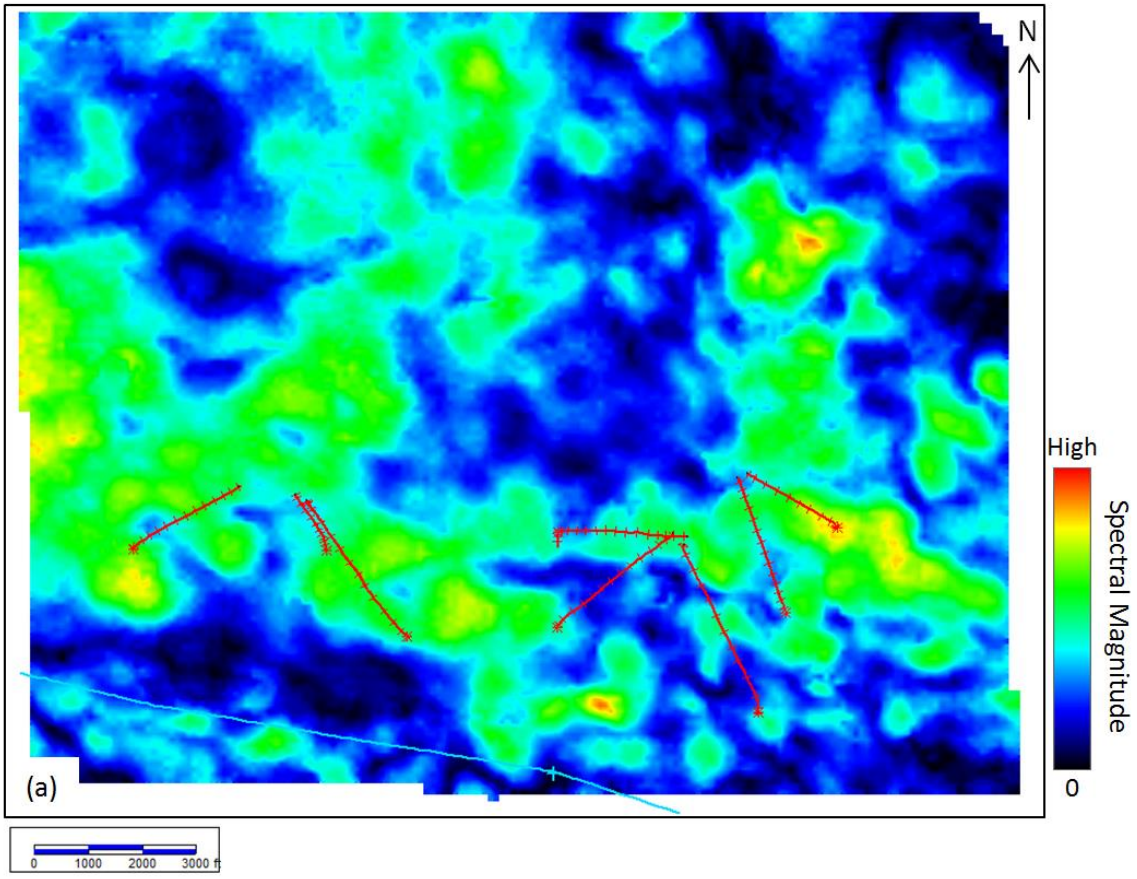

Figure 5.2.14 Iso-frequency responses on the Navajo horizon at (a) 23 Hz and (b) 43 Hz.

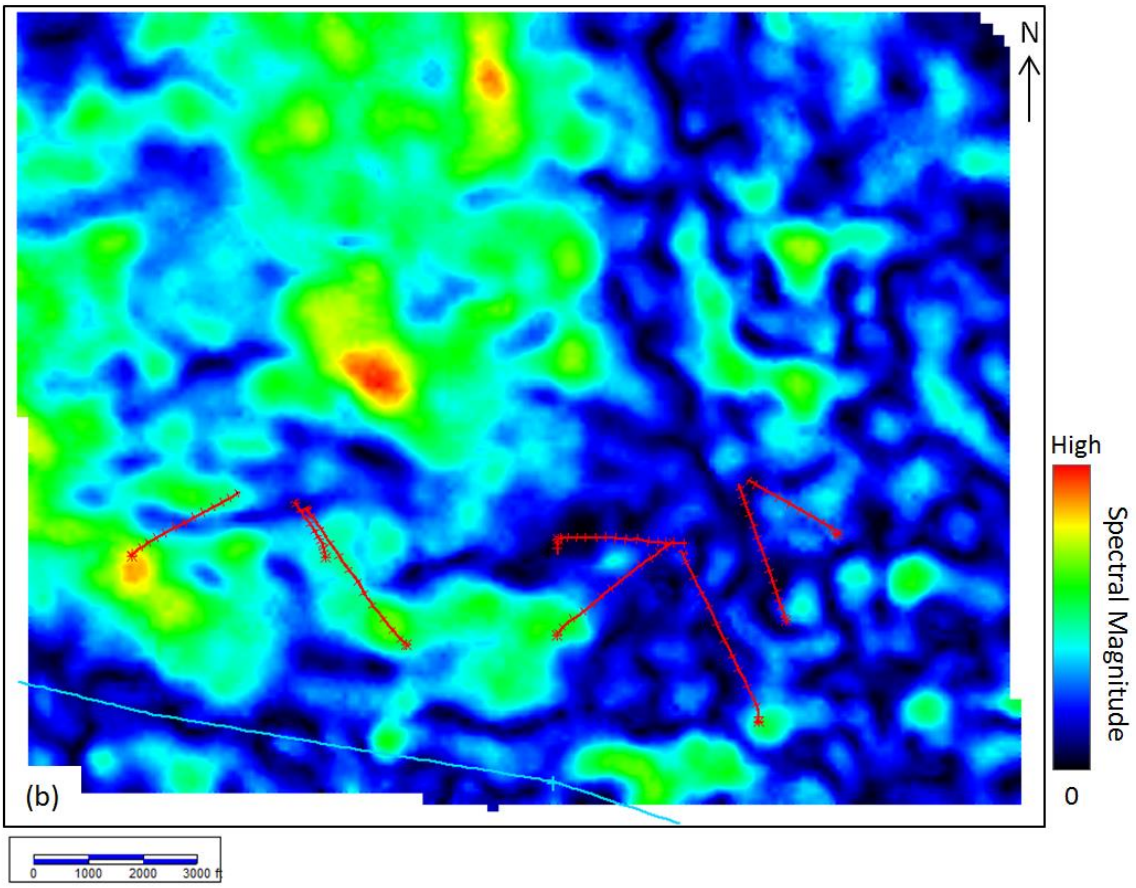

Figure 5.2.14 (continued) Iso-frequency responses on the Navajo horizon at (a) 23 Hz and (b) 43 Hz.

At 43 Hertz, only the locations where there is only thick sediment can be imaged. Correlating this map to known production in Figure 5.2.15, it can be seen that the well-production was highest where the sand is thick and degraded where the sediment is thin (Well 4, 7, 8). Well-logs show that the thicker sediment also has greater neutron-density crossover. This means the thick sediment is either richer in hydrocarbons or it is more porous. From the coherence display, it is known that the sand is continuous and does not truncate. This leads to the conclusion that well-performance is primarily dominated by the thickness of the sand and positioning on the Peter's Point structure (i.e. wells higher on the structure with thicker sand accumulation give the best well-performance). This is confirmed by Figure 5.2.15. The wells with

the best performance lie within the 43 Hertz peak magnitude signature. From here, the two best wells (Well 3 and 6) are positioned highest on the Prickly Pear structure.

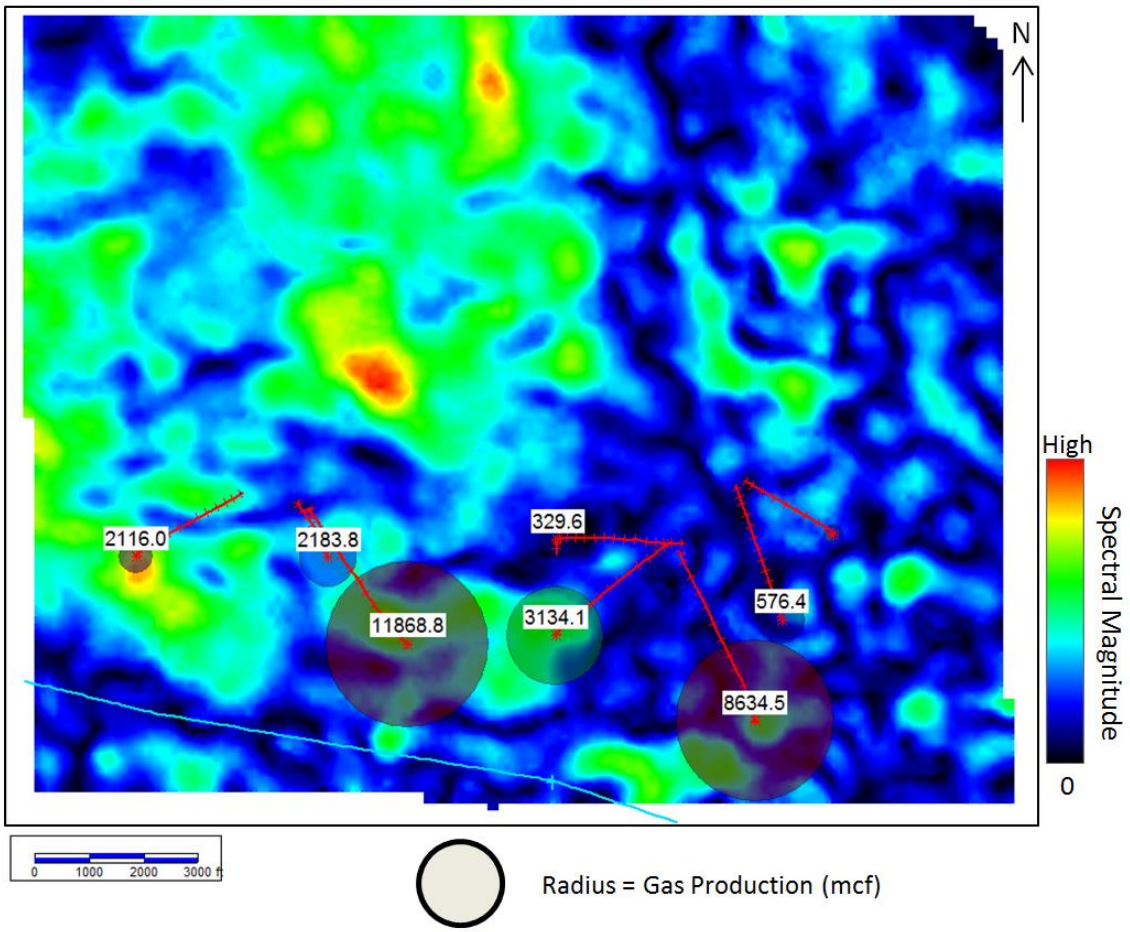

Figure 5.2.15 43 Hz iso-frequency response on the Navajo horizon with the correlating well-production. The best producing wells lie in high peak magnitude responses. The poor producers lie where the sand is thinnest (i.e., no peak magnitude response).

Also, it is important to note that Well 1 and Well 2 experienced mechanical failure issues which limited their production. It is possible that these wells only produced a fraction of their true capability. This is encouraging when discussing future prospects heading west where the sand is thicker.

5.3 Conclusions

Using a three-dimensional seismic survey, Stone Cabin 3D, and well-control with known production it was possible to successfully map portions of the Navajo sandstone where the sand is relatively thin. Running secondary seismic processing steps like 5D interpolation and wavelet packet denoising dramatically improved the overall signal-to-noise ratio of the target zone. With tertiary processing techniques like spectral whitening/shaping and bandwidth extension improvement in vertical resolution was achieved and the Navajo sandstone was resolved over a good portion of the test area. Bandwidth extended coherence (energy ratio similarity) was used to map the faulting in the Navajo interval. A synthetic model verified the spectral decomposition response over the entire data volume. With high frequencies the areas of the sand that were resolved (thick) and portions that were unresolved (thin) were mappable. The thin portions of the sand correlated to wells that were known poor producers and the thick portions to the wells that produced well (>2 BCFE). In particular, on the iso-frequency map of 43 Hertz it can be discerned where the sand is thick or thin which aids in the understanding of current gas production. Using these maps, future drilling locations can potentially be vetted in an area that has very little penetration or well control.

LIST OF REFERNCES

Abbott, Ward. "Tertiary of the Uinta basin." (1957): 102-109.

Anders, Donald E., James G. Palacas, and Ronald C. Johnson. "Thermal maturity of rocks and hydrocarbon deposits, Uinta Basin, Utah." (1992): 53-76.

Baker, Arthur Alan, John Warfield Huddle, and Douglas Merrill Kinney. "Paleozoic geology of north and west sides of Uinta Basin, Utah." *AAPG Bulletin* 33, no. 7 (1949): 1161-1197.

Bader, Jeffrey W. "Structural and tectonic evolution of the Douglas Creek arch, the Douglas Creek fault zone, and environs, northwestern Colorado and northeastern Utah Implications for petroleum accumulation in the Piceance and Uinta basins." *Rocky Mountain Geology* 44, no. 2 (2009): 121-145.

Biondi, Biondo. "Velocity estimation by beam stack." *Geophysics* 57, no. 8 (1992): 1034-1047.

Bump, Alexander P., and George H. Davis. "Late Cretaceous–early Tertiary Laramide deformation of the northern Colorado Plateau, Utah and Colorado."*Journal of Structural Geology* 25, no. 3 (2003): 421-440.

Chopra, Satinder, and Kurt J. Marfurt. "Seismic attributes for prospect identification and reservoir characterization." (2007).

Chopra, Satinder, and Kurt J. Marfurt. "Preconditioning seismic data with 5D interpolation for computing geometric attributes." *The Leading Edge* 32, no. 12 (2013): 1456-1460.

Fouch, Thomas D., Vito F. Nuccio, John C. Osmond, Logan MacMillan, William B. Cashion, and Craig J. Wandrey. "Oil and gas in uppermost Cretaceous and Tertiary rock, Uinta Basin, Utah." (1992): 9-48.

Gilluly, James, and John B. Reeside Jr. *Sedimentary rocks of the San Rafael Swell and some adjacent areas in eastern Utah*. No. 150-D. 1928.

Johnston, Robert E., and An Yin. "Kinematics of the Uinta fault system (southern Wyoming and northern Utah) during the Laramide orogeny."*International Geology Review* 43.1 (2001): 52-68.

Keighley, David, Stephen Flint, John Howell, and Andrea Moscariello. "Sequence stratigraphy in lacustrine basins: a model for part of the Green River Formation (Eocene), southwest Uinta Basin, Utah, USA." *Journal of Sedimentary Research* 73, no. 6 (2003): 987-1006.

Lawton, Don C. "Computation of refraction static corrections using first-break traveltime differences." *Geophysics* 54, no. 10 (1989): 1289-1296.

Liang, Chen. “Spectral Bandwidth Extention: Invention Versus Harmonic Extrapolation.”(Master’s Thesis, University of Houston, 2014).

Liner, Christopher L. *Elements of 3D seismology*. Vol. 1. PennWell Books, 2004.

Liu, Bin, and Mauricio D. Sacchi. "Minimum weighted norm interpolation of seismic records." *Geophysics* 69, no. 6 (2004): 1560-1568.

Liu, Jianlei, and Kurt J. Marfurt. "Matching pursuit decomposition using Morlet wavelets." *2005 SEG Annual Meeting*. Society of Exploration Geophysicists, 2005.

Malehmir, Alireza, and Christopher Juhlin. "An investigation of the effects of the choice of stacking velocities on residual statics for hardrock reflection seismic processing." *Journal of Applied Geophysics* 72.1 (2010): 28-38.

Marfurt, Kurt J. "Robust estimates of 3D reflector dip and azimuth."*Geophysics* 71, no. 4 (2006): P29-P40.

McPherson, Brian JOL, and John D. Bredehoeft. "Overpressures in the Uinta basin, Utah: Analysis using a three-dimensional basin evolution model."*Water Resources Research* 37, no. 4 (2001): 857-871.

Osmond, John C., Robert Locke, Alan C. Dilie, Walter Praetorious, and James G. Wilkins. "Natural gas in Uinta basin, Utah." (1968): 174-198.

Osmond, J. C. "History of Oil and Gas Exploration in the Uinta Basin, Utah."*MOUNTAIN GEOLOGIST* 40, no. 4 (2003): 101-110.

Pitman, Janet K., Karen J. Franczyk, and Donald E. Anders. "Marine and nonmarine gas-bearing rocks in Upper Cretaceous Blackhawk and Neslen Formations, eastern Uinta Basin, Utah: sedimentology, diagenesis, and source rock potential." *AAPG Bulletin* 71, no. 1 (1987): 76-94.

Rice, Dudley D., Thomas D. Fouch, and Ronald C. Johnson. "Influence of source rock type, thermal maturity, and migration on composition and distribution of natural gases, Uinta Basin, Utah." (1992): 95-110.

Sanborn, Albert F. "Possible future petroleum of Uinta and Piceance basins and vicinity, northeast Utah and northwest Colorado." *Exploration frontiers of the central and southern Rockies: RMAG Guidebook* (1977): 151-166.

Sanborn, A. F. "Potential petroleum resources of northeastern Utah and northeastern Colorado." *Field Conf. Guideb.(NM Geol. Soc.);(United States)*. Vol. 32. No. CONF-8110216-. 1981.

Schneider, William A., and Shih-Yen Kuo. "Refraction modeling for static corrections." In *1985 SEG Annual Meeting*. Society of Exploration Geophysicists, 1985.

Stone, Donald S. "Tectonic history of the Uncompahgre uplift." *Exploration frontiers of the central and southern Rockies: Rocky Mountain Association of Geologists* (1977): 23-30.

Taylor, K. G., and J. H. S. Macquaker. "Diagenetic alterations in a silt-and clay-rich mudstone succession: an example from the Upper Cretaceous Mancos Shale of Utah, USA." *Clay Minerals* 49.2 (2014): 213-227.

Taylor, A. W., and B. D. Ritts. "MESOSCALE HETEROGENEITY OF FLUVIALLACUSTRINE RESERVOIR ANALOGUES: EXAMPLES FROM THE EOCENE GREEN RIVER AND COLTON FORMATIONS, UINTA BASIN, UTAH, USA." *Journal of Petroleum Geology* 27, no. 1 (2004): 3-25.

Trad, Daniel. "Five-dimensional interpolation: Recovering from acquisition constraints." *Geophysics* 74, no. 6 (2009): V123-V132.

Walton, Paul T. "Geology of the Cretaceous of the Uinta Basin, Utah."*Geological Society of America Bulletin* 55, no. 1 (1944): 91-130.

Woog, Lionel J., Igor Popovic, and Anthony Vassiliou. "Applications of adapted waveform analysis for spectral feature extraction and denoising."*2005 SEG Annual Meeting*. Society of Exploration Geophysicists, 2005.

Yilmaz, O. "Seismic Data Processing: Society of Exploration Geophysiscists." (1987).

Zhang, Rui, and John Castagna. "Seismic sparse-layer reflectivity inversion using basis pursuit decomposition." *Geophysics* 76.6 (2011): R147-R158.

Zhou, Hua-Wei. *Practical seismic data analysis*. Cambridge University Press, 2014.

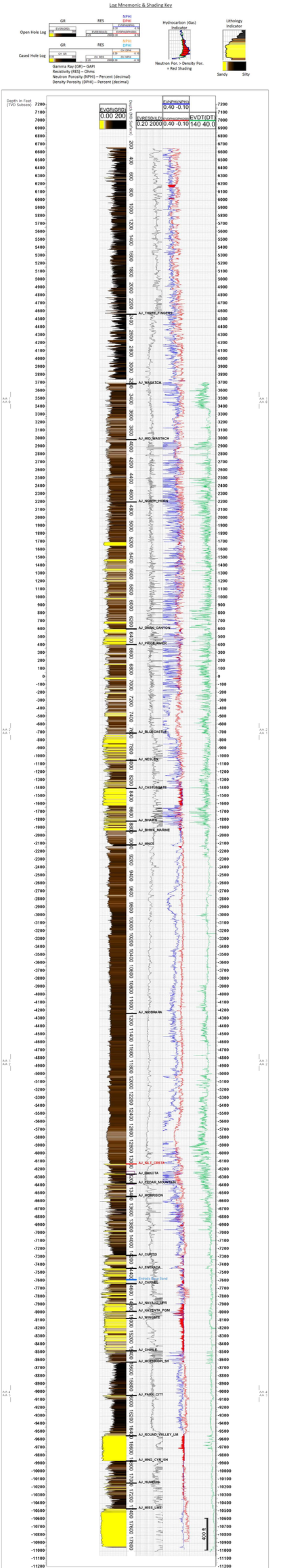

Type Log

Uinta Basin,

Utah

Figure 4.1.1a Type Log for well-log correlation in Wells 1-8. Picks were continued from this log to the remaing well control locations.

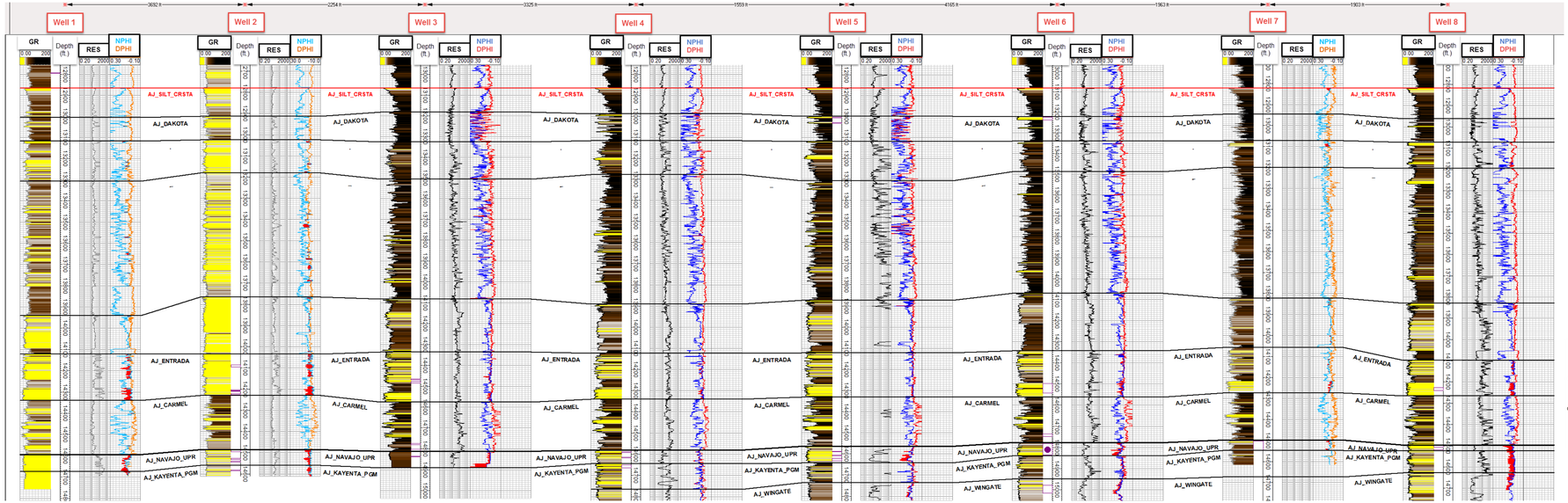

Log Mnemonic & Shading Key

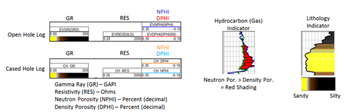

Gamma Ray (GR) – GAPI
Resistivity (RES) – Ohms
Neutron Porosity (NPHI) – Percent (decimal)
Density Porosity (DPHI) – Percent (decimal)

Neutron Por. > Density Por. = Red Shading

Figure 4.1.2 Well-to-well cross-section from well 1 to Well 8 with the Dakota Silt flooding surface marked by the red line. This pick was used as a calibration point for successive picks.

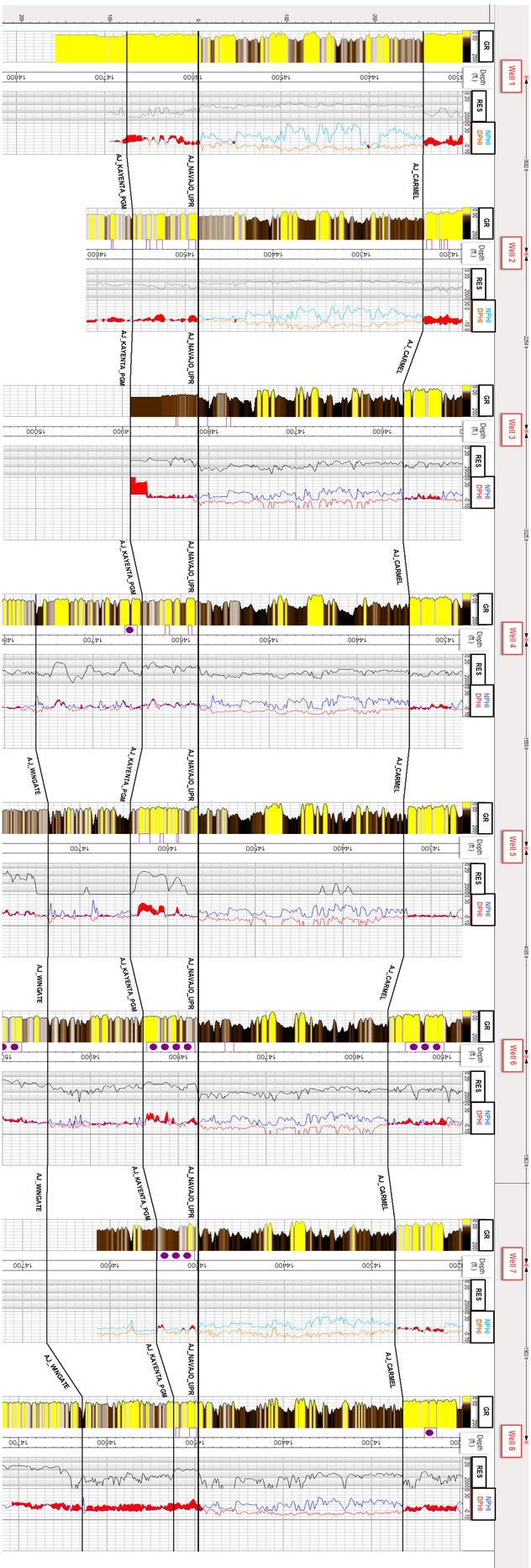

Figure 4.1.3 Well-to-well cross section zoomed in and flattened on the Navajo sandstone pick. Notice the Navajo varies in thickness in well to well from approximately 30 feet to 90 feet.